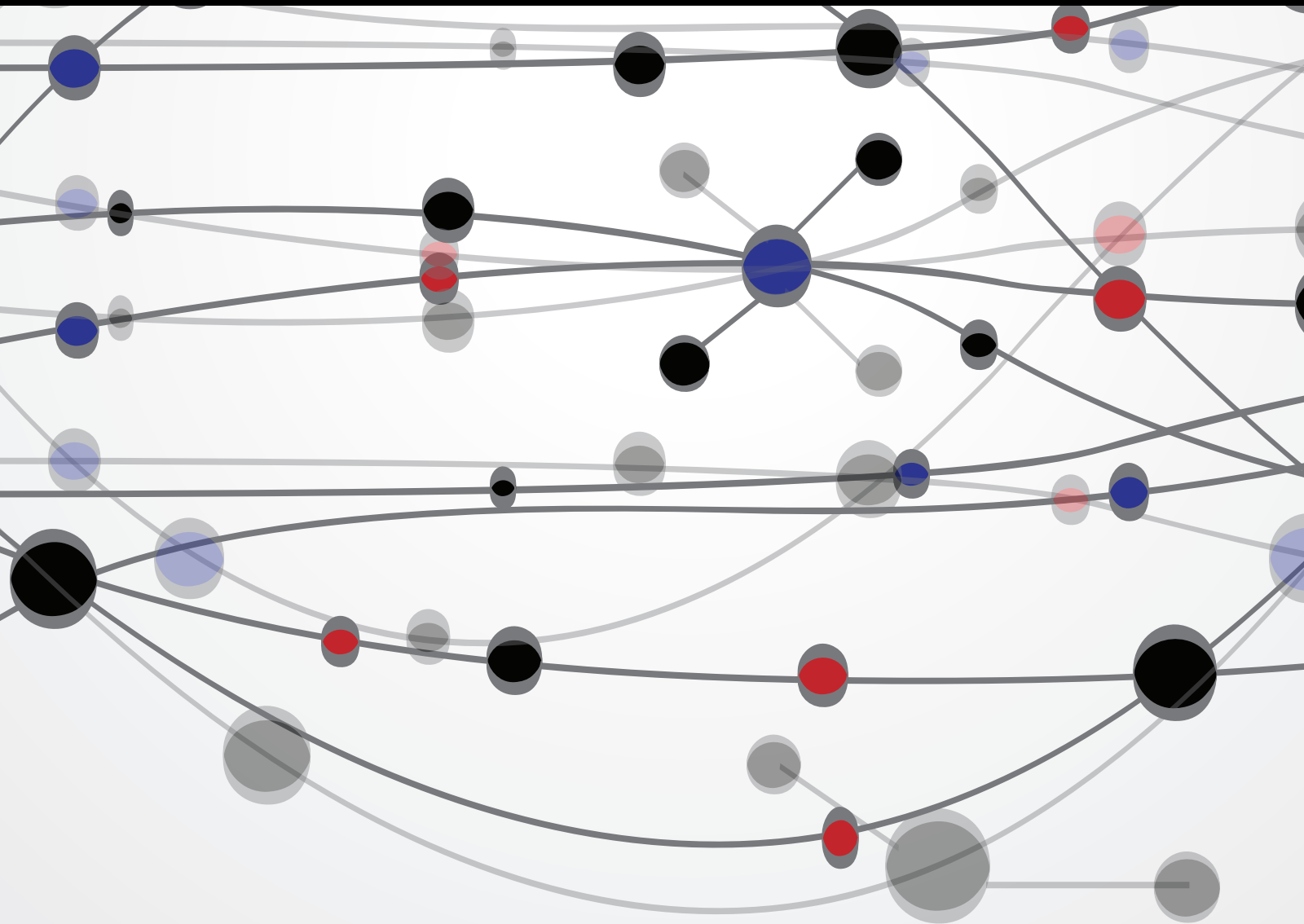


Soft Computing Methods in Civil Engineering

Guest Editors: Siamak Talatahari, Vijay P. Singh, Amir H. Alavi,
and Fei Kang





Soft Computing Methods in Civil Engineering

The Scientific World Journal

Soft Computing Methods in Civil Engineering

Guest Editors: Siamak Talatahari, Vijay P. Singh,
Amir H. Alavi, and Fei Kang



Copyright © 2015 Hindawi Publishing Corporation. All rights reserved.

This is a special issue published in “The Scientific World Journal.” All articles are open access articles distributed under the Creative Commons Attribution License, which permits unrestricted use, distribution, and reproduction in any medium, provided the original work is properly cited.

Contents

Soft Computing Methods in Civil Engineering, Siamak Talatahari, Vijay P. Singh, Amir H. Alavi, and Fei Kang

Volume 2015, Article ID 605871, 2 pages

Optimal Pipe Size Design for Looped Irrigation Water Supply System Using Harmony Search: Saemangeum Project Area, Do Guen Yoo, Ho Min Lee, Ali Sadollah, and Joong Hoon Kim

Volume 2015, Article ID 651763, 10 pages

Conceptual Comparison of Population Based Metaheuristics for Engineering Problems,

Oluwole Adekanmbi and Paul Green

Volume 2015, Article ID 936106, 9 pages

Safety Identifying of Integral Abutment Bridges under Seismic and Thermal Loads,

Narges Easazadeh Far and Majid Barghian

Volume 2014, Article ID 757608, 12 pages

Performance-Based Seismic Design of Steel Frames Utilizing Colliding Bodies Algorithm, H. Veladi

Volume 2014, Article ID 240952, 6 pages

A Parametric Study of Nonlinear Seismic Response Analysis of Transmission Line Structures, Li Tian,

Yanming Wang, Zhenhua Yi, and Hui Qian

Volume 2014, Article ID 271586, 9 pages

The Effect Analysis of Strain Rate on Power Transmission Tower-Line System under Seismic Excitation,

Li Tian, Wenming Wang, and Hui Qian

Volume 2014, Article ID 314605, 10 pages

Editorial

Soft Computing Methods in Civil Engineering

Siamak Talatahari,¹ Vijay P. Singh,² Amir H. Alavi,³ and Fei Kang⁴

¹*Department of Civil Engineering, University of Tabriz, Tabriz, Iran*

²*Department of Biological and Agricultural Engineering, Texas A&M University, College Station, USA*

³*Department of Civil and Environmental Engineering, Michigan State University, Engineering Building, East Lansing, MI 48824, USA*

⁴*Dalian University of Technology, Dalian, China*

Correspondence should be addressed to Siamak Talatahari; siamak.talat@gmail.com

Received 26 February 2015; Accepted 26 February 2015

Copyright © 2015 Siamak Talatahari et al. This is an open access article distributed under the Creative Commons Attribution License, which permits unrestricted use, distribution, and reproduction in any medium, provided the original work is properly cited.

Demand for lightweight, efficient, and low cost structures seems mandatory because of growing realization of the rarity of raw materials and rapid depletion of convention energy sources. This requires engineers to be aware of optimization techniques. Designing, analyzing, and solving civil engineering problems can be very large scale and can be highly nonlinear, and to find solutions to these problems is often very challenging. In the past two decades, soft computing methods are becoming an important class of efficient tools for developing intelligent systems and providing solutions to complicated engineering problems.

The papers selected for this special issue represent a good panel in recent challenges. The topics of these papers are connected with the computational intelligence methods and their application in civil and hydraulic engineering. An investigation on different metaheuristics abilities for engineering problems was studied by O. Adekanmbi and P. Green. They utilized the third version of generalized differential evolution (GDE) for solving practical engineering problems. GDE3 metaheuristic modifies the selection process of the basic differential evolution and extends DE/rand/1/bin strategy.

Performance-based seismic design of steel frames using the colliding bodies optimization (CBO) algorithm as new optimization method was presented by H. Veladi. A pushover analysis method based on semirigid connection concept was developed and the CBO algorithm is employed to find optimum seismic design of frame structures. H. Veladi solved two numerical examples from literature and show the power or weakness of this new algorithm.

A parametric study of nonlinear seismic response analysis of transmission line structures and the effect analysis of strain rate on power transmission tower-line system under seismic excitation were developed by L. Tian et al. in two papers. In one of them, nonuniform ground motions are generated using a stochastic approach based on random vibration analysis. Then, the effects of multicomponent ground motions, correlations among multicomponent ground motions, wave travel, coherency loss, and local site on the responses of the cables were investigated using nonlinear time history analysis method. The results showed the multicomponent seismic excitations should be considered, but the correlations among multicomponent ground motions could be neglected. While, in the other, a three-dimensional finite element model of a transmission tower-line system was created based on a real project. The results showed that the effect of strain rate on the transmission tower generally decreases the maximum top displacements, but it would increase the maximum base shear forces, and thus it is necessary to consider the effect of strain rate on the seismic analysis of the transmission tower. The effect of strain rate could be ignored for the seismic analysis of the conductors and ground lines, but the responses of the ground lines considering strain rate effect are larger than those of the conductors.

A study of bridge structures is performed by N. Easazadeh Far and M. Barghian. They selected integral abutment bridges (IABs) as jointless bridges. Although all developed bridge design codes consider temperature and earthquake loads separately in their specified load combinations for conventional

bridges with expansion joints, the thermal load is an “always on” load and during the occurrence of an earthquake, these two important loads act on bridge simultaneously. Safety identifying of these bridges under seismic and thermal loads is the main aim of their work where the safety of IABs, designed by AASHTO LRFD bridge design code, under combination of thermal and seismic loads was studied. They showed that for an IAB designed by AASHTO LRFD the reliability indexes have been reduced under combined effects.

In the field of hydraulic engineering, optimal design of pipe sizes for looped irrigation water supply system is presented by D. G. Yoo et al. in which they developed a harmony search algorithm to fulfill this aim. Their study mainly serves two purposes. The first is to develop an algorithm and a program for estimating a cost-effective pipe diameter for agricultural irrigation water supply systems using optimization techniques. The second is to validate the developed program by applying the proposed optimized cost-effective pipe diameter to an actual study region (Saemangeum project area, zone 6). They show that the optimal design program can be effectively applied for the real systems of a looped agricultural irrigation water supply.

Acknowledgments

We would like to thank the authors for their excellent contributions and the reviewers for helping improve the papers.

*Siamak Talatahari
Vijay P. Singh
Amir H. Alavi
Fei Kang*

Research Article

Optimal Pipe Size Design for Looped Irrigation Water Supply System Using Harmony Search: Saemangeum Project Area

Do Guen Yoo, Ho Min Lee, Ali Sadollah, and Joong Hoon Kim

School of Civil, Environmental and Architectural Engineering, Korea University, Seoul 136-713, Republic of Korea

Correspondence should be addressed to Joong Hoon Kim; jaykim@korea.ac.kr

Received 27 August 2014; Accepted 23 October 2014

Academic Editor: Siamak Talatahari

Copyright © 2015 Do Guen Yoo et al. This is an open access article distributed under the Creative Commons Attribution License, which permits unrestricted use, distribution, and reproduction in any medium, provided the original work is properly cited.

Water supply systems are mainly classified into branched and looped network systems. The main difference between these two systems is that, in a branched network system, the flow within each pipe is a known value, whereas in a looped network system, the flow in each pipe is considered an unknown value. Therefore, an analysis of a looped network system is a more complex task. This study aims to develop a technique for estimating the optimal pipe diameter for a looped agricultural irrigation water supply system using a harmony search algorithm, which is an optimization technique. This study mainly serves two purposes. The first is to develop an algorithm and a program for estimating a cost-effective pipe diameter for agricultural irrigation water supply systems using optimization techniques. The second is to validate the developed program by applying the proposed optimized cost-effective pipe diameter to an actual study region (Saemangeum project area, zone 6). The results suggest that the optimal design program, which applies an optimization theory and enhances user convenience, can be effectively applied for the real systems of a looped agricultural irrigation water supply.

1. Introduction

Water supply systems are mainly classified into branched and looped network systems. The main difference between the two is that, in a branched network system, the flow within each pipe is a known value, whereas in a looped network system, the flow within each pipe is considered an unknown value. Therefore, an analysis of a looped network system can be a more complex endeavor.

Water supply systems form part of a larger social infrastructure of an industrial society; their objective is the effective supply of water from a water source to an area in demand. The analysis of a water supply system can be one of the more complex mathematical problems. A significant fraction of the entire set of equations consists of nonlinear equations, and a large number of these equations must be solved simultaneously.

This process requires sufficient consideration of the law of conservation of energy and a continuity equation of mass. In this regard, over the past few decades, many methods have been developed to analyze water supply systems and perform

hydraulic simulations of their steady state conditions. Commercial hydraulic analysis programs such as EPANET [1] and WaterGEMS [2] have been developed to analyze the hydraulic simulations of large water supply systems, an achievement that could not even be dreamed of in past years.

The development of such models has played an important role in the design and operation of water supply systems. However, problems related to the selection of the pipe diameter for configuring low-cost water supply systems have emerged as important issues that need to be resolved.

In recent years, many optimization methods have been used for the design of low-cost water supply systems. The process for obtaining an optimal water supply system and pipe diameter is considered important because it helps in determining the final operational costs. However, because the aforementioned problems are extremely complex, they are constrained by the types of methods selected for defining the problems, as well as by analysis methods; thus far, only a minimization of the construction costs has been experimentally applied [3–6].

If the structure of a water supply system and its constraints (water pressure and velocity) are known, the optimal design of the water supply system can be expressed in terms of the selection of a pipe diameter that minimizes the total cost. The mathematical optimization methods described earlier can easily be used to find the optimal solutions in small systems within an ideal environment.

However, if existing mathematical optimization methods are applied to actual civil engineering problems, the limitations of these methods are revealed. For example, in linear programming, because all functions applied to such problems are linear, simplified assumptions lower the accuracy of the final solution. On the other hand, in dynamic programming, too many combinations have to be considered to obtain the optimal solutions, thereby requiring a considerable amount of computational effort and storage space.

In nonlinear programming, if the initial solution is not located at a good position within the solution zone, the global optimum is unobtainable, and the initial solution cannot escape from the local optima. To overcome these disadvantages, during the last 20 years, researchers have attempted to apply new approaches to optimization technologies that do not use an existing mathematical methodology.

Rather than relying completely on conventional differential derivatives, the technologies currently being developed apply a natural evolution phenomenon, that is, the principle of the survival of the fittest, and artificial imitations of this phenomena in the optimal system design; these have yielded better results than those obtained using an existing optimal mathematical design.

Such nature-inspired optimization algorithms are called metaheuristic algorithms. Some examples of such algorithms include a Genetic Algorithm (GA), Simulated Annealing (SA), Tabu Search (TS), Ant Colony Optimization (ACO), Harmony Search (HS), and Particle Swarm Optimization (PSO). Reça et al. [7], Monem and Namdarian [8], da Conceição Cunha and Ribeiro [9], Zecchin et al. [10], Geem et al. [11], and Montalvo et al. [12] have conducted studies on the optimal design of water supply systems using the GA, SA, TS, ACO, HS, and PSO algorithms, respectively. In recent years, hybrid versions of existing algorithms and new algorithms have been also developed such as Genetic Heritage Evolution by Stochastic Transmission (GHEST, [13]), NLP-Differential Evolution algorithm (Combined NLP-DE, [14]), Hybrid Particle Swarm Optimization and Differential Evolution (Hybrid PSO-DE, [15]), and Charged System Search algorithm (CSS, [16]).

However, most of these studies have disadvantages in that they were applied to small benchmark problems and were not reflected in the actual plans [17]. The present study aims to develop an optimal pipe diameter estimation technique of an actual agricultural looped irrigation water supply system using an HS algorithm. This study has two main purposes. The first is to develop an economic pipe diameter estimation algorithm and program using the optimization techniques for agricultural irrigation water supply systems. The second is to validate the developed program by applying the proposed optimized economic pipe diameter to an actual target region (Saemangeum business area, zone 6).

TABLE 1: Land use divisions according to the comprehensive Saemangeum development plan.

Division and facilities	Ratio (%)	Area (km ²)
Agricultural lands	30.3	85.7
U-complex urban lands	23.8	67.3
Industrial lands (free economic zone (FEZ))	6.6	18.7
Science and research lands	8.1	22.9
New and renewable energy lands	7.2	20.4
Urban lands	5.2	14.7
Sinsi-Yami multifunctional lands	0.7	2.0
Ecological and environmental lands	15.0	42.4
Water proof facilities and so forth	3.1	8.8
Total	100.0	282.9

2. Saemangeum Project

The Saemangeum Project is a reclamation project intended to create land from a mud flat and sea waters along the western coast of South Korea by constructing a 33.9 km long seawall. Under the Saemangeum Project, which was started on November 16, 1991, the construction of a cofferdam was completed on April 21, 2006, and the reinforcement and embankment projects were completed on April 27, 2010.

The Saemangeum seawall is listed in the Guinness Book of World Records as the longest seawall on record and is 1.4 km longer than the Zuider seawall (32.5 km) of the Netherlands, which was earlier regarded to be the longest. The construction of the seawall has resulted in the reclamation of a new region with an area of 401 km², of which land and a fresh water lake account for 283 km² and 118 km², respectively.

Upon completion of the seawall construction, the South Korean Government newly formulated its Comprehensive Saemangeum Development Plan. According to this plan, the reclaimed land is to be developed as the central agricultural and economic sector of Northeast Asia, with the reclaimed land mainly divided into nine areas, as shown in Figure 1 and Table 1.

Agricultural lands account for the largest share (30.3%) among the divided areas. These agricultural lands are used for ensuring national competitiveness, producing high-value-added agricultural products, and developing food-industry facilities through mixed environment-friendly agriculture and ecological crop cultivation. Traditionally, agricultural irrigation water supply systems have been designed as branched water supply networks, which incur less initial costs. However, such networks are disadvantageous in that they do not ensure the reliability of the water supply.

In recent years, new cultivation methods such as greenhouse crop cultivation, high-value-added crop cultivation, and perennial cultivation have been adopted. Accordingly, agricultural irrigation water supply systems also need to provide a stable and reliable water supply, as achieved by urban water supply systems.

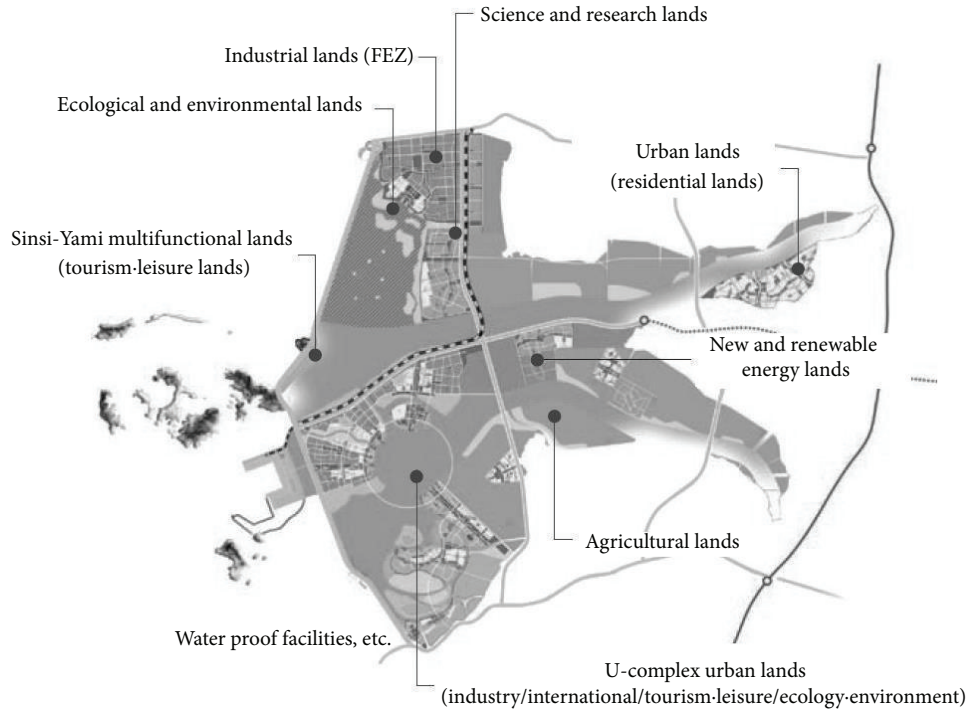


FIGURE 1: Comprehensive Saemangeum development plan.

3. Model Development and Methodology

3.1. Harmony Search Algorithm. The HS algorithm proposed by Geem et al. [11] is an optimization technique used in pipe design. HS is a solution-finding technique that considers an optimal solution in engineering to correspond to an optimal sound in music. Generally, heuristic search methods involve the observation of natural phenomena, but the HS method is an algorithm based on the artificial phenomenon of harmony.

When sounds are produced by various sources, they together create a single harmony. Some of these created harmonies sound pleasant, whereas others sound dissonant. Eventually, the discordant harmonies disappear through practice, and among the more appropriate harmonies (local optimum), those that are aesthetically the most beautiful (global optimum) are achieved.

In other words, the HS algorithm considers an optimal solution to be an optimal harmony found through practice. The principle of the HS algorithm can be explained in detail by first comparing how music improvisation and optimization calculations correspond to each other.

Improvisation is the spontaneous creation of notes by performers without relying on sheet music (score). The ability of the performers improves the more they perform together, and ultimately a top-level harmony is created. In such an improvisation, each performer (e.g., a saxophonist, guitarist, and double bass player, as shown in Figure 2) can be referred to as a decision variable or design variable (χ_1 , χ_2 , and χ_3 in Figure 2).

The musical range of each instrument (in the case of the saxophonist, e.g., one of the notes among Do, Re, and Mi,

can be created) made by the corresponding performer can be referred to as the range of each variable (in the case of χ_1 in Figure 2, its pipe diameter may be 100, 200, or 300 mm). Moreover, when each performer plays a different note, the harmony they create (e.g., the harmony in the figure) (i.e., saxophone, Do; double bass, Mi; and guitar, Sol) corresponds to the overall solution vector obtained (the solution vector for Figure 2 is $\chi_1 = 100$ mm, $\chi_2 = 300$ mm, and $\chi_3 = 500$ mm) by substituting the value of each variable.

Whether the harmony played at a point in time is of high quality is judged aesthetically by the performers or audience through auditory stimuli. If the harmony is very pleasant for the performers or audience, it will often be replayed in the memories. Likewise, during an optimization, whether a solution vector is good or bad can be determined by substituting the vector in an objective function; if this yields a better functional value than the existing one, the solution vector will be preserved.

Moreover, in an improvisation, as the performance is repeated, better harmonies are created, and ultimately, a high level of ability is reached; likewise, in an optimization operation, as additional iterations are carried out, better functional values are increasingly developed, and ultimately, the optimum value is obtained.

The harmony memory (HM), harmony memory considering rate (HMCR), and pitch adjustment rate (PAR) are important factors in the HS method for finding an optimal solution. First, each musical performer should have a memory space to preserve a good harmony; before starting the important process of the HS algorithm, a harmony

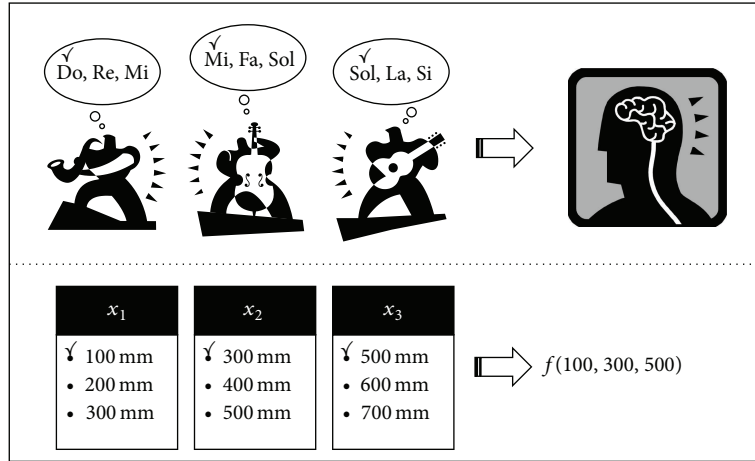


FIGURE 2: Concepts of a harmony search.

```

Begin
Objective function  $f(x)$ ,  $x = (x_1, x_2, \dots, x_d)^T$ 
Generate initial harmonics (Define Harmony Memory and Size, HM & HMS)
Define pitch adjusting rate (PAR), pitch limits and bandwidth (BW)
Define harmony memory considering rate (HMCR)
while ( $t < \text{Max number of iterations}$ )
Generate new harmonics by accepting best harmonics
Adjust pitch to get new harmonics (solutions)
if ( $\text{rand} > \text{HMCR}$ ), choose an existing harmonic randomly
else if ( $\text{rand} > \text{PAR}$ ), adjust the pitch randomly within limits
else generate new harmonics via randomization
end if
Accept the new harmonics (solutions) if better
end while
Find the current best solutions
End
    
```

PSEUDOCODE 1: Pseudocode of HS.

memory space is created by consolidating existing memory spaces.

This is called the HM, and the maximum number of harmonies that can be stored in this storage space is called the harmony memory size (HMS). Next, to produce better solutions from the harmony storage space, which is initially filled by as many random vectors as the HMS, the HS algorithm employs three types of operators.

3.1.1. Random Selection. In the random selection technique, the value of a variable is randomly selected from all values of the playable note range. If K is the total number of all possible variable values, one of them is randomly selected, and the probability of this technique being adopted is $1 - \text{HMCR}$.

3.1.2. Memory Consideration. The memory consideration technique picks the value of a variable from the existing high-quality notes. In other words, a single value is picked from all values possessed by a variable within the storage space.

Its probability is HMCR, and although it can have a value between 0 and 1, a value between 0.7 and 0.95 is usually used; nevertheless, the value is changeable.

3.1.3. Pitch Adjustment. For a pitch adjustment, a note obtained through a memory recall technique is considered a basic note, and its pitch is trimmed by adjusting the note based on the surrounding upper and lower notes. In an actual calculation, when a single value is obtained using a memory recall technique, it is adjusted by a one-step higher or lower value. The PAR is the probability of this technique actually being applied, and it can attain a value between 0 and 1. Generally, the PAR has a value of around 0.01 to 0.3, but this can vary. Pseudocode 1 shows the pseudocode of the HS algorithm.

3.2. Objective Function. An objective function minimizes the design cost of an irrigation system. The algorithm developed in the present study was applied to an optimization;

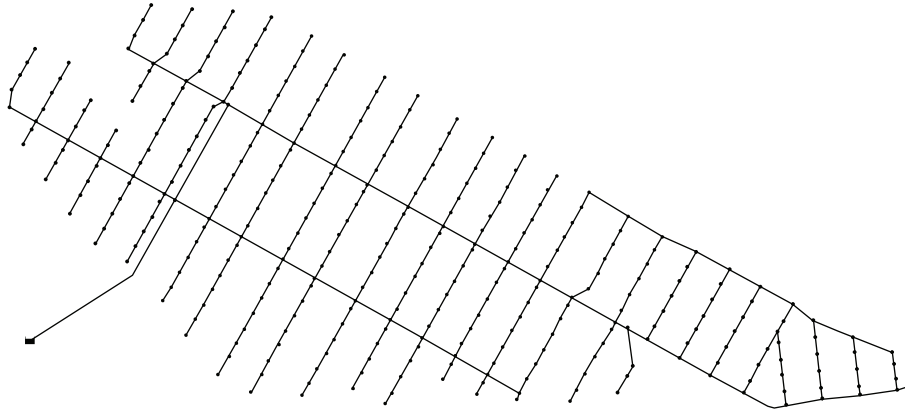


FIGURE 3: A looped water supply network applied to the target zone of Saemangeum.

the construction costs, pipe material costs, and maintenance costs are considered as the design costs according to the pipe diameter. Therefore, the equation for the objective function is as follows:

$$\text{Min} \cdot \text{Cost} = \sum_{i=1}^N (C_C(D_i) + C_M(D_i) + C_P(D_i)) L_i, \quad (1)$$

where $C_C(D_i)$ is cost function (construction cost) per unit length (m) for each pipe diameter, $C_M(D_i)$ is cost function (maintenance cost) per unit length (m) for each pipe diameter, $C_P(D_i)$ is cost function (pipe material cost) per unit length (m) for each pipe diameter, L_i is length of the pipe (m), D_i is pipe diameter (mm), and N is total number of pipes.

Hydraulic constraint equations are considered in optimization problems. Therefore, a penalty function method is introduced to convert the optimization problem subject to constraint conditions into an optimization that is free from the constraint conditions. The final objective function, which is applied using a penalty function, can be defined as follows:

$$\begin{aligned} \text{Min} \cdot \text{Cost} = & \sum_{i=1}^N (C_C(D_i) + C_M(D_i) + C_P(D_i)) L_i \\ & + \sum_{j=1}^M P_j |h_j - h_{\min \text{ or } \max}| \\ & + \sum_{i=1}^N P_i |v_i - v_{\min \text{ or } \max}|, \end{aligned} \quad (2)$$

where h_j is pressure head of each node (m), h_{\min} is minimum pressure head (m), h_{\max} is maximum pressure head (m), v_i is velocity of each pipe (m/s), v_{\min} is minimum pipe velocity (m/s), v_{\max} is maximum pipe velocity (m/s), P_j , P_i are penalty functions with regard to the pressure and pipe velocity, and M is total number of nodes.

The above penalty function is applied only when the pressure of each node and the velocity of the pipe exceed either the minimum or maximum value; the equation below represents the penalty function equation applied to the

present model. In the target water supply system, the minimum and maximum nodal pressures were set to 10 and 35 m, respectively, and the minimum and maximum pipe velocities were set to 0.01 and 2.5 m/s, respectively:

$$\begin{aligned} P_j &= \alpha (|h_j - h_{\min \text{ or } \max}|) + \beta, \\ P_i &= \alpha (|v_i - v_{\min \text{ or } \max}|) + \beta, \end{aligned} \quad (3)$$

where α , β are penalty constants.

When running an optimization model, if the pressure head of each node and the velocity of the pipe do not satisfy the minimum and maximum values, which are the design conditions, the penalty cost is increased by assigning a significantly greater value to α so that the solution will not be selected. To prepare for a case in which the pressure head and pipe velocity fall short of the design conditions by a small margin, a model that largely satisfies all of the design conditions was implemented by assigning a large value to β . A trial-and-error analysis was conducted using the α and β values for Saemangeum, which is the target area of the present project. The results indicate that an effective optimal design is possible when α and β are assigned values of 10,000,000 and 100,000,000, respectively. But, detailed studies about constraint handling techniques and determination of their parameters should be tackled to improve model efficiency and reliability in future.

4. Saemangeum Water Supply Network Application and Results

4.1. Target Water Supply Network. In the present study, proposal data on the loop-type design of the six zones of Saemangeum were obtained and applied to one of the zones. A diagram of the corresponding water supply network is shown in Figure 3. The target water supply network comprises 356 pipelines, and as mentioned earlier, some of the network consists of a circuit-type water supply.

The data on the cost incurred per unit of pipe length for the different diameter pipes used in this study are listed in Table 2. For optimization, 18 types of commercial pipes with

TABLE 2: Cost data corresponding to different pipe diameters for Saemangeum.

Pipe diameter (mm)	Cost (₩/m)		
	Construction costs	Material costs	Maintenance costs
80	65,000	15,000	6,500
100	65,999	27,583	6,600
150	76,410	40,686	7,641
200	86,028	58,716	8,603
250	96,135	81,160	9,614
300	105,325	103,231	10,533
350	113,818	125,107	11,382
400	126,797	148,836	12,680
450	136,250	155,522	13,625
500	147,792	181,823	14,779
600	171,991	211,396	17,199
700	211,413	273,528	21,141
800	307,640	339,740	30,764
900	359,048	384,619	35,905
1,000	415,702	451,932	41,570
1,100	482,074	547,224	48,207
1,200	576,736	606,962	57,674
1,350	687,390	716,075	68,739

TABLE 3: Decision variables and number of possible solutions for the target water supply network.

Target water supply network	Number of water supply network decision variables in the initial design	Total length of the pipeline	Number of possible solutions
Six zones of Saemangeum (loop type)	356	40,440 m	$18^{356} \approx \infty$

different diameters were considered. Data on the construction and pipe material costs corresponding to the different pipe diameters were obtained from the “Water Facilities Construction Cost Estimation Report” from K-water [18], which provides estimated data on the construction costs for different steel pipe diameters. The task of optimization was carried out on Intel(R) Core(TM) i5-3570 CPU at 3.4 GHz with 4 GB RAM. EPANET [1] was used as a hydraulic analysis program.

4.2. Parameter Settings. The number of decision variables, which should be determined through optimization, is 356 because there are 356 pipelines in the target water supply network. As indicated in Table 2, 18 pipe diameters were considered for the target water supply network. Hence, the number of possible solutions that can be considered during the design period is infinite, as mentioned in Table 3.

The parameters applied in the present program for the Saemangeum target water supply network are listed in Table 4. The size of the harmony memory (HMS), the value of the HMCR parameter, and the value of PAR were set to 30, 0.97, and 0.01, respectively.

These values, which correspond to the optimum results, are adjusted; therefore, the convergence time and efficiency of the optimal solution vary. However, when there are many

TABLE 4: Cost data based on pipe diameters as applied to Saemangeum.

Control parameters	Set value
HMS	30
HMCR	0.97
PAR	0.01
Constraint condition (pressure, h)	$10 < h < 35$
Constraint condition (pipe velocity, v)	$0.01 < v < 2.5$

decision variables, and in such a case, if large HMCR and small PAR values are used, the efficiency of the optimization generally increases.

4.3. The Economic Feasibility of the Initial Design and Hydraulic Analysis Evaluation. To compare and evaluate the optimization results of the pipe diameters for the initial design, the cost results and hydraulic analysis results of the initial design were first reviewed according to Pseudocode 1; the results of this review are listed in Tables 5 and 6. The equalization of the nodal heads and the economical velocity corresponding to each pipe diameter are generally used as

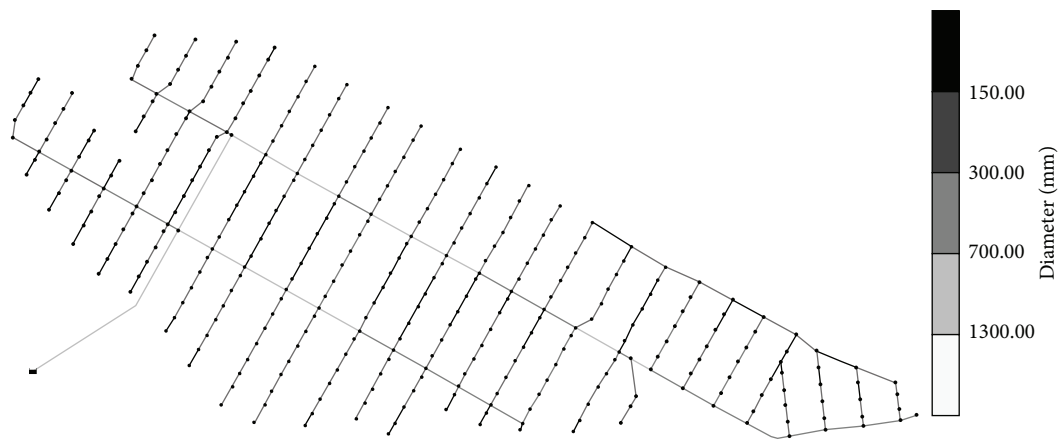


FIGURE 4: Pipe diameter optimization results for the six zones of the Saemangeum water supply network.

TABLE 5: Comparisons of the costs incurred upon applying the optimal design versus the initial design.

Target water supply network	Initial design cost (₩)	Optimal design cost (₩)	Variation (%)
Six zones of Saemangeum (looped type)	11,200,114,720	10,182,733,295	-9.08

the factors in evaluating the mathematical stability of an irrigation system.

The minimum nodal pressure head is mostly stable at a value greater than 10 m. In the present initial design, a looped network irrigation system is implemented by installing an additional pipeline to a branched network system. In this case, the supply path up to the demand node is determined to be a branched network, that is, only a single type.

However, in the initial design, because various supply paths are possible, the head loss is slight, and a water supply is possible through the hydraulically satisfied supply paths, a system that is more hydraulically stable than a branched network system that can be implemented. Thus, because various supply paths are possible in a looped irrigation water supply system, a looped system provides a better water supply than a branched system during abnormal operating conditions such as during an irrigation path failure or closure.

4.4. Optimal Pipe Diameter Design Results. The pipe diameter was optimized by considering the pressure and pipe velocity constraint conditions and the HS parameters, which were explained earlier in this study. The optimization results from a cost-effective pipe diameter are shown in Figure 4.

The statistical values of the nodal pressure head and pipeline velocities, which are the results of a hydraulic analysis based on cost-effective pipe diameter and the optimal cost results, are shown in Tables 5 and 6. Overall, the pressure head and pipe velocities were confirmed to be stable, and a comparison based on the hydraulic stability and economic feasibility of the initial design was conducted.

The application results indicate that the cost reduction rate of the optimal design was considerably greater (9.08%) than that of the initial design. These results were further analyzed from the viewpoint of current practices that do not

employ optimization techniques; this analysis indicates that even without using any optimization technique, branched network systems that do not significantly differ from the optimal designs can be created using the current techniques.

However, in the case of a looped network system, such as the water supply network applied in this study, the differences in the results were significant; therefore, it is necessary to determine an cost-effective pipe diameter for the optimization technique based on the results obtained when employing current practices. The hydraulic analysis results indicate that the minimum pressure head (more than 10 m) was mostly satisfied, as observed in the initial design. Furthermore, the statistical values of the nodal pressure head and pipe velocity indicate that the minimum pressure head, allowable pipe velocity, and average pipe velocity all satisfy the economical pipe velocity requirements.

5. Differences from Other Existing Plans

In the present study, optimal design reviews of two other design plans in addition to the proposed looped network design plan were conducted. These two design plans are of a branch type and a pump type, as shown in Figures 5 and 6, respectively.

The branch-type water supply network comprises 335 pipelines, with a total length of 37.88 km. The pump-type water supply network comprises 345 pipelines; for the water supplied by the pumping of this irrigation network, the entire area encompassing the six zones was reclassified into four new areas. The total length of the pipelines is approximately 41.39 km.

To compare and evaluate the estimation results for the optimal pipe diameter of the three water supply network systems, that is, the loop type (plan 1), branch type (plan 2),

TABLE 6: Analysis results of the optimal and initial hydraulic designs (based on statistical values of the nodal head and pipe velocity).

Target water supply network	Nodal pressure head (m)				Pipe velocity (m/s)			
	Min.	Max.	Avg.	Var.	Min.	Max.	Avg.	Var.
Six zones of Saemangeum (looped type)	17.65	31.66	23.04	13.95	0.01	1.92	0.97	0.16
Optimal design	10.00	29.08	15.36	23.68	0.02	2.46	1.18	0.29

TABLE 7: Optimal design results and cost comparison of the initial plan (three cases).

Target water supply network	Initial design costs (₩)	Optimal design costs (₩)	Variation (%)
Loop type (plan 1)	11,200,114,720	10,182,733,295	-9.08
Branch type (plan 2)	10,484,719,750	10,044,962,405	-4.19
Pump type (plan 3)	11,503,515,255	11,586,379,380	+0.72

TABLE 8: Analysis results of the optimal and initial hydraulic designs (three cases).

Target water supply network		Nodal pressure head (m)				Pipe velocity (m/s)			
		Min.	Max.	Avg.	Var.	Min.	Max.	Avg.	Var.
Loop type (plan 1)	Initial plan	17.65	31.66	23.04	13.95	0.01	1.92	0.97	0.16
	Optimal design	10.00	29.08	15.36	23.68	0.02	2.46	1.18	0.29
Branch type (plan 2)	Initial plan	10.45	31.66	21.24	23.55	0.09	2.22	1.11	0.09
	Optimal design	10.00	29.08	14.28	20.63	0.15	2.40	1.08	0.30
Pump type (plan 3)	Initial plan	0.5	30.79	25.17	10.63	0.07	1.89	0.95	0.06
	Optimal design	10.00	30.79	16.14	29.26	0.22	2.49	1.36	0.25

and pump type (plan 3), the cost results according to the final optimum pipe diameter and the pipe diameters of the initial plan of each of the three networks are listed in Table 7.

The results indicate that the cost of applying the optimal design was at a minimum for plan 2 and at a maximum for plan 3. This is similar to the trends found in the initial plan. However, an examination of the varying cost rate shows that the cost reduction of the optimal design for plan 2 was 4.19% less than that of the initial plan. On the other hand, the cost increased by 0.72% for plan 3, whereas in the case of plan 1, the cost reduction rate was very high (9.08%). The results for plan 1 show that the reduction rate between the optimal cost and the total length of the pipes is inversely proportional when the pressure head and velocity conditions remain constant. Moreover, a looped irrigation system has many nodes and pipes, which vary hydraulically because pipes of different diameters are used in a pipe system; this proves that it is difficult to design a looped irrigation system economically without using an optimization technique.

These results are attributed to the fact that the self-nodal pressure head of the initial version of plan 1 is relatively greater than that of the initial version of plan 2. However, from the viewpoint of current practices, which do not employ optimization techniques, branch-type systems such as plans 2 and 3, which do not differ greatly from optimal systems, can be designed by applying current techniques. In the case of a looped network system such as plan 1, the differences between the results corresponding to the initial and optimal designs were considerable. Therefore, based on the results

from current practices, it is necessary to determine a cost-effective pipe diameter using an optimization technique.

The results of a hydraulic analysis in which the optimal pipe diameters for plans 1, 2, and 3 were considered are shown in Table 8. The statistical values of the nodal pressure head and pipe velocity indicate that the minimum pressure head, allowable pipe velocity, and average pipe velocity for all three plans satisfy the economical pipe velocity requirements. An examination of the nodal pressure head confirms that the minimum pressure head (10 m) is mostly stable in plans 1 and 2, as is the case of the initial plan. In the case of plan 3, the minimum pressure for the initial plan was very low (0.5 m); however, the cost increases if the minimum pressure of the initial plan (0.5 m) exceeds the minimum pressure standards (10 m) during the optimal design process.

A comparison of the three optimal design types shows that plan 2 (branch type) is the most economic optimal design based only on the criterion of minimum costs. However, because plan 2 does not differ greatly from plan 1 in terms of costs, it is necessary to derive the final design results by considering the hydraulic and maintenance aspects. Plan 1 is a case in which a looped network irrigation system is implemented by installing additional pipelines to plan 2, which is a branched system.

If the pipelines supplied up to the demand node correspond to plan 2 (branch network type), the supply path is determined to be of only one type. However, in the case of plan 1, many supply paths are present; the water supply is made possible through the supply paths, which are

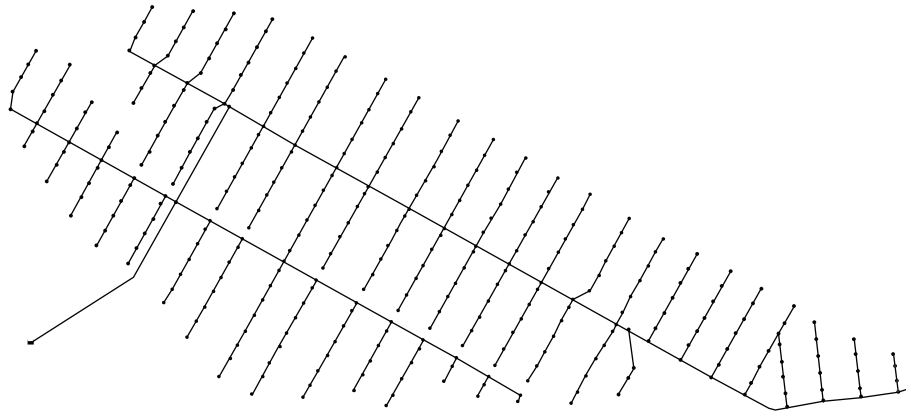


FIGURE 5: Branch-type system.

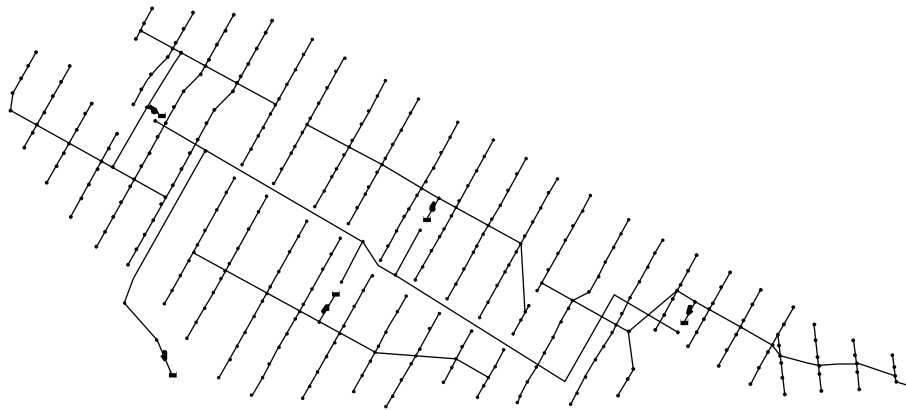


FIGURE 6: Pump-type system.

hydraulically satisfactory. Therefore, plan 1, which is a more hydraulically stable system than plan 2, can be implemented.

Thus, the supply of a looped irrigation water supply system during abnormal situations such as an irrigation path failure or closure is better than that of a branched irrigation water supply system because the former has various supply paths. Unlike plans 1 and 2, plan 3 was designed by reclassifying the target pipeline system into four hydraulically independent sections, and water was supplied to each section through pumping heads. By dividing the target pipeline system into four hydraulically independent sections, the fluctuations in the water quantities by each area can be more effectively and reasonably handled, and plan 3 can respond to future pipeline maintenance and expansion plans. However, the increased use of pumps can cause maintenance difficulties and an increase in maintenance costs.

6. Conclusions

In the present study, the HS algorithm, which is one of the latest optimization techniques, was introduced in the design of an agricultural irrigation system, and a corresponding program was developed. The developed program was applied to the actual target area (Saemangeum business area, zone

6), and the results were presented in this paper. Currently used methods have disadvantages in that the pipe diameter has to be adjusted through a hydraulic calculation of the given water supply network, and this process has to be repeated until satisfactory results are obtained. Unlike this calculation method, the model presented herein yields results that automatically meet the hydraulic conditions through the combined use of the HS algorithm and a hydraulic analysis. Hence, a comparative analysis is simple and effective. The results obtained by applying this method to an actual large-scale water supply network are better than those obtained using existing mathematical algorithms even after considering the nonlinearity, which is inevitable during the analysis. The calculation results of the optimal construction costs and the pipe diameter when applying the proposed model to the actual target region (Saemangeum business area zone 6) indicate that the optimal design results obtained using HS yield much better results (9%) in terms of cost than those of the presently utilized economic pipe diameter calculation techniques. In particular, the optimization technique was found to be more necessary in the optimal design of a looped network irrigation system than for a branched network irrigation system. Furthermore, an examination of the hydrological factors of a pipeline system in which cost-effective pipe

diameters were applied showed that based on the statistical values of the head and pipe velocity, the minimum pressure head, the allowable pipe velocity, and the average pipe velocity all satisfy the requirements of an economical pipe velocity. Therefore, if the benefits of the proposed model are proven through application in future systems, it will show the model to be a useful decision-making tool for designing looped network water supply systems.

Conflict of Interests

The authors declare that there is no conflict of interests regarding the publication of this paper.

Acknowledgment

This work was supported by the National Research Foundation of Korean (NRF) Grant funded by the Korean Government (MSIP) (NRF. 2013RIA2A1A01013886).

References

- [1] Rossman, *EPANET 2.0 User's Manual*, EPA, 2000.
- [2] Bentley, *Water GEMS User's Manual*, 2007.
- [3] E. Alperovits and U. Shamir, "Design of optimal water distribution systems," *Water Resources Research*, vol. 13, no. 6, pp. 885–900, 1977.
- [4] G. E. Quindry, E. D. Brill, and J. C. Liebman, "Optimization of looped water distribution systems," *Journal of the Environmental Engineering Division*, vol. 107, no. 4, pp. 665–679, 1981.
- [5] O. Fujiwara and D. B. Khang, "A two-phase decomposition method for optimal design of looped water distribution networks," *Water Resources Research*, vol. 26, no. 4, pp. 539–549, 1990.
- [6] G. Eiger, U. Shamir, and A. Ben-Tal, "Optimal design of water distribution networks," *Water Resources Research*, vol. 30, no. 9, pp. 2637–2646, 1994.
- [7] J. Reca, J. Martínez, C. Gil, and R. Baños, "Application of several meta-heuristic techniques to the optimization of real looped water distribution networks," *Water Resources Management*, vol. 22, no. 10, pp. 1367–1379, 2008.
- [8] M. J. Monem and R. Namdarian, "Application of simulated annealing (SA) techniques for optimal water distribution in irrigation canals," *Irrigation and Drainage*, vol. 54, no. 4, pp. 365–373, 2005.
- [9] M. da Conceição Cunha and L. Ribeiro, "Tabu search algorithms for water network optimization," *European Journal of Operational Research*, vol. 157, no. 3, pp. 746–758, 2004.
- [10] A. C. Zecchin, A. R. Simpson, H. R. Maier, M. Leonard, A. J. Roberts, and M. J. Berrisford, "Application of two ant colony optimisation algorithms to water distribution system optimisation," *Mathematical and Computer Modelling*, vol. 44, no. 5-6, pp. 451–468, 2006.
- [11] Z. W. Geem, J. H. Kim, and G. V. Loganathan, "A new heuristic optimization algorithm: harmony search," *Simulation*, vol. 76, no. 2, pp. 60–68, 2001.
- [12] I. Montalvo, J. Izquierdo, R. Perez, and M. M. Tung, "Particle swarm optimization applied to the design of water supply systems," *Computers & Mathematics with Applications*, vol. 56, no. 3, pp. 769–776, 2008.
- [13] A. Bolognesi, C. Bragalli, A. Marchi, and S. Artina, "Genetic heritage evolution by stochastic transmission in the optimal design of water distribution networks," *Advances in Engineering Software*, vol. 41, no. 5, pp. 792–801, 2010.
- [14] F. Zheng, A. R. Simpson, and A. C. Zecchin, "A combined NLP-differential evolution algorithm approach for the optimization of looped water distribution systems," *Water Resources Research*, vol. 47, no. 8, Article ID W08531, 2011.
- [15] A. Sedki and D. Ouazar, "Hybrid particle swarm optimization and differential evolution for optimal design of water distribution systems," *Advanced Engineering Informatics*, vol. 26, no. 3, pp. 582–591, 2012.
- [16] R. Sheikholeslami, A. Kaveh, A. Tahershamsi, and S. Talatahari, "Application of charged system search algorithm to water distribution networks optimization," *International Journal of Optimization in Civil Engineering*, vol. 4, no. 1, pp. 41–58, 2014.
- [17] A. de Corte and K. Sörensen, "Optimisation of gravity-fed water distribution network design: a critical review," *European Journal of Operational Research*, vol. 228, no. 1, pp. 1–10, 2013.
- [18] K-Water, *Water Facilities Construction Cost Estimation Report*, K-Water, 2010.

Research Article

Conceptual Comparison of Population Based Metaheuristics for Engineering Problems

Oluwole Adekanmbi and Paul Green

Department of Finance and Information Management, Durban University of Technology, P.O. Box 101112, Scottsville, Pietermaritzburg 3209, South Africa

Correspondence should be addressed to Oluwole Adekanmbi; adekanmbioluwole@gmail.com

Received 24 October 2014; Revised 28 December 2014; Accepted 30 December 2014

Academic Editor: Fei Kang

Copyright © 2015 O. Adekanmbi and P. Green. This is an open access article distributed under the Creative Commons Attribution License, which permits unrestricted use, distribution, and reproduction in any medium, provided the original work is properly cited.

Metaheuristic algorithms are well-known optimization tools which have been employed for solving a wide range of optimization problems. Several extensions of differential evolution have been adopted in solving constrained and nonconstrained multiobjective optimization problems, but in this study, the third version of generalized differential evolution (GDE) is used for solving practical engineering problems. GDE3 metaheuristic modifies the selection process of the basic differential evolution and extends DE/rand/1/bin strategy in solving practical applications. The performance of the metaheuristic is investigated through engineering design optimization problems and the results are reported. The comparison of the numerical results with those of other metaheuristic techniques demonstrates the promising performance of the algorithm as a robust optimization tool for practical purposes.

1. Introduction

In structural engineering, most design optimization problems are highly nonlinear consisting of different design variables and complex constraints such as displacements, geometrical configuration, stresses, and load carrying capability. The design variables are normally grouped into two categories, namely, continuous variables and discrete variables. Optimization problems involving continuous and discrete variables generally require problem-specific search techniques [1]. Evolutionary multiobjective optimization techniques are examples of problem-specific search techniques. Several literatures have applied evolutionary multiobjective optimization techniques to solving multiobjective optimization problems to find a set of trade-off optimal solutions. Since most engineering problems involve multiobjective optimization, it is appropriate to apply an evolutionary optimization algorithm to solve them.

In the last two decades, different types of techniques aimed at effectively and efficiently exploring a search space by combining several basic heuristic methods have emerged [2–4]. These techniques currently referred to as “*Metaheuristics*” are used to describe heuristic methods applied to solving different practical problems. *Metaheuristics* can be considered

as a global algorithmic framework used in solving several optimization problems with little changes, thereby making the algorithm adaptive to the specific problem [5].

Metaheuristic search techniques, such as simulated annealing (SA) [6], genetic algorithm (GA) [7], evolution strategies (ESs) [8], and particle swarm optimization (PSO) [9], which are generally developed based on natural phenomena have become the popular optimization techniques of recent years due to their capability of finding promising solutions for complicated optimization problems as well as their independence to the derivatives of objective functions.

Furthermore, metaheuristics can handle both discrete and real-valued variables and can be applied to a wide range of optimization problems effectively. Basically, both trajectory and population based metaheuristic approaches aim to locate the global optimum in the solution space through random moves. The key difference between the metaheuristics is in the way they propose the next move in the solution space. This motivates developers of optimization algorithms to find more efficient methodologies for originating robust optimization algorithms. However, sometimes this results in complicated approaches which are difficult to understand and implement. Hence, this study is an attempt

to test the simplicity and efficiency methodology of GDE3 metaheuristics in solving engineering optimization purposes. Section 2 describes the GDE3 metaheuristics briefly. Test cases are described and optimization results are discussed in Section 3. Section 4 provides a clear conclusion of the study.

2. Generalized Differential Evolution Metaheuristic

Several extensions of differential evolution [26] exist for solving constrained and nonconstrained multiobjective optimization problems [27, 28]. In comparison to the extension of differential evolution (DE), GDE3 makes differential evolution a suitable algorithm for multiobjective optimization as well as constrained optimization with little changes to the basic differential evolution algorithm. GDE3 extends DE/rand/1/bin strategy which exhibit slow convergence rates and strong exploration properties. GDE3 is a third version of generalized differential evolution modifying the selection process of the basic differential evolution algorithm [29]. The selection process in GDE3 is guided by these three rules:

- (i) In a scenario where both the old vector and trial vector are infeasible, the old vector is selected if it dominates the trial vector, but if the trial vector weakly dominates the old vector, then the trial vector is selected.
- (ii) Feasible vector is selected in a situation where both feasible and infeasible vectors are generated.
- (iii) In a scenario where both the old vector and trial vector are feasible, the old vector is selected if it dominates the trial vector, but if the trial vector weakly dominates the old vector, then the trial vector is selected.

The whole GDE3 is presented in Algorithm 1. Parts that are new compared to previous GDE versions are framed in Algorithm 1. Without these parts, the algorithm is identical to GDE1. GDE3 can be seen as a combination of GDE2 and Pareto Differential Evolution Approach (PDEA). GDE3 is similar to differential evolution for multiobjective optimization (DEMO) except that DEMO does not contain constraint handling nor recede to basic DE in the case of a single objective because DEMO modifies the basic DE and does not consider weak dominance in the selection. Moreover, GDE3 has an improved diversity maintenance compared to DEMO. There are no constraints to be evaluated when $K = 0$ and $M = 1$, and the selection is simply

$$x_{i,G+1} = \begin{cases} u_{i,G}, & \text{if } f(u_{i,G}) \leq f(x_{i,G}), \\ x_{i,G}, & \text{otherwise.} \end{cases} \quad (1)$$

This is the same as for the basic DE algorithm. The size of the population does not increase since this requires that $x_{i,G}$ and $u_{i,G}$ do not dominate each other even weakly, but in the case of a single objective, the reverse is the case. GDE3 performs the sorting of the vector by calculating the crowding distance of the vector. The selection process

based on crowding distance gives GDE3 an advantage over NSGAI. In the case of comparing feasible, incomparable, and nondominating solutions, both offspring and parent vectors are saved for the population of the next generation [4]. There is no need to remove elements, since the population size does not increase. Hence, GDE3 is identical to basic DE in this case. GDE3 improves the ability to handle multiobjective optimization problems by giving a better distributed set of solutions and are less sensitive to the selection of control parameter values compared to the earlier GDE versions. As a result, this procedure reduces the computational costs of the metaheuristic and improves its efficiency. Readers interested in GDE3 should refer to the texts by [30, 31].

3. Implementation of Engineering Optimization Problems

The metaheuristic optimization was implemented in NET-BEAN v7.3; optimization runs were executed on an HP PC with a 2.30 GHz Intel Dual Core processor and 4 GB of RAM memory. Different examples taken from several optimization literatures were used to show the performance of GDE3 metaheuristic. These examples have been previously solved using a variety of other techniques, which is useful to show the validity and effectiveness of the GDE3 metaheuristic. The optimal results were compared with data recently published in literatures. An experiment has been performed to determine the best values of F and CR for better performance in GDE3 metaheuristic. For this purpose, both CR and F are varied from 0.1 to 1 with an increment of 0.1. The simulations were conducted for each value of F with respect to all values of CR. Hence, 100 such simulations were conducted. From the results, it was found that better Pareto optimal front is obtained by GDE3 with $F = 0.5$, CR = 0.9 and the termination condition is set to the 10,000 objective function evaluations.

Example 1 (welded beam design optimization problem). The welded beam problem is designed to minimize the fabrication cost by subjecting it to some constraints such as bending stress (σ), shear stress (τ), end deflection (δ), and buckling load (P_c). The design variables of the optimization problem are the thickness of the beam (b), the thickness of the weld (h), the welded joint length (l), and the beam width (t). Figure 1 shows the welded beam design structure.

The values of l and h must be integer multiples of 0.0065 in. Assuming $x_1 = h$, $x_2 = l$, $x_3 = t$, and $x_4 = b$ as design variables, the optimization problem can be mathematically expressed as follows:

$$\begin{aligned} \text{Minimize } f(\vec{x}) &= (1 + C_1)x_1^2x_2 \\ &\quad + C_2x_3x_4(14.0 + x_2), \end{aligned}$$

$$\begin{aligned} \text{Subject to } g_1(\vec{x}) &= \tau(\vec{x}) - \tau_{\max} \leq 0, \\ g_2(\vec{x}) &= \sigma(\vec{x}) - \sigma_{\max} \leq 0, \\ g_3(\vec{x}) &= x_1 - x_4 \leq 0, \end{aligned}$$

```

Input:  $D, G_{max}, NP \geq 4, F \in (0, 1+], CR \in [0, 1]$ , and initial bounds:  $x^{(lo)}, x^{(hi)}$ 
Initialize:  $\begin{cases} \forall i \leq NP \wedge \forall j \leq D: x_{j,i,0} = x_j^{(lo)} + rand_j[0, 1] \cdot (x_j^{(hi)} - x_j^{(lo)}), \\ i = \{1, 2, \dots, NP\}, j = \{1, 2, \dots, D\}, G = 0, rand_j[0, 1] \in [0, 1] \end{cases}$ 
While  $G < G_{max}$ 
 $\forall i \leq NP$ 
    Mutation and recombine:
     $r_1, r_2, r_3 \in \{1, 2, \dots, NP\}$ , randomly selected,
    except mutually different and different from  $i$ 
     $j_{rand} \in \{1, 2, \dots, D\}$ , randomly selected from each  $i$ 
     $\forall j \leq D, u_{j,i,G} = \begin{cases} x_{j,r_3,G} + F \cdot (x_{j,r_1,G} - x_{j,r_2,G}) \\ \text{if } rand_j[0, 1] < CR \vee j == j_{rand} \\ x_{j,r_1,G} \end{cases}$ 
    Select:
     $x_{i,G+1} = \begin{cases} u_{i,G} & \text{if } f(u_{i,G}) \leq f(x_{i,G}) \\ x_{i,G} & \text{otherwise} \end{cases}$ 
    Set:  $n = n + 1$ 
     $x_{NP+n,G+1} = u_{i,G}$  if  $\begin{cases} \forall j: g_j(u_{i,G}) \leq 0 \\ \wedge \\ x_{i,G+1} == x_{i,G} \\ \wedge \\ x_{i,G} \nprec u_{i,G} \end{cases}$ 
while  $n > 0$ 
    Select  $x \in \rho = \{x_{1,G+1}, x_{2,G+1}, \dots, x_{NP+n,G+1}\}$ ;
     $\begin{cases} x \text{ belongs to the last non-dominated set of } \rho \\ \wedge \\ x \text{ is the most crowded in the last non-dominated set} \end{cases}$ 
    Remove  $x$  from  $\rho$ 
     $n = n - 1$ 
     $G = G + 1$ 

```

ALGORITHM 1: The GDE3 algorithm [29].

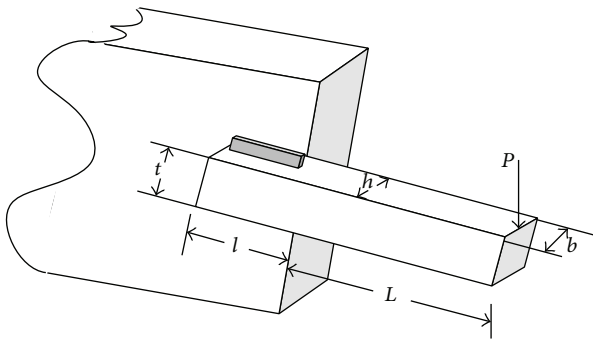


FIGURE 1: Schematic of the welded beam design problem [1].

$$\begin{aligned}
 g_4(\vec{x}) &= C_1(x_1^2) \\
 &\quad + C_2x_3x_4(14.0 + x_2) - 5.0 \leq 0, \\
 g_5(\vec{x}) &= 0.125 - x_1 \leq 0, \\
 g_6(\vec{x}) &= \delta(\vec{x}) - \delta_{max} \leq 0, \\
 g_7(\vec{x}) &= P - P_c \leq 0,
 \end{aligned}$$

(2)

where

$$\tau(\vec{x}) = \sqrt{(\tau')^2 + (2\tau'\tau'') \frac{x_2}{2R} + (\tau'')^2},$$

$$\tau'' = \frac{MR}{J},$$

$$M = P \left(L + \frac{x_2}{2} \right),$$

$$R = \sqrt{\frac{x_2^2}{4} + \left(\frac{x_1 + x_3}{2} \right)^2},$$

$$J = 2 \left\{ \sqrt{2}x_1x_2 \left[\frac{x_2^2}{12} + \left(\frac{x_1 + x_3}{2} \right)^2 \right] \right\},$$

$$\sigma(\vec{x}) = \frac{6PL}{x_4x_3^2},$$

$$\tau' = \frac{P}{\sqrt{2}x_1x_2},$$

$$\delta(\vec{x}) = \frac{4PL^3}{Ex_3^3x_4},$$

$$P_c(\vec{x}) = \frac{4.013E\sqrt{x_3^2x_4^6/36}}{L^2} \left(1 - \frac{x_3}{2L} \sqrt{\frac{E}{4G}} \right).$$

(3)

TABLE 1: Values of parameters involved in the formulation of the welded beam problem [1].

Constant item	Description	Values
C_1	The welded material	0.10471 (\$/in ³)
C_2	The bar stock	0.04811 (\$/in ³)
τ_{\max}	Shear stress of the welded material	13600 (psi)
σ_{\max}	Normal stress of the bar material	30000 (psi)
δ_{\max}	Bar end deflection	0.25 (inch)
E	Young's modulus of bar stock	30×10^6 (psi)
G	Shear modulus of bar stock	12×10^6 (psi)
P	Loading condition	6000 (lb)
L	Beam's projection length	14 (inch)

The simple bounds of the problem are $x_1, x_4 \in [0.1, 2.0]$ and $x_2, x_3 \in [0.1, 10.0]$. The values of parameters involved in the formulation of the welded beam problem are also shown in Table 1.

The optimum design of the welded beam is executed using GDE3 metaheuristic, and the best solution is found as $x^* = \{x_1, x_2, x_3, x_4\} = \{0.20572840999876, 3.47072911158159, 9.03661683005891, 0.20572540074781\}$ which yields an objective function value of $f(\vec{x}) = 1.7248496$ as seen in Table 2.

The results obtained by GDE3 are presented in Table 2. GDE3 found the global optimum requiring 400 iterations (i.e., 10,000 evaluations) per optimization run. Table 3 provides a comparison of this solution with the results of other optimization algorithms. It is apparent from the table that GDE3 metaheuristic finds a competitive solution using only 10,000 evaluations which is considerably lesser than those of other approaches. Further, a statistical evaluation of 100 independent runs of the GDE3 metaheuristic is tabulated in Table 4 considering the best, worst, average, and the standard deviation (std. dev.) of the obtained solutions. The ratio between the optimized costs corresponding to best and worst designs is 1.00042. Remarkably, GDE3 produced the overall best design result with a value of 1.724849. For continuous optimization problem, [20, 22] found a better design result with a value of 1.7248 at a higher function evaluation.

Example 2 (pressure vessel optimization problem). The pressure vessel problem is designed to minimize total cost which is comprised of the welding cost and forming material cost. The compressed air tank with a working pressure of 3000 psi and a minimum volume of 750 ft³ must be designed according to the ASME code on boilers and pressure vessels. The design variables of the optimization problem are the length of the cylindrical segment of the vessel (L), the thickness of the cylindrical skin (T_s), the inner radius (R), and the thickness of the spherical head (T_h).

The variables T_s and T_h are discrete values which are integer multiples of 0.0625 inches. Figure 2 shows the cylindrical pressure vessel capped at both ends by hemispherical heads.

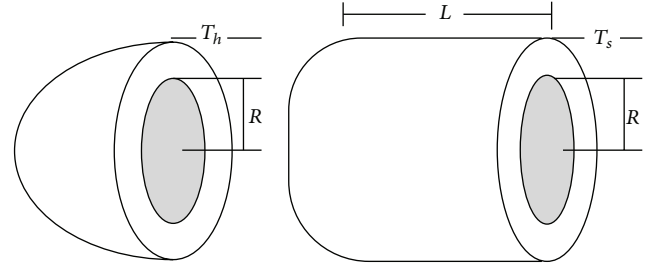


FIGURE 2: Schematic of the pressure vessel design problem [1].

Assuming $x_1 = T_s, x_2 = T_h, x_3 = R$, and $x_4 = L$ as the design variables, the optimization problem can be mathematically expressed as follows:

$$\begin{aligned}
 \text{Minimize } f(\vec{x}) &= 0.6224x_1x_3x_4 + 1.7781x_2x_3^2 \\
 &\quad + 3.1611x_1^2x_4 + 19.8621x_1^2x_3, \\
 \text{Subject to } g_1(\vec{x}) &= 0.0193x_3 - x_1 \leq 0, \\
 g_2(\vec{x}) &= 0.00954x_3 - x_2 \leq 0, \\
 g_3(\vec{x}) &= x_4 - 240 \leq 0, \\
 g_4(\vec{x}) &= 750 \times 1728 - \pi x_3^2 x_4 \\
 &\quad - \frac{4}{3}\pi x_3^3 \leq 0.
 \end{aligned} \tag{4}$$

The simple bounds of the problem are $x_1, x_2 \in [1 \times 0.0625, 99 \times 0.0625]$ and $x_3, x_4 \in [10.0, 240.0]$. Unlike the usual limit of 200 in considered in literatures, the upper bound of design variable L was increased to 240 in to expand the search space.

Optimization results are presented in Table 5. GDE3 produced a design result with a value of 6083.773 within 400 iterations (i.e., 10,000 evaluations). Table 6 compares the optimal design results produced by GDE3 with those reported in [1, 17, 20, 21, 24, 32]. Further, a statistical evaluation of 100 independent runs of the GDE3 metaheuristic is tabulated in Table 7 considering the best, worst, average, and the standard deviation (std. dev.) of the obtained solutions. The ratio between the optimized costs corresponding to worst and best designs is 1.00229. The best design result was produced by the Firefly algorithm. GDE3 metaheuristic produced the least performance compared to the other algorithms.

Example 3 (speed reducer design optimization problem). The speed reducer design problem [25] is designed to minimize the weight of the speed reducer subjecting it to some constraints such as shaft stresses, surface stress, gear teeth bending stress, and shafts crosswise deflections. The width of the gear face x_1 , teeth module x_2 , number of pinion teeth x_3 , first shaft length between bearings x_4 , second shaft length between bearings x_5 , the diameter of the first shaft x_6 , and diameter of the second shaft are the design variables of the

TABLE 2: GDE3 solution vector for welded beam.

	x_1	x_2	x_3	x_4
Best solution	0.20572840999876	3.47072911158159	9.03661683005891	0.20572540074781
	$g_1(\vec{x})$	$g_2(\vec{x})$	$g_3(\vec{x})$	$g_4(\vec{x})$
	-0.66062798472194	0.665171394633944	3.00925094998E - 06	-3.43299575416113
	$g_5(\vec{x})$	$g_6(\vec{x})$	$g_7(\vec{x})$	$f(\vec{x})$
	-0.08072840999876	-0.235539990649711	0.373971078704926	1.72484969509211

TABLE 3: Welded beam problem: comparison of GDE3 results with other optimization methods.

Researcher	Metaheuristic	x_1	x_2	x_3	x_4	$f(x)$	NE
[10]	Genetic algorithm	0.2489	6.1730	8.1789	0.2533	2.4331	320,080
[11]	Genetic algorithm	0.2489	6.1097	8.2484	0.2485	2.4000	6,273
[12]	Social behavioral model	0.2407	6.4851	8.2399	0.2497	2.4426	19,259
[13]	Society and civilization algorithm	0.2444	6.2380	8.2886	0.2446	2.3854	33,095
[14]	Genetic algorithm	0.2443	6.2117	8.3015	0.2443	2.3816	320,000
[15]	Particle swarm optimization	0.2444	6.2175	8.2915	0.2444	2.3810	30,000
[16]	Harmonic search	0.2442	6.2231	8.2915	0.2443	2.3810	110,000
[17]	Simulated annealing—direct search	0.2444	6.2158	8.2939	0.2444	2.3811	56,243
[18]	Simulated annealing—genetic algorithm	0.2231	1.5815	12.8468	0.2245	2.2500	26,466
[19]	Artificial Immune System—genetic algorithm	0.2444	6.2183	8.2912	0.2444	2.3812	320,000
[20]	Harmonic search	0.2057	3.4705	9.0366	0.2057	1.7248	200,000
[21]	Simple constrained particle swarm optimizer	0.2057	3.4705	9.0366	0.2057	1.7249	24,000
[22]	Harmonic search—sequential quadratic programming	0.2057	3.4706	9.0368	0.2057	1.7248	90,000
[23]	Differential evolution	0.2444	6.2175	8.2915	0.2444	2.3810	24,000
[8]	Evolutionary algorithm	0.2443	6.2201	8.2940	0.2444	2.3816	28,897
[1]	Firefly algorithm	0.2015	3.5620	9.0414	0.2057	1.7312	50,000
[24]	Simple optimization	0.2057	3.4705	9.0366	0.2057	1.7246	10,000
Present study	Generalized differential evolution 3	0.2057	3.4707	9.0366	0.2057	1.724849	10,000

TABLE 4: Statistical results of the GDE3 optimization.

Best	Average	Worst	Std. dev.	Number of iterations
1.724849	1.725023	1.725569	0.0001018	400

TABLE 5: GDE3 Solution vector for pressure vessel.

	x_1	x_2	x_3	x_4
Best Solution	0.74395291436715	0.36774755668330	38.5288195380221	239.37719314082
	$g_1(\vec{x})$	$g_2(\vec{x})$	$g_3(\vec{x})$	$g_4(\vec{x})$
	-0.00034669728332	-0.00018261829057	-0.62280685917400	-42.436889517499
	$f(\vec{x})$			
	6083.77328355025			

TABLE 6: Pressure vessel problem: comparison of GDE3 results with optimization methods.

Researcher	Metaheuristic	x_1	x_2	x_3	x_4	$f(x)$
[17]	Simulated annealing—direct search	0.7683	0.3797	39.8096	207.2250	5868.76
[32]	Particle swarm optimization—genetic algorithm	0.7500	0.3750	38.8601	221.3654	5850.383
[20]	Harmonic search	0.7500	0.3750	38.8600	221.3600	5849.7
[21]	Simple constrained particle swarm optimizer	0.8125	0.4375	42.0980	176.6360	6.059.714
[1]	Firefly algorithm	0.7500	0.3750	38.8600	221.3600	5850.3
[24]	Simple optimization	1.1250	0.6250	58.2901	43.6927	7199.35
Present study	Generalized differential evolution 3	0.74391	0.36774	38.5288	239.377	6083.773

TABLE 7: Statistical results of the GDE3 optimization.

Best	Average	Worst	Std. dev.	Number of iterations
6083.773	6092.318	6097.725	40.32205	400

TABLE 8: GDE3 Solution vector for speed reducer.

	x_1	x_2	x_3	x_4
	3.5000000004788	0.7000000000000	17.0000000000000	7.3000000000000
	x_5	x_6	x_7	$g_1(\vec{x})$
	7.8000000000000	3.3502146664526	5.2866832298256	-0.07391528052456
Best Solution	$g_2(\vec{x})$	$g_3(\vec{x})$	$g_4(\vec{x})$	$g_5(\vec{x})$
	-0.197998527251663	-0.499172248315386	-0.9014716976203	-3.1892233298E - 10
	$g_6(\vec{x})$	$g_7(\vec{x})$	$g_8(\vec{x})$	$g_9(\vec{x})$
	-3.8408276559E - 11	-0.7025	-1.3680001575E - 10	-0.583333332763
	$g_{10}(\vec{x})$	$g_{11}(\vec{x})$	$f(\vec{x})$	
	-0.0513257534686439	-0.0108523650245949	2996.34816529042	

TABLE 9: Speed reducer problem: comparison of generalized differential evolution 3 results with simple constrained particle swarm optimization.

Solution	Simple constrained particle swarm optimization [21]	Generalized differential evolution (Present study)
x_1	3.5000	3.5000
x_2	0.7000	0.7000
x_3	17.0000	17.0000
x_4	7.3000	7.3000
x_5	7.8000	7.8000
x_6	3.350214	3.3502146
x_7	5.286683	5.2866832
$f(\vec{x})$	2996.348165	2996.3481653

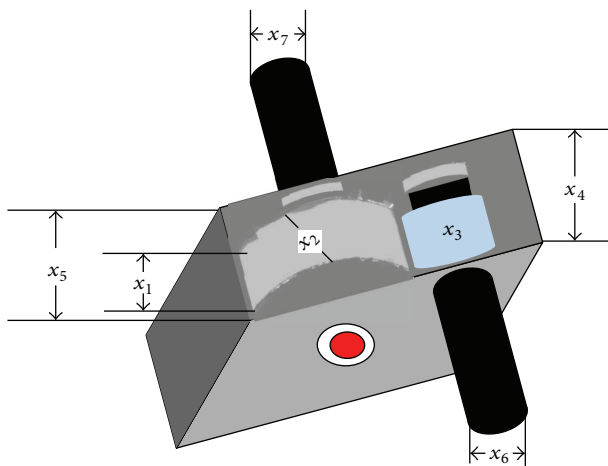


FIGURE 3: Schematic of the speed reducer design problem [25].

optimization problem. Figure 3 shows the schematic of the speed reducer.

The mathematical expression for the speed reducer problem is as follows:

$$\begin{aligned} \text{Minimize } f(\vec{x}) &= 0.7854x_1x_2^2 \\ &\cdot (3.3333x_3^2 + 14.9334x_3 \\ &\quad - 43.0934) \\ &\quad - 1.508x_1(x_6^2 + x_7^2) \\ &\quad + 7.4777(x_6^3 + x_7^3) \\ &\quad + 0.7854(x_4x_6^2 + x_5x_7^2), \end{aligned}$$

$$\text{Subject to } g_1(\vec{x}) = \frac{27}{x_1x_2^2x_3} - 1 \leq 0,$$

$$g_2(\vec{x}) = \frac{397.5}{x_1x_2^2x_3^2} - 1 \leq 0,$$

$$g_3(\vec{x}) = \frac{1.93x_4^3}{x_2x_3x_6^4} - 1 \leq 0,$$

$$g_4(\vec{x}) = \frac{1.93x_5^3}{x_2x_3x_7^4} - 1 \leq 0,$$

$$g_5(\vec{x}) = \frac{1.0}{110x_6^3}$$

$$\cdot \sqrt{\left(\frac{745.0x_4}{x_2x_3}\right)^2 + 16.9 \times 10^6} - 1 \leq 0,$$

$$g_6(\vec{x}) = \frac{1.0}{85x_7^3}$$

$$\cdot \sqrt{\left(\frac{745.0x_5}{x_2x_3}\right)^2 + 157.5 \times 10^6} - 1 \leq 0,$$

TABLE 10: Statistical results of the GDE3 optimization.

Best	Average	Worst	Std. dev.	Number of iterations
2996.3481653	2996.3483815	2996.3491534	0.0000021	400

TABLE 11: GDE3 Solution vector for tension/compression spring.

	x_1	x_2	x_3	$g_1(\vec{x})$
Best Solution	0.0517955276224998	0.359283196922392	11.1405163630287	-3.0601282864E - 05
	$g_2(\vec{x})$	$g_3(\vec{x})$	$g_4(\vec{x})$	$f(\vec{x})$
	-0.133636716257444	-4.05865278285946	-0.725947516970072	0.01266583600858

TABLE 12: Tension/compression spring problem: comparison of GDE3 results with simple constrained particle swarm optimization.

Solution	Simple constrained particle swarm optimization [21]	Generalized differential evolution 3
x_1	0.051583	0.0517955
x_2	0.354190	0.3592831
x_3	11.438675	11.140516
$f(\vec{x})$	0.012665	0.012665836

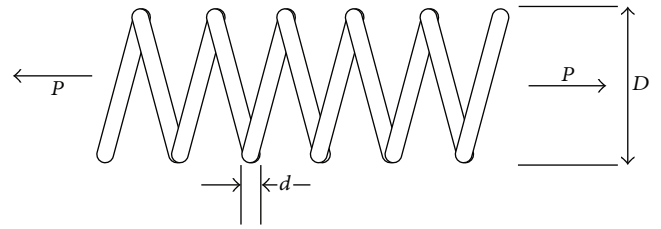


FIGURE 4: Schematic of the tension/compression spring design problem.

The ratio between the optimized costs corresponding to best and worst designs is 1.0000003. Remarkably, GDE3 produced the overall best design result with a value of 2996.3481653.

Example 4 (tension/compression spring design optimization problem). The tension/compression spring problem is designed to minimize the weight of the spring subjecting it to some constraints such as shear stress, minimum deflection, outside diameter limits, and surge frequency. The design variables are the number of active coils P , the diameter of the mean coil D , and the diameter of the wire d . Figure 4 shows the tension/compression spring design.

Assuming $x_1 = d$, $x_2 = D$, and $x_3 = P$, as the design variables, the tension/compression spring design problem can be expressed as follows:

$$\begin{aligned}
 &\text{Minimize } f(\vec{x}) = (x_3 + 2) x_2 x_1^2, \\
 &\text{Subject to } g_1(\vec{x}) = 1 - \frac{x_2^3 x_3}{71,785 x_1^4} \leq 0, \\
 &g_2(\vec{x}) = \frac{4x_2^2 - x_1 x_2}{12,566(x_2 x_1^3 - x_1^4)} + \frac{1}{5,108 x_1^2} - 1 \leq 0, \\
 &g_3(\vec{x}) = 1 - \frac{140.45 x_1}{x_2^2 x_3} \leq 0, \\
 &g_4(\vec{x}) = \frac{x_2 + x_1}{1.5} - 1 \leq 0.
 \end{aligned} \tag{6}$$

The simple bounds of the problem are $x_1 \in [0.05, 2.0]$, $x_2 \in [0.25, 1.3]$, and $x_3 \in [2.0, 15.0]$.

$$\begin{aligned}
 g_7(\vec{x}) &= \frac{x_2 x_3}{40} - 1 \leq 0, \\
 g_8(\vec{x}) &= \frac{5x_2}{x_1} - 1 \leq 0, \\
 g_9(\vec{x}) &= \frac{x_1}{12x_2} - 1 \leq 0, \\
 g_{10}(\vec{x}) &= \frac{1.5x_6 + 1.9}{x_4} - 1 \leq 0, \\
 g_{11}(\vec{x}) &= \frac{1.1x_7 + 1.9}{x_5} - 1 \leq 0.
 \end{aligned} \tag{5}$$

The simple bounds of the problem are $x_1 \in [2.6, 3.6]$, $x_2 \in [0.7, 0.8]$, $x_3 \in [17, 28]$, $x_4 \in [7.3, 8.3]$, $x_5 \in [7.8, 8.3]$, $x_6 \in [2.9, 3.0]$, and $x_7 \in [5.0, 5.5]$.

The optimum design of the speed reducer is executed using GDE3 metaheuristic, and the best solution is found as $x^* = \{x_1, x_2, x_3, x_4, x_5, x_6, x_7\} = \{3.50000000047883, 0.7, 17.0, 7.3, 7.8, 3.35021466645262, 5.2866832298256\}$ which yields an objective function value of $f(\vec{x}) = 2996.34816529042$ as seen in Table 8.

The results obtained by GDE3 are presented in Table 8. GDE3 found the global optimum requiring 400 iterations per optimization run. Table 9 provides a comparison of this solution with the results of simple constrained particle swarm optimization. It is apparent from the table that GDE3 metaheuristic finds a competitive solution using only 10,000 objective function evaluations, which is considerably lesser than those of other approaches. Further, a statistical evaluation of 100 independent runs of the GDE3 metaheuristic is tabulated in Table 10 considering the best, worst, average, and the standard deviation (std. dev.) of the obtained solutions.

TABLE 13: Statistical results of the GDE3 optimization.

Best	Average	Worst	Std. dev.	Number of iterations
0.012665836	0.012666648	0.012667194	3.97815E - 07	400

The optimum design of the tension/compression spring is carried out using GDE3 metaheuristic, and the best solution is found as $x^* = \{x_1, x_2, x_3\} = \{0.0517955276224998, 0.359283196922392, 11.1405163630287\}$ which yields an objective function value of $f(\vec{x}) = 0.0126658360085857$ as seen in Table 11.

The results obtained by GDE3 are presented in Table 11. GDE3 found the global optimum requiring 400 iterations per optimization run. Table 12 provides a comparison of this solution with the results of simple constrained particle swarm optimization. It is apparent from the table that GDE3 metaheuristic finds a competitive solution using only 10,000 objective function evaluations, which is considerably lesser than those of other approaches. Further, a statistical evaluation of 100 independent runs of the GDE3 metaheuristic is tabulated in Table 13 considering the best, worst, average, and the standard deviation (std. dev.) of the obtained solutions. The ratio between the optimized costs corresponding to worst and best designs is 1.000107.

4. Conclusion

In the present study, the GDE3 algorithm is used as a simple and efficient optimization technique for handling engineering optimization problems. The GDE3 algorithm also uses a very simple mechanism to deal with constrained functions and results generated by the algorithm indicate that such mechanism, despite its simplicity, is effective in practice. From this study, performance evaluation of the GDE3 algorithm through benchmark design optimization examples reveals the efficiency of this technique in solving practical optimization problems. Although in the present study the algorithm is utilized only for solving engineering design optimization problems, GDE3 algorithm can easily be employed for solving other types of optimization problems as well.

Conflict of Interests

The authors declare that there is no conflict of interests regarding the publication of this paper.

References

- [1] A. H. Gandomi, X.-S. Yang, and A. H. Alavi, "Mixed variable structural optimization using Firefly Algorithm," *Computers & Structures*, vol. 89, no. 23-24, pp. 2325-2336, 2011.
- [2] R. Caballero, M. González, F. M. Guerrero, J. Molina, and C. Parolera, "Solving a multiobjective location routing problem with a metaheuristic based on tabu search. Application to a real case in Andalusia," *European Journal of Operational Research*, vol. 177, no. 3, pp. 1751-1763, 2007.
- [3] A. Kaveh and S. Talatahari, "A novel heuristic optimization method: charged system search," *Acta Mechanica*, vol. 213, no. 3-4, pp. 267-289, 2010.
- [4] O. Adekanmbi, O. Olugbara, and J. Adeyemo, "An investigation of generalized differential evolution metaheuristic for multi-objective optimal crop-mix planning decision," *The Scientific World Journal*, vol. 2014, Article ID 258749, 9 pages, 2014.
- [5] F. Glover and G. A. Kochenberger, *Handbook of Metaheuristics*, Springer, 2003.
- [6] M. M. Atiqullah and S. S. Rao, "Simulated annealing and parallel processing: an implementation for constrained global design optimization," *Engineering Optimization*, vol. 32, no. 5, pp. 659-685, 2000.
- [7] C. A. Coello Coello, "Use of a self-adaptive penalty approach for engineering optimization problems," *Computers in Industry*, vol. 41, no. 2, pp. 113-127, 2000.
- [8] J. Zhang, C. Liang, Y. Huang, J. Wu, and S. Yang, "An effective multiagent evolutionary algorithm integrating a novel roulette inversion operator for engineering optimization," *Applied Mathematics and Computation*, vol. 211, no. 2, pp. 392-416, 2009.
- [9] K. E. Parsopoulos and M. N. Vrahatis, "Unified particle swarm optimization for solving constrained engineering optimization problems," in *Advances in Natural Computation*, vol. 3612 of *Lecture Notes in Computer Science*, pp. 582-591, Springer, Berlin, Germany, 2005.
- [10] K. Deb, "Optimal design of a welded beam via genetic algorithms," *AIAA Journal*, vol. 29, no. 11, pp. 2013-2015, 1991.
- [11] J. P. B. Leite and B. H. V. Topping, "Improved genetic operators for structural engineering optimization," *Advances in Engineering Software*, vol. 29, no. 7-9, pp. 529-562, 1998.
- [12] S. Akhtar, K. Tai, and T. Ray, "A socio-behavioral simulation model for engineering design optimization," *Engineering Optimization*, vol. 34, no. 4, pp. 341-354, 2002.
- [13] T. Ray and K. M. Liew, "Society and civilization: an optimization algorithm based on the simulation of social behavior," *IEEE Transactions on Evolutionary Computation*, vol. 7, no. 4, pp. 386-396, 2003.
- [14] A. C. C. Lemonge and H. J. C. Barbosa, "An adaptive penalty scheme for genetic algorithms in structural optimization," *International Journal for Numerical Methods in Engineering*, vol. 59, no. 5, pp. 703-736, 2004.
- [15] S. He, E. Prempain, and Q. H. Wu, "An improved particle swarm optimizer for mechanical design optimization problems," *Engineering Optimization*, vol. 36, no. 5, pp. 585-605, 2004.
- [16] K. S. Lee and Z. W. Geem, "A new meta-heuristic algorithm for continuous engineering optimization: harmony search theory and practice," *Computer Methods in Applied Mechanics and Engineering*, vol. 194, no. 36-38, pp. 3902-3933, 2005.
- [17] A. R. Hedar and M. Fukushima, "Derivative-free filter simulated annealing method for constrained continuous global optimization," *Journal of Global Optimization*, vol. 35, no. 4, pp. 521-549, 2006.
- [18] S.-F. Hwang and R.-S. He, "A hybrid real-parameter genetic algorithm for function optimization," *Advanced Engineering Informatics*, vol. 20, no. 1, pp. 7-21, 2006.
- [19] H. S. Bernardino, H. J. C. Barbosa, and A. C. C. Lemonge, "A hybrid genetic algorithm for constrained optimization problems in mechanical engineering," in *Proceedings of the IEEE*

- Congress on Evolutionary Computation (CEC '07)*, pp. 646–653, IEEE, 2007.
- [20] M. Mahdavi, M. Fesanghary, and E. Damangir, “An improved harmony search algorithm for solving optimization problems,” *Applied Mathematics and Computation*, vol. 188, no. 2, pp. 1567–1579, 2007.
- [21] L. C. Cagnina, S. C. Esquivel, and C. A. Coello, “Solving engineering optimization problems with the simple constrained particle swarm optimizer,” *Informatica*, vol. 32, no. 3, pp. 319–326, 2008.
- [22] M. Fesanghary, M. Mahdavi, M. Minary-Jolandan, and Y. Alizadeh, “Hybridizing harmony search algorithm with sequential quadratic programming for engineering optimization problems,” *Computer Methods in Applied Mechanics and Engineering*, vol. 197, no. 33–40, pp. 3080–3091, 2008.
- [23] M. Zhang, W. Luo, and X. Wang, “Differential evolution with dynamic stochastic selection for constrained optimization,” *Information Sciences*, vol. 178, no. 15, pp. 3043–3074, 2008.
- [24] O. Hasançebi, S. K. Azad, and O. Hasançebi, “An efficient metaheuristic algorithm for engineering optimization: SOPT,” *International Journal of Optimization in Civil Engineering*, vol. 2, no. 4, pp. 479–487, 2012.
- [25] J. Golinski, “An adaptive optimization system applied to machine synthesis,” *Mechanism and Machine Theory*, vol. 8, no. 4, pp. 419–436, 1973.
- [26] R. Storn and K. Price, “Differential evolution—a simple and efficient heuristic for global optimization over continuous spaces,” *Journal of Global Optimization*, vol. 11, no. 4, pp. 341–359, 1997.
- [27] V. L. Huang, A. K. Qin, and P. N. Suganthan, “Self-adaptive differential evolution algorithm in constrained real-parameter optimization,” in *Proceedings of the IEEE Congress on Evolutionary Computation (CEC '06)*, pp. 215–222, Vancouver, Canada, July 2006.
- [28] K. Suresh, D. Kundu, S. Ghosh, S. Das, and A. Abraham, “Data clustering using multi-objective differential evolution algorithms,” *Fundamenta Informaticae*, vol. 97, no. 4, pp. 381–403, 2009.
- [29] S. Kukkonen and J. Lampinen, “Generalized differential evolution for general non-linear optimization,” in *COMPSTAT 2008*, pp. 459–471, Springer, 2008.
- [30] J. Rönkkönen, S. Kukkonen, and J. Lampinen, “A comparison of differential evolution and generalized generation gap model,” *Journal of Advanced Computational Intelligence and Intelligent Informatics*, vol. 9, no. 5, pp. 549–555, 2005.
- [31] S. Kukkonen and J. Lampinen, “GDE3: the third evolution step of generalized differential evolution,” in *Proceedings of the IEEE Congress on Evolutionary Computation (CEC '05)*, pp. 443–450, September 2005.
- [32] G. G. Dimopoulos, “Mixed-variable engineering optimization based on evolutionary and social metaphors,” *Computer Methods in Applied Mechanics and Engineering*, vol. 196, no. 4, pp. 803–817, 2007.

Research Article

Safety Identifying of Integral Abutment Bridges under Seismic and Thermal Loads

Narges Easazadeh Far and Majid Barghian

Department of Structural Engineering, Faculty of Civil Engineering, University of Tabriz, Tabriz 5166616471, Iran

Correspondence should be addressed to Majid Barghian; barghian@tabrizu.ac.ir

Received 2 August 2014; Revised 6 September 2014; Accepted 6 September 2014; Published 27 October 2014

Academic Editor: Siamak Talatahari

Copyright © 2014 N. Easazadeh Far and M. Barghian. This is an open access article distributed under the Creative Commons Attribution License, which permits unrestricted use, distribution, and reproduction in any medium, provided the original work is properly cited.

Integral abutment bridges (IABs) have many advantages over conventional bridges in terms of strength and maintenance cost. Due to the integrity of these structures uniform thermal and seismic loads are known important ones on the structure performance. Although all bridge design codes consider temperature and earthquake loads separately in their load combinations for conventional bridges, the thermal load is an “always on” load and, during the occurrence of an earthquake, these two important loads act on bridge simultaneously. Evaluating the safety level of IABs under combination of these loads becomes important. In this paper, the safety of IABs—designed by AASHTO LRFD bridge design code—under combination of thermal and seismic loads is studied. To fulfill this aim, first the target reliability indexes under seismic load have been calculated. Then, these analyses for the same bridge under combination of thermal and seismic loads have been repeated and the obtained reliability indexes are compared with target indexes. It is shown that, for an IAB designed by AASHTO LRFD, the indexes have been reduced under combined effects. So, the target level of safety during its design life is not provided and the code’s load combination should be changed.

1. Introduction

Integral abutment bridges (IABs) are continuous single or multispans bridges in which the jointless superstructure is connected rigidly to the abutment. So, in the longitudinal direction these two parts can be assumed as a single integral component. The rigid connection between them leads most of displacements and loads transfer from superstructure to substructure consisting of abutments and piled foundations. By eliminating the expansion joints in IABs, most problems associated with expansion joints and bearings are reduced, such as high maintenance costs, deterioration due to deicing chemicals, and impact loads. These advantages of IABs have caused them to be used throughout the world increasingly, especially, in USA, Canada, UK, and Republic of Korea. These bridges similar to conventional bridges are subjected to primary (loads live loads, dead loads, seismic loads, etc.) and secondary effects (shrinkage, creep, passive pressure, uniform temperature changes, thermal gradients, etc.). Among these loads—due to the integrity of these bridges and the resultant complexity of soil/structure interactions—uniform thermal

and longitudinal seismic loads become important and have deterministic role in the behavior of IABs.

Several researchers studied the behavior of these bridges under thermal and seismic loads separately and showed the importance of these loads on the IAB’s response. Tsang and England [1] investigated the soil/structure interaction of integral bridge with full height abutments. Dicleli and Albhaisi [2] studied the effect of cyclic thermal loading on the behavior of steel H-piles foundation of integral bridges. In this research the abutments of bridges are stub. Kim and Laman [3] investigated the integral abutment bridge response under the thermal loading. In the other research they studied the long-term behavior of integral abutment bridges by using numerical analysis. Tegos et al. [4] proposed two different abutment configurations to improve seismic behavior of integral bridges. Itani and Pekcan [5] and Frosch et al. [6] investigated the seismic behavior of IABs and developed design recommendations. Maleki and Mahjoubi [7] introduced a 2D finite element model for seismic analysis of retaining walls and integral bridge abutments. They also proposed a new seismic soil pressure distribution to replace

the Mononobe-Okabe [8] equations. Kim [9] proposed new load combinations for the load and resistance factor design (LRFD) to design typical IABs, by developing the nominal IAB response prediction models and establishing IAB's response statistics using Monte Carlo simulation. These developed load combinations were established using reliability analysis and included dead load, live load, and thermal load due to temperature variation, temperature gradient, backfill pressure, and time-dependent effects.

As (1) Eurocode 8 [10], American Association of State Highway and Transportation Officials (AASHTO LRFD 2012) [11] and other developed bridge design codes consider temperature and earthquake loads separately in their specified load combinations for the design of bridges; (2) by knowing that these load combinations have been primarily defined for conventional bridges with expansion joints while due to the elimination of expansion joints and due to the integration between substructure and superstructure of IABs overall performance of bridges is different from conventional bridges; (3) according to the fact that there is a temperature difference between temperature at any time of bridge life and bridge construction time temperature, hence, a uniform temperature load is applied to the bridge. Therefore, during earthquake the existence of a uniform temperature load is an obvious matter; and (4) both the uniform temperature load and earthquake load are important for integral bridges due to their structural nature and the role of the mentioned loads on these bridges. Therefore, the importance of evaluating the safety level IABs—designed by AASHTO LRFD [11] bridge designed code—under combination of temperature and earthquake loads during the design life of IABs is perceived.

For this reason, in this paper, by using structural reliability analysis conducted on a case study bridge—designed in accordance with existing AASHTO LRFD [11] code—the safety level of bridge under combination of seismic and thermal loads was evaluated during its 75-year design life [11]. Comparing the obtained results with the target safety level, it will be clear whether the target safety level for designed integral bridge—during design life (according to AASHTO LRFD)—under combined effect of seismic and thermal loads is guaranteed or not. On the other hand, the current code has been written for conventional bridges but it is used for IABs. Codes are gradually developed to consider new bridges such as IABs. If the target safety level for these bridges is not satisfied then the modification of the code's load combination is needed.

To achieve this objective, this paper reviews the basic reliability concepts and available analytical models for studying the reliability of structures under the combination of loads. These models are (1) Turkstra's rule [19]; (2) the Ferry-Borges (or Ferry Borges-Castanheta) model [20]; (3) Wen's load coincidence method [21]; and (4) scenario sampling model [22, 23].

As the reliability index is usually used to evaluate the safety level of a structure, an IAB designed based on AASHTO LRFD bridge design specification [11] was analyzed to evaluate reliability index values for its 75-year design life (a 75-year design life is used for an IAB [11]) for different limit states. As moments and shears at the interface of pile with

the abutment are most affected by the temperature change that accompanies an earthquake, the bending moment and shearing limit states of piled foundation are considered in this paper. First, the reliability indexes are calculated for bridges under the effect of only earthquake load to evaluate the target reliability indexes [24]. Then by repeating these analyses for the same bridges subjected to the combination of seismic and thermal loads and comparing evaluated indexes with the target reliability indexes, whether the target safety level for designed integral bridge—according to AASHTO LRFD code under uniform temperature and earthquake loads combination—is satisfied or not will be investigated.

As mentioned above, AASHTO LRFD [11] considers earthquake load separately in the extreme event I load combination as addressed in

$$\text{Extreme Event } I = \gamma_{DL}DL + \gamma_{P_a}P_a + \gamma_{\Delta P_a}\Delta P_{ae} + \gamma_{EQ}EQ, \quad (1)$$

where EQ, DL, P_a , and ΔP_{ae} are seismic load, dead load, static earth pressure, and seismic earth pressure, respectively, and $\gamma_{DL} = 1.25$, $\gamma_{P_a} = 1.5$, $\gamma_{\Delta P_a} = 1$, $\gamma_{EQ} = 1$ are the considered load factors.

The statistical data required for this reliability analysis are assembled from reliability literature, Ghosn et al. [24], United States Geological survey (USGS) website [16], weather website [18, 25], and Kim [9].

2. Basic Concepts of Structural Reliability Theory

The purpose of the structural reliability theory is, including the uncertainties associated with the member capacity and the occurrence, intensities and effect of loads that the members are subjected to during their design life. Thus, all variables contributing in the member resistance and the load effects should be represented by random variables. The minimum characteristics to define a random variable, R , are probability distribution function, PDF, the Mean value, \bar{R} , and the standard deviation, σ_R . As shown in (2), the coefficient of variation (COV) is defined as the ratio of standard deviation, σ_R , to mean value, \bar{R} , and bias factor, b_r , as the ratio of the mean value, \bar{R} , to the nominal or design value, R_n . Consider

$$\text{COV} = \frac{\sigma_R}{\bar{R}}, \quad b_r = \frac{\bar{R}}{R_n}. \quad (2)$$

Based on structural reliability theory, the safety of a structure can be achieved just when the structural resistance (R) exceeds the load effects (S). So, the reliability, R_e , of a structure is the probability of this exceedance as follows:

$$R_e = \Pr [R > S],$$

$$R_e = \Pr [Z = R - S > 0], \quad (3)$$

$$\text{or } R_e = \Pr [Z(X_1, X_2, \dots, X_n) > 0],$$

where Z is the limit state function that relates the resistance (R) to the load effects (S) for evaluating the safety level

of the structure. X_1, X_2, \dots, X_n are the random variables associated with the resistance and the applied loads. In contrast, probability of failure, P_f , is the probability that the safety margin, Z , is less than zero as follows:

$$P_f = \Pr [R < S] = \Pr [Z < 0] = 1 - R_e. \quad (4)$$

The reliability index, β , is usually used to evaluate the safety level of a structure. This index is related to the probability of failure as follows:

$$\beta = -\Phi^{-1}(P_f), \quad (5)$$

where Φ is the cumulative standard normal distribution function. A general equation for the probability of failure is defined as follows:

$$P_f = \int_{Z(\{\mathbf{X}\}) < 0} f_{\{\mathbf{X}\}}(\{\mathbf{x}\}) dx_1 dx_2 \dots dx_n, \quad (6)$$

where $\{\mathbf{X}\} = \{X_1, X_2, \dots, X_n\}$ is a random variables vector, $f_{\{\mathbf{X}\}}(\{\mathbf{x}\})$ is the probability density of vector $\{\mathbf{X}\}$, and $Z(\{\mathbf{X}\})$ is the limit state function. As $f_{\mathbf{x}_i}$ is generally unknown, the evaluation of the probability of failure, P_f , using (6) is very difficult. Therefore, based on the type of distribution function corresponding to the structural resistance (R) and load effects (S) in the limit state function (Z) in (3), there are several methods to evaluate the reliability index. The methods include the first order reliability method (FORM), the second order reliability method (SORM), and Monte Carlo simulation method. In this paper, the Monte Carlo simulation method was used to evaluate the probability of failure. Then by using (5), the reliability index was obtained. The Monte Carlo method creates large number simulated outcomes of a limit state. Next, by counting the number of failure events ($Z < 0$) and dividing them into the total number of simulated events, the probability of failure, P_f , can be estimated. In this method, during each simulation, all involved variables in the limit state function are chosen (or generated) randomly [26].

The reliability index has been used to express structural risk. For this index the range of 2 to 4 is usually specified to failure of a single component for different structural application [24].

To calculate the reliability index, at first, the statistical data for all the random variables associated with the limit state function Z of (3) should be obtained. These data include all the uncertainties in estimating the member resistances and the load effects. According to Nowak [13] and Ellingwood et al. [15] approach a bridge member resistance capacity by a variable R can be defined as follows:

$$R = MFPR_n, \quad (7)$$

where M is material factor representing properties such as strength and modulus of elasticity; F is fabrication factor including geometry, dimensions, and section modulus; P is analysis factor such as approximate models for estimating member capacity, idealized stress, and strain distribution models; and R_n is predicted member capacity using code-specified methods. Equation (7) can be used to find the mean

value of R using (2) if the total resistance bias, b_r , is set to be equal to the product of the mean values of M , F , and P . The resistance model of (7) does not directly account for member deterioration or other changes with time. Thus, all the variables are time-independent random variables.

For a bridge member (or structural system) to be safe, the resistance should be large enough for the maximum load effect that could occur within the structure's service life. Estimating the effects of the maximum loads involves a number of random variables, which may often be associated with large levels of modeling uncertainties. In particular, the intensities of the maximum loads are time-dependent random variables in the sense that longer service lives imply higher chances that the structure will be subjected to a given extreme load level. On the other hand, the projection of limited load intensity data, collected from previous measurements over short periods of time, to future return periods is associated with various levels of statistical modeling uncertainties. In addition, modeling the structure's response to the applied loads and estimating the variables that control the effects of the loads on the structure are associated with high levels of uncertainty that are independent of the return period. These modeling uncertainties are often represented by time-independent random variables. Thus, the effect of a particular load type, i , on a structural member may be represented as follows:

$$S_i = \lambda_i f_i(\lambda_{Q_i} C_{ij} Q_i), \quad (8)$$

where S_i is the load effect for load type i ; λ_i is the analysis modeling factor that accounts for differences between measured load effects and predicted load effects; $f_i()$ is the analysis prediction model that converts load intensities into load effects; Q_i is the projected intensity variable of load type i for the return period of interest; λ_{Q_i} is the statistical modeling variable that accounts for the limitations in predicting the value of Q_i ; and C_{ji} is the analysis variables such as bridge material and geometrical properties required for executing the analysis for load type i . All the variables in (8) may be considered random where Q_i is a time-dependent random variable and the remaining variables are time-invariant. The probability density of the load intensity, Q_i , for a given return period, t , can be calculated by studying the probability that Q_i will exceed a given value within t . Assuming that the occurrence of load events follows a Poisson model, the probability that the load intensity will exceed a value x , within a period, t , is represented by $(1 - F_{Q_i,t}(x))$, which may be approximated as

$$\Pr(Q_i > x; T < t) = 1 - F_{Q_i,t}(x) = 1 - e^{(-tp)}, \quad (9)$$

where p is the rate of exceedance per unite time. P is equal to the probability of exceeding x when t equals 1.0:

$$p = \Pr(Q_i > x) = 1 - F_{Q_i}(x). \quad (10)$$

For extreme values of x , when the values of $F_{Q_i}(x)$ are close to 1.0 and p is calculated for one unit of time while the return

period, t , consists of m units of time, (9) can be approximated as

$$\begin{aligned} \Pr(Q_i > x; T < t) &= 1 - F_{Q_{i,t}}(x) \\ &= 1 - e^{(-tp)} \approx 1 - (1 - p)^m \quad (11) \\ &= 1 - (F_{Q_i}(x))^m. \end{aligned}$$

Equation (10) can be written as follows:

$$\Pr(Q_i < x; T < t) = F_{Q_{i,t}}(x) \approx (F_{Q_i}(x))^m. \quad (12)$$

Equation (12) indicates that the cumulative probability function for a return period of time, t , may be approximated by raising the cumulative probability function of the basic time period to the power, m .

3. Reliability Methods for Combination of Loads

In general, by considering the variability of the load magnitude with time, the loads can be classified as permanent loads that are time independent and transient loads that vary with time. The minimum required characteristics to represent a time-dependent load are the rate of occurrence in time, the time duration, and the intensity of load. This kind of load can be modeled by a random process. As described before, in order to evaluate the probability of failure of the structure under the combination of load effects, the extreme value of the combined load effects is required. For this purpose, the extreme value of the combined load effects corresponding to considered limit state should be calculated. During the design life time of a structure (T), different individually acting time-dependent loads may be modeled as the sum of the load effect processes $X_i(t)$ and the extreme value $X_{\max}(T)$ is calculated as follows:

$$X_{\max}(T) = \max_T \{X_1(t) + X_2(t) + \dots + X_n(t)\}. \quad (13)$$

As generally it is very difficult to obtain an exact solution of (13), some approximate analytical models exist to estimate this solution. These are (1) Turkstra's rule [19]; (2) the Ferry-Borges (or Ferry Borges-Castanheta) model [20]; (3) Wen's load coincidence method [21]; and (4) scenario sampling model [22, 23]. As in this paper the scenario sampling model is used, this model is described briefly below.

3.1. Scenario Sampling Method. Scenario Sampling [22, 23] method can be used for time-dependent loads combination. Compared with other methods, this method has high accuracy and can be used for any linear and nonlinear loads combinations. This method is presented based on Monte Carlo sampling.

To calculate the probability of structural failure under the combination of several time-dependent loads for a limit state function using scenario sampling method it is done as follows: with the knowledge of the rate of occurrence, time duration, and intensity of each time-dependent load and by using Poisson's distribution function to estimate the

occurrence time of any event of load, first, during structure's T -years design life, a scenario of load occurrence is generated. Then, whenever the intensity of any load changes, the amount of limit state function is calculated. Among the limit state function amount for each T -year life, the minimum limit state function amount is selected which is related to the maximum loads effect in the structure life. This procedure is repeated n times. According to Monte Carlo's method, the failure probability is calculated by dividing the total states—in which their limit state function minimum amount is negative (indicating member failure)—into the total simulating cycles, n , and finally the reliability index is calculated from (5). The total of simulating cycles, n , is chosen in a way that coefficient of variation related to failure probability is maximum 2%.

4. IAB Pile Resistance Capacity

As described before, the considered limit state in this study is the bending moment and shearing failure of the IAB pile. For supporting the abutments of the considered IAB a single row of steel H-piles is used. As the bending moment and shearing capacities of steel pile are defined by its yield stress, F_y , and geometric parameters, by considering the yield stress of pile section as a random variable the uncertainties associated with the bending moment and shearing capacities of the pile are taken into account during reliability analysis. So, for the yield stress, F_y , a bias of 1.05 and a COV of 10% using a lognormal distribution are used [27].

5. Reliability Models for Loads

According to extreme event I load combination of AASHTO LRFD [11], nominal design loads dead load, earth pressure, seismic load, and uniform thermal load are just considered in this study. The required statistical models of these loads are described in this section.

5.1. Dead Load. Based on Nowak [13], the statistics for dead load are summarized in Table 1.

Since, in this study, the deck of considered IAB is a factory-made steel girder composite and cast-in place concrete slab, a bias of $1.08 = 1.03 \times 1.05$ with a COV of $12.8\% = \sqrt{10^2 + 8^2}$ using a normal distribution is used for dead load.

5.2. Backfill Earth Pressure. Backfill static earth pressure dependent on the movement direction of IAB's abutments under applied loads can be the form of passive or active. The backfill passive pressure (abutment moves far from backfill) resists bridge against applied load while active pressure (abutment moves toward backfill) is a permanent load on the abutments. Based on Rankin's theory, the lateral earth pressure considering cohesionless backfill soil is determined by unit weight and friction angle of soil. Based on Becker's researches [14], statistics for backfill soil are summarized in Table 2.

5.3. Earthquake Load. The reliability analysis of a structural member under earthquake load involves a number of random variables that the uncertainty of them should be considered.

TABLE 1: Dead load Statistics [13].

Load	Bias factor (b_r)	Coefficient of variation (COV %)
Dead load (factory-made component)	1.03	8
Dead load (cast-in place component)	1.05	10
Asphalt wearing surface (88.9 mm assumed)	1	25

TABLE 2: Backfill Soil related statistics [14].

Variable	Bias	COV	Distribution type
Unit weight (γ)	1.0	7%	Normal
Fraction angle (ϕ_s)	1.0	13%	Normal
Rankine coefficient (K_p, K_a)	1.5	20%	Normal
Cyclic effects, λ_{cyc}	1.0	15%	Normal

A brief discussion of each variable is given and statistics for each are summarized in Table 3.

5.3.1. Intensity of Earthquake Acceleration. The expected earthquake intensity for IAB's sites was obtained from the USGS [16]. These maps provide the horizontal peak ground accelerations (PGAs) for various sites throughout the United States with 7 percent exceedance probability in 75 years (a return period of about 1000 yr). In this study five sites were considered as the IAB's site: San Francisco with 94117 zip code, Seattle with 98195 zip code, Memphis with 38101 zip code, New York with 10031 zip code, and St. Paul with 55418 zip code. An annual exceedance probability curves for PGA was provided by Frankel et al. [12] for a number of sites (see Figure 1).

5.3.2. Rate of Earthquake Occurrence. The number of expected earthquakes varies from site to site and is available at the USGS [16]. The average number of earthquakes in one year is about 8 for San Francisco, 2 for Seattle, 0.5 for Memphis (one every 2 years), 0.4 for New York (one every 2.5 years), and 9×10^{-3} for St. Paul (one every 111 years).

5.3.3. Natural Period of IABs. The natural period of an IAB is related to the type of bridge structure, type of bridge foundation, the characteristics of the used materials, the characteristics of bridge geometry, the interaction between soil and structure (SSI), and so forth. As the considered IAB in this study included the effects of SSI, based on published researches [17], a bias of 0.9 and a COV of 20% using a normal distribution was used for the natural period of the IAB.

5.3.4. Mass Applied. To account for uncertainties associated with the mass applied on the IAB's members (considering weight alone) a bias of 1.05 and a COV of 5% using a normal distribution were used [13, 15].

5.3.5. Seismic Response Coefficient. The design response spectrum proposed by AASHTO LRFD [11] was used in this paper. These design spectra are based on the USGS [16]. For considering uncertainties associated with these spectra, the statistics provided by Frankel et al. [12] were used. They found that, for all sites inside USA, the mean value of spectral accelerations is very close to the design spectral accelerations, so a bias of 1.0 can be used. Also, for all sites, COV depends on the number of observed earthquakes at which, the COV is low for sites with high frequency of earthquakes and for sites with low frequency the COV is high. Therefore, for San Francisco, the COV is about 15%, for Seattle and Memphis it is about 25%, for New York it is about 30%, and for St. Paul it is about 40%. For this variable a normal distribution is used.

5.3.6. Modeling Factor. Modeling factor was used to take into account for the uncertainties produced during the dynamic analysis process. A bias of 1 and a COV of 20% using a normal distribution were used for this variable [15].

5.3.7. Reliability Equation for Earthquake Load. Using the presented information, the equivalent seismic load applied on the IAB is defined as follows:

$$F_{EQ} = \lambda_{eq} C' S_a (t' T) \times \frac{A \times W}{R_m}, \quad (14)$$

where F_{EQ} is the equivalent applied load, λ_{eq} is the modeling factor, C' is the response spectrum modeling parameter, A is the maximum 75-year peak ground acceleration at the site, S_a is the calculated spectral acceleration using the IAB's period, T , and period modeling factor, t' , W is the weight of system, and R_m is the response modification factor which is equal to 1.0 for IAB's pile [11]. The statistics for random variables used in (14) are summarized in Table 3.

5.4. Uniform Thermal Load. Due to eliminating expansion joints in IAB's superstructure and due to the rigid connection of IAB's superstructure to substructure (consisting of abutments, pile, and backfill soil), the movements of IAB's superstructure due to temperature variation are transferred to substructure and induce thermal load on substructure. This uniform thermal load depends on the superstructure's temperature variation, thermal expansion coefficient and bridge span length.

To consider the uncertainties associated with this load, super structure temperature and thermal expansion are considered as random variables as follows.

5.4.1. Superstructure Temperature. The superstructure temperature is affected by the ambient air temperature, solar radiation, wind speed and direction, and so forth. The primary component of them is the ambient air temperature and can be assumed as the IAB's superstructure temperature [28]. Thus, based on Kim's research [9], for every 7 days, the IAB's superstructure temperature is a normal distribution with a mean value defined by (15) and standard deviation which have been tabulated in Table 4:

$$T_{mean}(t) = \mu_T + A_T \sin(\omega t + \phi_T), \quad (15)$$

TABLE 3: Earthquake load related statistics.

Variable	Bias	COV	Distribution type	Reference	
Earthquake modeling factor, λ_{eq}	1.0	20%	Normal	[15]	
Spectrum modeling factor, C'	San Francisco		15%	Normal [12]	
	Seattle		25%		
	Memphis	1.0	25%		
	New York		30%		
	St. Paul		40%		
75-year PGA, A	San Francisco			[16]	
	Seattle				
	Memphis	from Figure 1	from Figure 1		from Figure 1
	New York				
	St. Paul				
Period modeling factor, t'	0.9	20%	Normal	[17]	
Weight, W	1.05	5%	Normal	[15]	

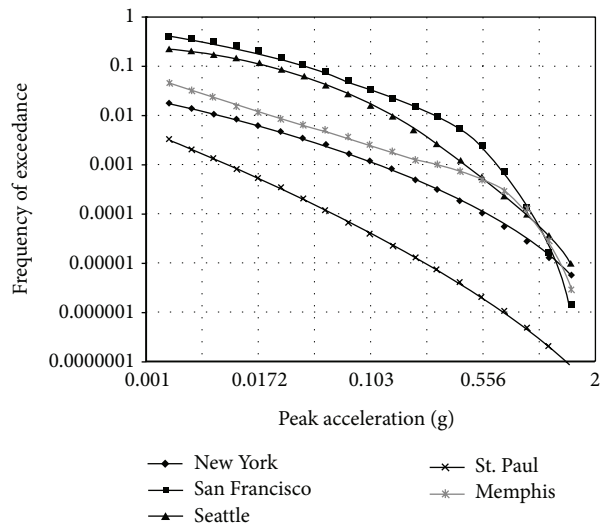


FIGURE 1: Annual probability of exceedance curves for PGA [12].

where μ_T is annual mean temperature, A_T is annual mean temperature variation, ω is frequency (2π), t is analyzing time (year), and ϕ_T is phase lag. For three sites considered in this study the temperature statistics were established from the weather website [18] and summarized in Table 4.

5.4.2. *Thermal Expansion Coefficient.* In this study, based on AASHTO LRFD [11] a nominal design value of $1.17 \times 10^{-6}/^\circ C$ is considered for the thermal expansion coefficient of the IAB's deck steel girders. A bias of 1.0 and a COV of 0.1 using a normal distribution are used for this random variable [27].

6. Reliability Analysis of the Integral Abutment Bridge

In this section, the reliability analysis is performed for a basic IAB designed to satisfy the current AASHTO LRFD specifications for evaluating the safety level under seismic and thermal

loads for its 75-year design life (a 75-year design life is used for an IAB [11]) for different limit states. As Piles moments and shears are most affected by the temperature change that accompanies an earthquake, the bending moment and shearing limit states of piled foundation are considered in this paper. For evaluating the safety level of a structure, first the reliability indexes are calculated for bridges under the effect of only earthquake load to evaluate the target reliability indexes [24]. Then these analyses are repeated for the same bridges subjected to the combination of seismic and thermal loads. Finally, resultant indexes will be compared with the target reliability indexes and the satisfaction of the target safety level for designed integral bridge according to AASHTO LRFD specifications under the temperature and earthquake load combination will be investigated.

In this paper, the reliability indexes have been calculated by using Monte Carlo method. To combine the seismic and thermal loads, the scenario sampling method [22], and reliability analysis, the Rt Software has been used [23].

TABLE 4: Thermal load related statistics [18].

Variable	San Francisco	Seattle	Memphis	New York	St. Paul
Annual mean, μ_T °C	23.89	15.68	16.01	12.78	5.83
Annual variation, A_T °C	3.33	7	12.5	6.5	4.2
Daily standard deviation (°C)	6.59	5.68	6	5.75	6.5

Geometric and structural properties of the basic IAB are described below.

6.1. *Geometric and Structural Properties of the Basic IAB.* The considered IAB in this study is a one-span 40 m IAB having the longitudinal section as shown in Figure 2. The superstructure of the bridge is composed of concrete slab with 20 cm thickness and steel beams at 2 m spacing. Each abutment of this bridge has 7 m height and 1 m wall thickness and supported on a single row of steel H piles with 12 m length at 1 m spacing. The section properties of deck girder and piles are given in Table 5.

The abutments backfill soil is assumed to be dense cohesionless soil with 30° angle of internal friction and a unit weight of 16.72 kN/m³.

As described earlier, the piles moment and shear force are affected the most by the earthquake and thermal loads, thus, in this study bending moment and shearing failure limit state of the IAB piles at point A (where the pile connect to abutment) were considered for reliability analysis. The requirement moment and shear capacity were calculated to satisfy the current AASHTO LRFD specifications. The free body diagram of the basic IAB pile under applied load is shown in Figure 3, where $F_{DL} = 198.16$ kN is the permanent weight of superstructure, $M_{DL} = 1.32$ MN is the moment caused by the permanent weight of superstructure, $P_a = 272.82$ kN is the static active backfill force and acts on the H/3 from the bottom of abutment, ΔP_{ae} is the seismic active backfill force based on Mononobe and Matsue [29] and Okabe [30], and for San Francisco, Seattle, and Memphis it is equal to 819.33 kN, for New York it is equal to 166.28 kN, and for St. Paul it is equal to 17.27 kN. This load acts on the 0.6H from the bottom of abutment [31], $H = 7$ m is the abutment height, $e_1 = 0.25$ m is the dead load eccentricity from the point A, and F_{EQ} is the equivalent earthquake force—described below—transferred from the IAB deck and acts on the distance $f = 6$ m from the bottom of abutment.

The equivalent internal earthquake force, F_{EQ} , by using the nominal natural period of $T = 0.41$ s, the soil of type D, and the calculated spectra acceleration for 1000-year return period (7% probability of exceedance in 75 years) [11], is obtained as follows:

$$F_{EQ} = \frac{S_a \times W}{R_m}, \tag{16}$$

where S_a is the spectral acceleration, W is the weight of structure, and R_m is the response modification factor. Based on AASHTO LRFD [11] by using a modification factor $R_m = 1$

the equivalent earthquake is equal to 307.54 kN for San Francisco site, 210.52 kN for Seattle, 176.38 kN for Memphis, 44.05 kN for New York, and 10.51 kN for St. Paul.

As the dominant AASHTO LRFD [11] load combination to design the considered pile is the extreme event I combination at point A (see Figure 3), the design equation used for calculating the nominal moment capacity is as follows:

$$\phi M_{req} = 1.25M_{DL} + 1.5M_{P_a} + M_{\Delta P_{ae}} + M_{EQ}, \tag{17}$$

where ϕ is the resistance factor which for bending is equal to 0.9, $M_{DL} = 1.37$ MN m ($= 0.198 \times 0.25 + 1.32$) is the total moment caused by permanent weight of superstructure, $M_{P_a} = 0.64$ MN m ($= 0.273$ MN $\times 2.333$ m) is the moment caused by static active backfill force, and $M_{\Delta P_{ae}}$ is the moment caused by seismic active backfill force and is equal to 3.44 MN m ($= 0.819$ MN $\times 0.6 \times 7$ m) for San Francisco, Seattle, and Memphis, equal to 0.698 MN m for New York, and equal to 0.0725 MN m for St. Paul. M_{EQ} is the equivalent earthquake moment that is equal to 1.85 MN m for San Francisco, 1.26 MN m for Seattle, 1.058 MN m for Memphis, 0.264 MN m for New York, and 0.063 MN m for St. Paul.

Based on the extreme event I combination at point A (see Figure 3), the design equation used for calculating the nominal shear capacity is as follows:

$$\phi V_{req} = 1.25V_{DL} + 1.5V_{P_a} + V_{\Delta P_{ae}} + V_{EQ}, \tag{18}$$

where ϕ is the resistance factor which for shearing is equal to 0.9, V_{DL} is the total shear caused by permanent weight of superstructure and usual 0, $V_{P_a} = 0.272$ MN is the shear caused by static active backfill force, and $V_{\Delta P_{ae}}$ is the shear caused by seismic active backfill force and is equal to 0.819 MN for San Francisco, Seattle, and Memphis, equal to 0.166 MN for New York, and equal to 0.0172 MN for St. Paul. V_{EQ} is the equivalent earthquake shear that is equal to 0.308 MN for San Francisco, 0.211 MN for Seattle, 0.176 MN for Memphis, 0.044 MN for New York, and 0.0105 MN for St. Paul.

Using (17) the requirement moment capacity, M_{req} , is equal to 8.84 MN m for San Francisco, 8.18 MN m for Seattle, 7.96 MN m for Memphis, 4.024 MN m for New York, and 3.12 MN m for St. Paul. Using (18) the requirement shear capacity, V_{req} , is equal to 1.706 MN for San Francisco, 1.6 MN for Seattle, 1.56 MN m for Memphis, 0.69 MN for New York, and 0.49 MN for St. Paul.

6.2. *Reliability Analysis under Seismic Load.* The reliability analysis of the IAB pile is performed using the models described in Section 4 and the free body diagram shown in

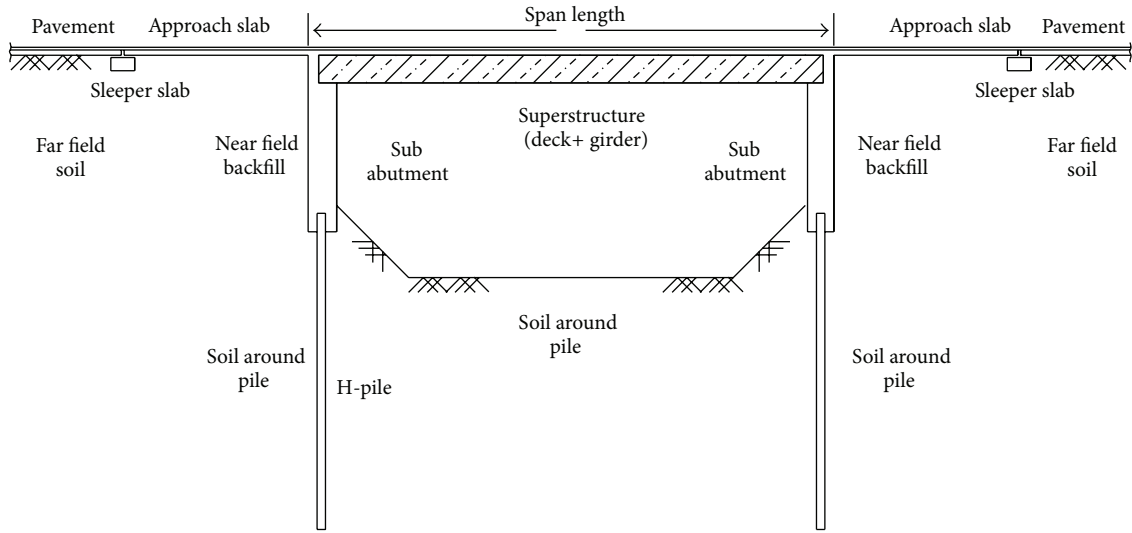


FIGURE 2: Longitudinal section of the IAB.

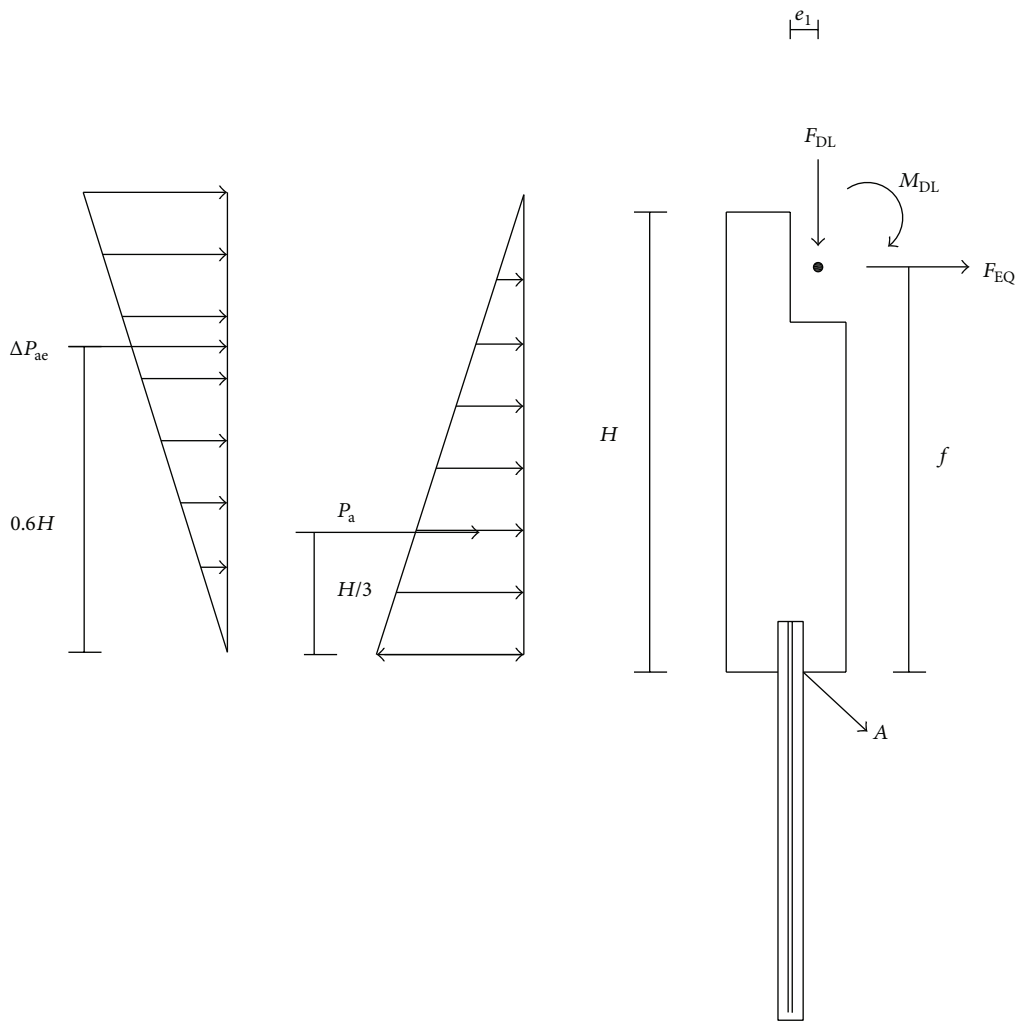


FIGURE 3: Free body diagram of IAB pile, dominant failure is bending at point A.

TABLE 5: Steel sections properties.

Section	Size	Height (cm)	Flange width (cm)	Flange thickness (cm)	Web thickness (cm)
Girder	W 1000 × 975	111	43	9	5
Piles					
San Francisco	H 300 × 300 × 15 × 15	30	30	1.5	1.5
Seattle	H 300 × 300 × 12 × 12	30	30	1.2	1.2
Memphis	H 250 × 250 × 9 × 14	25	25	1.4	0.9
New York	H 200 × 200 × 12 × 12	20	20	1.2	1.2
St. Paul	H 200 × 200 × 8 × 12	20	20	1.2	0.8

Figure 3. Referring to Figure 3 the failure function for pile bending can be represented by following equation:

$$Z_M = M_{Pile} - \left(M_{DL} + \left(\Delta P_{ae} \times 0.6H + P_a \times \left(\frac{H}{3} \right) \right) \right) \times \lambda_{cyc} + F_{EQ} \times f, \tag{19}$$

where M_{Pile} is the pile bending moment capacity, M_{DL} is the total moment caused by superstructure weight, F_{EQ} is the equivalent earthquake load transferred from superstructure defined by (14), P_a is the static active backfill force and acts on the $H/3$ from the bottom of abutment, ΔP_{ae} is the seismic active backfill force [29, 30] and acts on the $0.6H$ from the bottom of abutment [31], $H = 7\text{ m}$ is the abutment height, $f = 6\text{ m}$ is the distance earthquake load from point A, and λ_{cyc} is the model of the effect of cyclic loading on the pile.

Based on Figure 3, the failure equation for pile shearing can be represented as follows:

$$Z_V = V_{Pile} - \left((\Delta P_{ae} + P_a) \times \lambda_{cyc} + F_{EQ} \right), \tag{20}$$

where V_{Pile} is the pile shearing capacity.

Referring to (19)-(20), failure occurs when Z_M or Z_V are less than zero. All variables in (19)-(20) are considered random expect for abutment height, H , and distance earthquake load from point A, f . The statistical models used to describe the random variables are provided in Tables 1, 2, 3, and 4. In these failures limit state only earthquake load composed of time-depended and time-in depended random variables. The reliability analysis of the IAB pile was performed for five sites by using Monte Carlo simulation method using the Rt software [23]. Figures 4 and 5 show the reliability for the bending and shearing failure limit states for each of five sites as a function of pile moment and shear capacity, respectively. The abscissa of the plot is normalized such that a ratio of 1.0 indicates that the bridge is designed to exactly satisfy the AASHT LRFD [11] specifications requirements and reliability index corresponding to this ratio is used as the target reliability index, β_T . Figure 4 shows that the AASHTO LRFD [11] specifications using a nominal response modification factor $R_m = 1$ for pile bending limit state will produce a reliability index, β , between 2.12 and 2.57. The average from the five sites is equal to 2.28. Figure 5 shows that for pile shearing limit state the average reliability index for five sites is 2.33 with a minimum index equaling 2.09 and a maximum value equaling 2.68.

6.3. Reliability Analysis for Combination of Earthquake and Uniform Thermal Loads. As it was written earlier, there is a temperature difference between temperature at any time of bridge life and bridge construction time temperature; hence, a uniform temperature load is applied to the bridge. Therefore, during earthquake the existence of a uniform temperature load is an obvious matter. Due to integrity structure of integral bridges, thermal and earthquake loads are important for these bridges and have determinant role in the performance of integral bridges.

Since most bridge design codes such as AASHTO LRFD have considered these two loads in combination, separately, in this study, designed integral bridge safety level evaluation according to AASHTO LRFD under thermal and earthquake loads combination was investigated. Also comparing the results with target safety level (which was the bridge safety level under seismic load alone) was studied. The research was done to understand whether the safety of these kinds of bridges (during structure life) under the combination of thermal and earthquake loads was satisfied or not?

6.3.1. Combination of Earthquake and Thermal Loads (EQ + TU). The IAB pile was analyzed to illustrate the combined effects of earthquake and thermal loads on the pile. The data from five earthquake sites described in Figure 1 were used. The uniform thermal load data were obtained from models developed by Kim [9] and weather website [18]. The reliability calculations of the IAB pile under considered combined loads follow the scenario sampling method described in Section 3.1. For this method the following assumptions are made.

- (i) The reliability calculations are performed for the bending moment and shearing failure limit states of IAB pile.
- (ii) All earthquakes last 30 sec [24] and during this time it is assumed that the moment and shear at point A of the IAB pile remain at their highest value.
- (iii) All thermal loads last 7 days [9] and during this time the intensity of thermal load remains constant.
- (iv) The reliability analysis accounts for uncertainties which is associated with predicting the earthquake intensity, estimating the bridge pile response for given earthquake intensity, projecting the thermal load magnitude, and estimating pile moment and shear capacity.

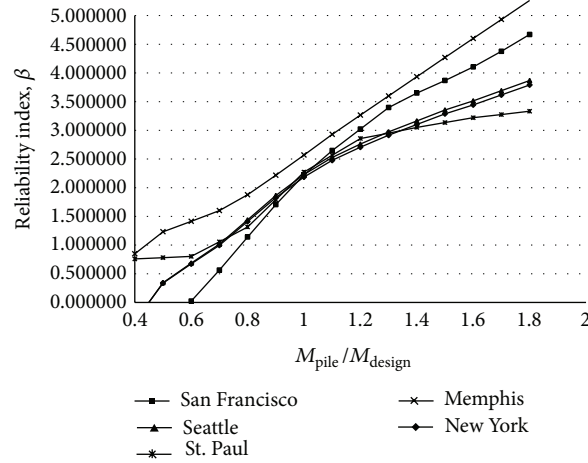


FIGURE 4: Reliability index for the bending of considered IAB's pile under earthquake load alone.

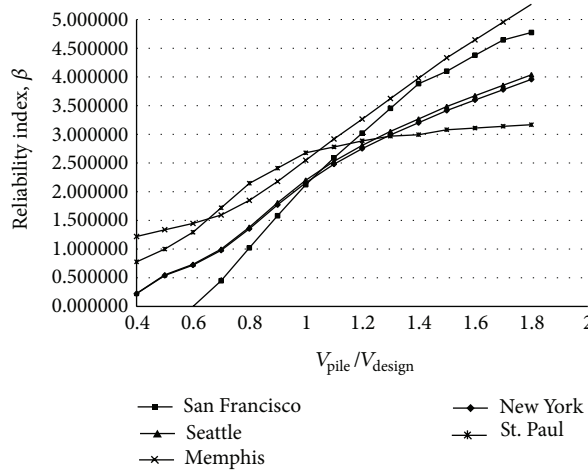


FIGURE 5: Reliability index for the shearing of considered IAB's pile under earthquake load alone.

Referring to Figure 3, the failure function of pile bending under combined load effects can be represented as follows:

$$Z_M = M_{pile} - \left(M_{DL} + \left(\Delta P_{ae} \times 0.6H + P_a \times \left(\frac{H}{3} \right) \right) \right) \times \lambda_{cyc} + F_{EQ+TU,75} \times f \tag{21}$$

where $M_{EQ+TU,75} = F_{EQ+TU,75} \times f$ is the applied moment caused by the combined effects of the earthquake and uniform thermal loads in the period of $T = 75$ years.

Based on Figure 3, the failure equation for pile shearing can be represented as follows:

$$Z_V = V_{Pile} - \left((\Delta P_{ae} + P_a) \times \lambda_{cyc} + F_{EQ+TU,75} \right), \tag{22}$$

where $F_{EQ+TU,75}$ is the applied shear caused by the combined effects of the earthquake and uniform thermal loads. This

combined effect is calculated by using scenario sampling [22, 23] method as described in Section 3.1.

The reliability analysis of the IAB pile was performed for five sites by using Monte Carlo simulation method, using scenario sampling method to combine seismic and thermal loads and using the Rt software [22, 23]. Tables 6 and 7 show the reliability index for the bending and shearing failure limit states for each of five sites. In these tables, the target reliability indexes are also shown and the resultant indexes under combined effect of seismic and thermal can be compared with them. As shown in Tables 6 and 7, for both limit states, for all considered sites when seismic and thermal loads combined, the reliability indexes and therefore the safety level have been reduced. Therefore, for pile bending and shearing limit states under combined effect of seismic and thermal loads, the AASHTO LRFD [11] specifications will not produce a responsible reliability index, β , by comparing resultant indexes with target indexes.

TABLE 6: Reliability indexes for the bending moment limit state under combined seismic and thermal loads.

Site	Reliability indexes under combined effect, β_{EQ+TU}	Target reliability indexes β_T
San Francisco	2.21	2.223
Seattle	2.211	2.23
Memphis	2.52	2.57
New York	2.08	2.12
St. Paul	2.07	2.27

TABLE 7: Reliability indexes for the shearing limit state under combined seismic and thermal loads.

Site	Reliability indexes under combined effect, β_{EQ+TU}	Target reliability indexes β_T
San Francisco	2.10807	2.12296
Seattle	2.11144	2.20097
Memphis	2.28674	2.54758
New York	1.91	2.09
St. Paul	2.15	2.67815

7. Conclusion

Integral abutment bridges (IABs) are jointless bridges that by eliminating the expansion joints have many advantages over conventional bridges. Due to the integrity of these bridges, among the loads acting on these bridges, seismic loads have major role in designing these bridges and readily transferred to substructure and affect the design of these components. As AASHTO LRFD like other developed bridge design codes consider temperature and earthquake loads separately in their specified load combinations for the design of bridges, according to the fact that there is a temperature difference between temperature at any time of bridge life and bridge construction time temperature, a uniform temperature load is applied to the bridge. Therefore, during earthquake the existing of a uniform temperature load is an obvious matter.

Then evaluating the safety level of IABs—designed by AASHTO LRFD bridge design code—under the combination of temperature and earthquake loads during the design life of IABs is important.

In this paper, by concerning the safety of the pile foundation of an IAB designed by AASHTO LRFD bridge design code under seismic load, the target safety level of IABs has been evaluated. Then by repeating these reliability analyses for the same bridge under combination of thermal and seismic loads and comparing calculated reliability indexes with target reliability indexes, it is shown that that for an IAB designed by AASHTO LRFD the reliability indexes have been reduced under combined effects and the target level of safety during its design life is not provided.

Conflict of Interests

The authors declare that there is no conflict of interests regarding the publication of this paper.

Acknowledgment

The authors thank the Research Center of Optimization and Engineering, Tabriz, Iran, for the support.

References

- [1] N. C. M. Tsang and G. L. England, "Soil/structure interaction of integral bridge with full height abutments," in *Proceedings of the 15th ASCE Engineering Mechanics Conference*, Columbia University, New York, NY, USA, 2002.
- [2] M. Dicleli and S. M. Albhaisi, "Effect of cyclic thermal loading on the performance of steel H-piles in integral bridges with stub-abutments," *Journal of Constructional Steel Research*, vol. 60, no. 2, pp. 161–182, 2004.
- [3] W. Kim and J. A. Laman, "Integral abutment bridge response under thermal loading," *Engineering Structures*, vol. 32, no. 6, pp. 1495–1508, 2010.
- [4] I. Tegos, A. Sextos, S. Mitoulis, and M. Tsitotas, "Contribution to the improvement of seismic performance of integral Bridges," in *Proceedings of the 4th European Workshop on the Seismic Behavior of Irregular and Complex Structures*, Thessaloniki, Greece, 2005.
- [5] A. Itani and G. Pekcan, "Seismic performance of steel plate girder bridges with integral abutments," Publication no. FHWA-HIF-11-043, 2011.
- [6] R. J. Frosch, M. E. Kreger, and A. M. Talbott, "Earthquake resistance of integral abutment bridges," Publication FHWA/IN/JTRP-2008/11, Joint Transportation Research Program, Indiana Department of Transportation and Purdue University, West Lafayette, Ind, USA, 2009.
- [7] S. Maleki and S. Mahjoubi, "A new approach for estimating the seismic soil pressure on retaining walls," *Scientia Iranica*, vol. 17, no. 4 A, pp. 273–284, 2010.
- [8] N. Mononobe and H. Matsue, "On the determination of earth pressures during earthquakes," in *Proceedings of the World Engineering Congress*, vol. 9, pp. 176–182, 1929.
- [9] W. Kim, *Load and resistance factor for integral abutment bridges [Ph.D. dissertation]*, Pennsylvania State University, University Park, Pa, USA, 2008.
- [10] "European Standard EN 1998-2: has the status of a British Standard," Eurocode 8, Bridges, 2005.
- [11] *AASHTO LRFD Bridge Design Specifications*, American Association of State Highway and Transportation Officials, Washington, DC, USA, 2012.
- [12] A. Frankel, S. Harmsen, C. Mueller et al., "Uniform hazard spectra, de-aggregation, and uncertainty," in *Proceedings of FHWA/NCEER Workshop on the National Representation of Seismic Ground Motion for New and Existing Highway Facilities*, NCEER Technical Report 97-0010, pp. 39–73, SUNY Buffalo, NY, USA, 1997.
- [13] A. S. Nowak, "Calibration of LRFD bridge design code," A.S. NCHRP Report, Transportation Research Board of the National Academies, Washington, DC, USA, 1999.
- [14] D. E. Becker, "Eighteenth Canadian geotechnical colloquium: Limit states design for foundations. Part II. Development for the national building code of Canada," *Canadian Geotechnical Journal*, vol. 33, no. 6, pp. 984–1007, 1996.
- [15] B. Ellingwood, T. V. Galambos, J. G. MacGregor, and C. A. Comell, *Development of a Probability Based Load Criterion for American National Standard A58*, National Bureau of Standards, Washington, DC, USA, 1980.

- [16] U.S. Geological Survey, USGS, 2013, <http://earthquake.usgs.gov/earthquakes/>.
- [17] A. K. Chopra and R. K. Goel, "Building period formulas for estimating seismic displacements," *Earthquake Spectra*, vol. 16, no. 2, pp. 533–536, 2000.
- [18] Weather online, 2013, <http://www.weather.com/weather/wxclimatology/USWA0395>.
- [19] C. J. Turkstra and H. O. Madsen, "Load Combinations in Codified Structural Design," *Journal of Structural Engineering*, vol. 106, no. 12, pp. 2527–2543, 1980.
- [20] J. Ferry Borges and M. Castanheta, *Structural Safety: Course 101*, Laboratorio Nacional de Engenharia Civil, Lisbon, Portugal, 2nd edition, 1971.
- [21] Y. K. Wen, *Structural Load Modeling and Combination for Performance and Safety Evaluation*, Elsevier, New York, NY, USA, 1990.
- [22] M. Mahsuli, *Probabilistic models, methods, and software for evaluating risk to civil infrastructure [A thesis submitted in partial fulfillment of the requirements for the degree of doctor of philosophy in the faculty of graduated studies]*, The University of British Columbia, Vancouver, Canada, 2012.
- [23] M. Mahsuli and T. Haukaas, "Computer program for multi-model reliability and optimization analysis," *Journal of Computing in Civil Engineering*, vol. 27, no. 1, pp. 87–98, 2013.
- [24] M. Ghosn, F. Moses, and J. Wang, "Design of highway bridges for extreme events," NCHRP Report 489, Transportation Research Board of the National Academies, Washington, DC, USA, 2003.
- [25] Weather Site, 2013, <http://www.wunderground.com/history/>.
- [26] M. Lemaire, *Structural Reliability*, ISTE, London, UK; John Wiley & Sons, Hoboken, NJ, USA, 2009.
- [27] T. V. Galambos and M. K. Ravindra, "Properties of Steel for Use in LRFD," *Journal of the Structural Division*, vol. 104, no. 9, pp. 1459–1468, 1978.
- [28] C. W. Roeder, "Thermal movement design procedure for steel and concrete bridges," A Report to the National Cooperative Highway Research Program NCHRP 20-07/106, 2002.
- [29] N. Mononobe and H. Matsue, "On the determination of earth pressures during earthquakes," in *Proceedings of the World Engineering Conference*, vol. 9, p. 176, 1929.
- [30] S. Okabe, "General theory of earth pressure," *Journal of the Japanese Society of Civil Engineers*, vol. 12, no. 1, 1926.
- [31] H. B. Seed and R. V. Whitman, "Design of earth retaining structures for dynamic loads," in *Proceedings of the Specialty Conference on Lateral Stresses in the Ground and Design of Earth Retaining Structures*, pp. 47–103, ASCE, 1970.

Research Article

Performance-Based Seismic Design of Steel Frames Utilizing Colliding Bodies Algorithm

H. Veladi^{1,2}

¹ Department of Civil Engineering, University of Tabriz, Tabriz, Iran

² The Research Center of Optimization and Engineering, Tabriz, Iran

Correspondence should be addressed to H. Veladi; hveladi@tabrizu.ac.ir

Received 23 July 2014; Revised 4 August 2014; Accepted 4 August 2014; Published 14 August 2014

Academic Editor: Siamak Talatahari

Copyright © 2014 H. Veladi. This is an open access article distributed under the Creative Commons Attribution License, which permits unrestricted use, distribution, and reproduction in any medium, provided the original work is properly cited.

A pushover analysis method based on semirigid connection concept is developed and the colliding bodies optimization algorithm is employed to find optimum seismic design of frame structures. Two numerical examples from the literature are studied. The results of the new algorithm are compared to the conventional design methods to show the power or weakness of the algorithm.

1. Introduction

The traditional seismic design practice entails specifying the desired performance objective, and subsequently the structure is designed to meet specific performance levels. Performance-based design is a more general approach which tries to design buildings with predictable loading-induced performance, rather than being based on prescriptive mostly empirical code specifications. The earthquakes and strong winds are the two major loading conditions imposed on buildings and the performance-based seismic design is becoming well accepted in professional practice for the design of buildings under seismic loading [1]. In performance-based seismic design, the criteria are expressed in terms of achieving a set of performance objectives while the structure is under levels of seismic hazard [2].

Performance-based design methodology allows a significantly different approach for formulating optimization problems, leading to the field of performance-based design optimization (PBDO) [3–7]. In recent years, extensive research has been carried out on RBDO problems [8–12]. Also, various approaches were developed using sequential approximate programming concept [13, 14], the optimality criteria (OC) algorithm [15], and a line search strategy [15]. The metaheuristic algorithms such genetic algorithm (GA) as well as ant colony optimization (ACO) [15], particle swarm

optimization (PSO) [16], and charged system search (CSS) [17] (developed by Kaveh and Talatahari [18]) are also some other variants which were utilized for PBDO problems.

This paper presents a new developed method, the so-called colliding bodies optimization algorithm (CBO) [19], to determine optimum design of steel frames considering four performance levels. The nonlinear analysis is required to reach the structural response at various performance levels. Nonlinear static analysis, as a pushover analysis, is a method for performance-based design of structures. Based on this method, earthquake effects such as displacements or forces can be applied to structure statically in some stages from zero to a proposed value, and in each stage the nonlinear internal forces and nodal displacements are calculated and used for the next stage [20]. In [21], a second order analysis of members including geometrical nonlinearly (using semirigid steel framework concept) has been presented to the pushover analysis for performance based seismic design.

2. Optimal Performance-Based Seismic Design of Buildings

In structural design, it is desirable to reach a proposed service-ability level with the least usage of the material [16]. Performance level is the required behavior of a structure in

different situations. Here, we utilize four performance levels as follows [16].

(a) *Operational Level*. In earthquake situation with probability of exceeding equal to 50% in 50 years structure life, the structure must remain elastic and lateral drift in center of gravity at roof level must be lesser than allowable value:

$$\text{OP Level } \Delta^{\text{OP}} \leq \bar{\Delta}^{\text{OP}}, \quad (1)$$

where Δ^{OP} is the lateral drift in center of gravity at roof level and $\bar{\Delta}^{\text{OP}}$ is the allowable lateral drift in center of gravity at roof level both in operational level.

(b) *Immediate Occupancy*. In earthquake situation with probability of exceeding equal to 20% in 50 years structure life, lateral drift in center of gravity at roof level must be lesser than allowable value:

$$\text{IO Level } \Delta^{\text{IO}} \leq \bar{\Delta}^{\text{IO}}, \quad (2)$$

where Δ^{IO} is the lateral drift in center of gravity at roof level and $\bar{\Delta}^{\text{IO}}$ is the allowable lateral drift in center of gravity at roof level both in immediate occupancy level.

(c) *Life Safety*. In earthquake situation with probability of exceeding equal to 10% in 50 years structure life, lateral drift in center of gravity at roof level must be lesser than allowable value:

$$\text{LS Level } \Delta^{\text{LS}} \leq \bar{\Delta}^{\text{LS}}, \quad (3)$$

where Δ^{LS} is the lateral drift in center of gravity at roof level and $\bar{\Delta}^{\text{LS}}$ is the allowable lateral drift in center of gravity at roof level both in life safety level.

(d) *Collapse Prevention*. In earthquake situation with probability of exceeding equal to 2% in 50 years structure life, the structure must remain stable and lateral drift in center of gravity at roof level must be lesser than allowable value:

$$\text{CP Level } \Delta^{\text{CP}} \leq \bar{\Delta}^{\text{CP}}, \quad (4)$$

where Δ^{CP} is the lateral drift in center of gravity at roof level and $\bar{\Delta}^{\text{CP}}$ is the allowable lateral drift in center of gravity at roof level both in immediate occupancy level.

Roof drift of 0.4%, 0.7%, 2.5%, and 5% of the height of structure is taken as allowable roof drift for OP, IO, LS, and CP performance levels in design optimization process, respectively [22].

The structural optimization problems can be expressed as minimizing the weight of structures as

$$\text{Minimize: } W(X) = \sum_{j=1}^{ne} \rho \cdot L_j \cdot A_j, \quad (5)$$

where $W(X)$ is the weight of the structure; X is the vector of design variables taken from W -shaped sections found in

the AISC design manual [23]; ne is the number of members; ρ is the material mass density; L_j and A_j are the length and the cross-sectional area of the member j , respectively.

To predict the seismic demands on building frameworks, a developed computer-based pushover analysis procedure is utilized. The analysis process is inspired of second-order inelastic analysis of semirigid framed structures where rigidity factor is replaced with plasticity factor in stiffness matrix. The detailed explanations are presented in [15, 16].

3. Colliding Bodies Optimization

3.1. *Laws of the Collision between Two Bodies* [19]. In physics, collisions between bodies are governed by laws of momentum and energy. When a collision occurs in an isolated system, the total momentum of the system of objects is conserved.

Provided that there are no net external forces acting upon the objects, the momentum of all objects before the collision equals the momentum of all objects after the collision.

The conservation of the total momentum demands that the total momentum before the collision is the same as the total momentum after the collision and is expressed by the following equation:

$$m_1 v_1 + m_2 v_2 = m_1 v'_1 + m_2 v'_2, \quad (6)$$

Likewise, the conservation of the total kinetic energy is expressed by

$$\frac{1}{2} m_1 v_1^2 + \frac{1}{2} m_2 v_2^2 = \frac{1}{2} m_1 v'^2_1 + \frac{1}{2} m_2 v'^2_2 + Q, \quad (7)$$

where v_1 and v_2 are the initial velocity of the first and second objects before impact, respectively; v'_1 and v'_2 are the final velocity of the first and second objects after impact; m_1 and m_2 are the mass of the first and second objects; and Q is the loss of kinetic energy due to the impact.

The formulas for the velocities after a one-dimensional collision are

$$v'_1 = \frac{(m_1 - \varepsilon m_2) v_1 + (m_2 + \varepsilon m_1) v_2}{m_1 + m_2}, \quad (8)$$

$$v'_2 = \frac{(m_2 - \varepsilon m_1) v_1 + (m_1 + \varepsilon m_2) v_2}{m_1 + m_2},$$

where ε is the coefficient of restitution (COR) of two colliding bodies, defined as the ratio of relative velocity of separation to relative velocity of approach.

3.2. *Theory*. The colliding bodies optimization algorithm is one of the metaheuristic search methods recently developed [19]. The idea of the CBO algorithm is based on observation of a collision between two objects in one dimension, in which one object collides with another object and they move toward minimum energy level. It is a population-based search approach, where each agent is considered as a colliding body with mass. The CBO procedure can briefly be outlined as follows.

- (i) The initial positions of CBs are determined with random initialization of a population of individuals in the search space:

$$x_i^0 = x_{\min} + \text{rand}(x_{\max} - x_{\min}), \quad (9)$$

where x_i^0 determines the initial value vector of the i th CB. x_{\min} and x_{\max} are the minimum and the maximum allowable values vectors of variables; rand is a random number in the interval $[0, 1]$; n is the number of CBs.

- (ii) The magnitude of the body mass for each CB is defined as

$$m_k = \frac{1/f_k}{\sum_{i=1}^n (1/f_i)}, \quad (10)$$

where f_k represents the objective function value of the agent k ; n is the population size. Obviously a CB with good values exerts a larger mass than bad ones.

- (iii) The arrangement of the CBs objective function values is performed in ascending order. The sorted CBs are equally divided into two groups.

- (a) The lower half of CBs (stationary CBs): these CBs are good agents which are stationary and the velocity of these bodies before collision is zero. Thus,

$$v_i = 0 \quad i = 1, \dots, \frac{n}{2}. \quad (11)$$

- (b) The upper half of CBs (moving CBs): these CBs move toward the lower half. Then, the better and worse CBs, that is, agents with upper fitness value of each group, will collide together. The change of the body position represents the velocity of these bodies before collision as

$$v_i = x_i - x_{i-(n/2)} \quad i = \frac{n}{2} + 1, \dots, n, \quad (12)$$

where v_i and x_i are the velocity and position vector of the i th CB in this group, respectively; $x_{i-(n/2)}$ is the i th CB pair position of x_i in the previous group.

- (iv) After the collision, the velocity of bodies in each group is evaluated using (8) and the velocities before collision. The velocity of each moving CB after the collision is

$$v_i' = \frac{(m_i - \varepsilon \cdot m_{i-(n/2)}) \cdot v_i}{(m_i + m_{i-(n/2)})}, \quad i = \frac{n}{2} + 1, \dots, n, \quad (13)$$

where v_i and v_i' are the velocity of the i th moving CB before and after the collision, respectively. Also, the velocity of each stationary CB after the collision is

$$v_i' = \frac{(m_{i+(n/2)} + \varepsilon \cdot m_{i+(n/2)}) \cdot v_{i+(n/2)}}{(m_i + m_{i+(n/2)})} \quad i = 1, \dots, \frac{n}{2}, \quad (14)$$

where $v_{i+(n/2)}$ and v_i' are the velocity of the i th moving CB pair before the collision and the i th stationary CB after the collision, respectively; ε is the coefficient of restitution (COR) and for most of the real objects, and its value is between 0 and 1. It is defined as the ratio of the separation velocity of two agents after collision to the approach velocity of two agents before collision. In the CBO algorithm, this index is used to control of the exploration and exploitation rate [19]. In this paper, the COR decreases linearly from unit (in starting) to zero (in the end of searching).

- (v) New positions of CBs are obtained using the generated velocities after the collision in position of stationary CBs. The new positions of each moving CB are

$$X_i^{\text{new}} = X_{i-(n/2)} + \text{rand} \circ v_i', \quad i = \frac{n}{2} + 1, \dots, n, \quad (15)$$

where X_i^{new} and v_i' are the new position and the velocity after the collision of the i th moving CB, respectively; $X_{i-(n/2)}$ is the old position of i th stationary CB pair. rand is a random vector uniformly distributed in the range $(-1, 1)$ and the sign “ \circ ” denotes an element-by-element multiplication.

Also, the new position of each stationary CB is obtained as

$$X_i^{\text{new}} = X_i + \text{rand} \circ v_i', \quad i = 1, \dots, \frac{n}{2}, \quad (16)$$

where X_i^{new} , X_i , and v_i' are the new position, old position, and the velocity after the collision of the i th stationary CB, respectively.

- (vi) The optimization is repeated until a termination criterion, specified as the maximum number of iteration, is satisfied. It should be noted that a body’s status (stationary or moving body) and its numbering are changed in two subsequent iterations.

The main steps of CBO algorithm are as follows.

Step 1. The initial positions of CBs are determined randomly in the search space.

Step 2. The magnitude of the body mass for each CB is defined.

Step 3. The arrangement of the CBs objective function values is performed in ascending order. The sorted CBs are equally divided into two groups: stationary and moving CBs.

Step 4. After the collision, the velocity of bodies in each group is evaluated and the new positions of CBs are evaluated using the generated velocities after the collision in position of stationary moving CBs.

Step 5 (termination criterion control). Steps 2, 3, and 4 are repeated until a termination criterion is satisfied.

Since the algorithm is a continuous algorithm, for solving the discrete problem like the performance-based design of

TABLE 1: The statistical information of performance-based optimum designs for the 4-bay 3-story frame.

Algorithm	This work	Hybrid CSS [17]	PSACO [16]	PSO [16]	ACO [15]	GA [15]	A conventional design [21]
Best weight (kN)	280.32	273.7	279.2	286.3	283.4	303.9	412.9 kN
Average weight (kN)	292.36	286.7	290.4	302.4	294.3	321.5	—
Worst weight (kN)	308.63	297.8	298.5	310.7	303.2	339.7	—
Std. Dev. (kN)	5.786	5.651	6.453	10.453	7.566	14.332	—
Average number of analyses	4,500	4,500	4,500	8,500	3,900	6,800	—

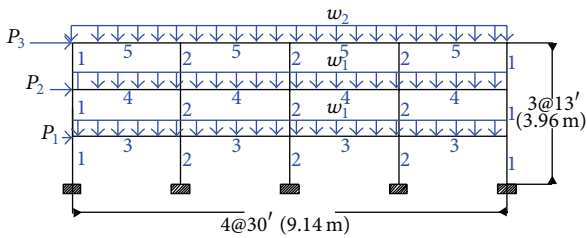


FIGURE 1: Three-story steel moment frame.

frames it is necessary to make some modifications. Here, we use a rounding function which changes the continuous value of a result to the nearest discrete value. Although this change is simple and efficient, it may reduce the exploration of the algorithm, [24].

4. Design Examples

Two building frameworks are selected for seismic optimum design using the metaheuristic algorithm [15–17]. These frames have previously been used to illustrate the pushover analysis technique by Hasan et al. [21] and Talatahari [16]. For the CBO algorithm, a number of 30 CBs are utilized and the maximum number of iterations is considered as 200.

The expected yield strength of steel material used for column members is $\sigma_{ye} = 397$ MPa, while $\sigma_{ye} = 339$ MPa is considered for beam members. The constant gravity load w is accounted for a tributary area width of 4.57 m and dead load and live load factors of 1.2 and 1.6, respectively. For each example, 30 independent runs are carried out using the new algorithms and compared with other algorithms.

4.1. Four-Bay Three-Story Steel Frame. The configuration, grouping of the members and applied loads of the four-bay three-story framed structure are shown in Figure 1 [15]. The 27 members of the structure are categorized into five groups, as indicated in the figure. The modulus of elasticity is taken as $E = 200$ GPa. The constant gravity load of $w_1 = 32$ kN/m is applied to the first and second story beams, while the gravity load of $w_2 = 28.7$ kN/m is applied to the roof beams. The seismic weight is 4,688 kN for each of the first and second stories and 5,071 kN for the roof story.

The optimum results for the CBO, a hybrid CSS [17], PACO [16], PSO [15], ACO [15], and GA [15] metaheuristic algorithm are presented in Table 1. The new algorithm as well as the CSS and PSACO needs 4500 analyses to reach

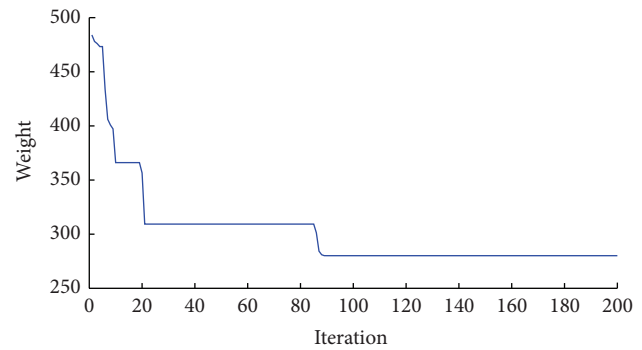


FIGURE 2: Convergence history of the CBO algorithm for the 4-bay 3-story frame.

a convergence while 3900, 6800, and 8500 analyses are required by the ACO, GA, and PSO. After performing optimal design of structure, a pushover analysis is applied to the result obtained using the CBO and roof drifts are controlled in various performance levels. The results show that the roof drifts are less than their corresponding allowable values. The best design for the CBO method has 280.32 kN weight, which is lighter than the conventional design. Although it is heavier than some of metaheuristic algorithms, the differences are small and its standard deviation value in a series of 30 different runs is better than the other methods. The convergence history of the CBO algorithm is presented in Figure 2.

4.2. Five-Bay Nine-Story Steel Frame. A five-bay nine-story steel frame is considered as shown in Figure 3. The material has a modulus of elasticity equal to $E = 200$ GPa. The 108 members of the structure are categorized into fifteen groups, as indicated in the figure. The constant gravity load of $w_1 = 32$ kN/m is applied to the beams in the first to the eighth story, while $w_2 = 28.7$ kN/m is applied to the roof beams. The seismic weights are 4,942 kN for the first story, 4,857 kN for each of the second to eighth stories, and 5,231 kN for the roof story. In this example, each of the five beam element groups is chosen from all 267 W-shapes, while the eight column element groups are limited to W14 sections (37 W-shapes).

The statistical results obtained by the metaheuristic algorithms are presented in Table 2. The best results of the new method is in a frame weighing 1600.25 kN. In order to converge to a solution for the new algorithm, approximately 5,500 frame analyses are required which are less than the 5,600, 6,000, 12,500, and 9,700 analyses necessary for

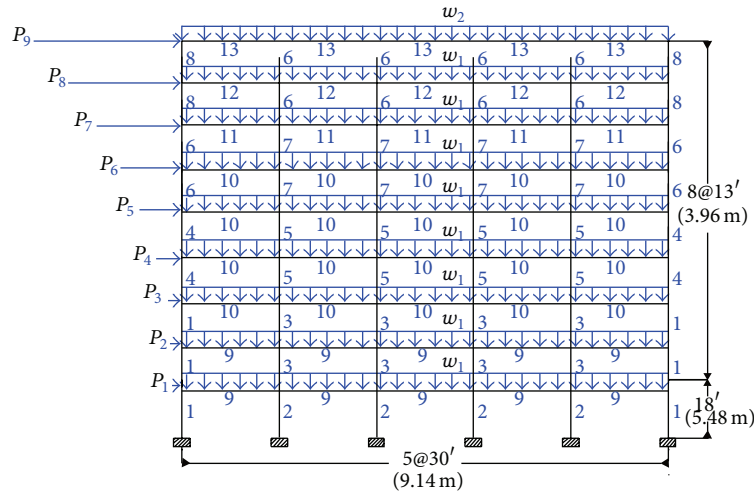


FIGURE 3: Nine-story steel moment frame.

TABLE 2: The statistical information of performance-based optimum designs for the 4-bay 9-story frame.

Algorithm	This work	Hybrid CSS [17]	PSACO [16]	PSO [16]	ACO [15]	GA [15]
Best weight (kN)	1600.25	1568.66	1601.32	1682.63	1631.83	1723.1
Average weight (kN)	1660.36	1626.32	1650.55	1725.36	1696.2	1791.4
Worst weight (kN)	1780.62	1725.36	1759.65	1813.25	1786.94	1943.2
Std. Dev. (kN)	31.02	30.35	38.52	66.35	49.33	78.33
Average number of analyses	5,500	5,000	6,000	12,500	5,600	9,700

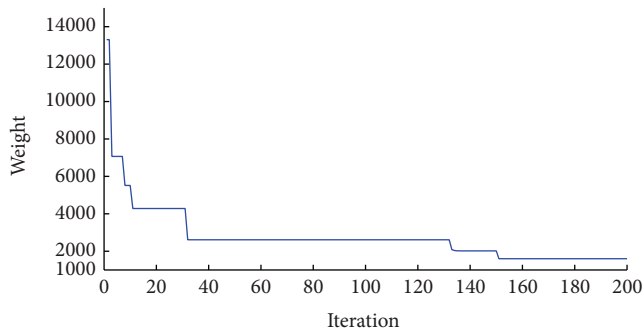


FIGURE 4: Convergence history of the CBO algorithm for the 4-bay 9-story frame.

the ACO, PSACO, PSO, and GA, respectively. The hybrid CSS needs only 5,000 analyses to find an optimum result. Figure 4 shows the convergence history for this example obtained by the CBO algorithm.

5. Conclusion Remarks

Performance-based design is a general approach which tries to design buildings with predictable loading-induced performance. In performance-based seismic design, the criteria are expressed in terms of achieving a set of performance objectives while the structure is under levels of seismic hazard. In this paper, the performance-based design of

frame structures is formulated to be optimized by the new algorithm, the colliding bodies' optimization. In order to control the lateral drift of building frameworks under seismic loading, a nonlinear analysis is utilized. The analysis method is based on a second order analysis of members including geometrical nonlinearly (using semirigid steel framework concept). The best, average, worst, and standard deviations of minimum weights are obtained by some metaheuristic algorithms as well as the CBO. Although the CBO cannot find the best results, the differences between the results of the CBO algorithm and the best one were small, and the new algorithm did not improve the results significantly.

Conflict of Interests

The author declares that there is no conflict of interests regarding the publication of this paper.

References

- [1] M. F. Huang, C. M. Chan, and W. J. Lou, "Optimal performance-based design of wind sensitive tall buildings considering uncertainties," *Computers and Structures*, vol. 98-99, pp. 7-16, 2012.
- [2] A. Ghobarah, "Performance-based design in earthquake engineering: state of development," *Engineering Structures*, vol. 23, no. 8, pp. 878-884, 2001.
- [3] B. D. Youn, K. K. Choi, and Y. H. Park, "Hybrid analysis method for reliability-based design optimization," *Journal of Mechanical Design, Transactions of the ASME*, vol. 125, no. 2, pp. 221-232, 2003.

- [4] C. M. Foley, "Optimized performance-based design for buildings," in *Recent Advance in Optimal Structural Design*, S. A. Burns, Ed., pp. 169–240, ASCE, Reston, Va, USA, 2002.
- [5] X. Zou and C. Chan, "An optimal resizing technique for seismic drift design of concrete buildings subjected to response spectrum and time history loadings," *Computers and Structures*, vol. 83, no. 19-20, pp. 1689–1704, 2005.
- [6] C. M. Chan, J. K. L. Chui, and M. R. Huang, "Integrated aerodynamic load determination and stiffness design optimization of tall buildings," *Structural Design of Tall and Special Buildings*, vol. 18, no. 1, pp. 59–80, 2009.
- [7] C. M. Chan, M. F. Huang, and K. C. S. Kwok, "Stiffness optimization for wind-induced dynamic serviceability design of tall buildings," *Journal of Structural Engineering*, vol. 135, no. 8, pp. 985–997, 2009.
- [8] D. M. Frangopol and K. Maute, "Life-cycle reliability-based optimization of civil and aerospace structures," *Computers and Structures*, vol. 81, no. 7, pp. 397–410, 2003.
- [9] D. M. Frangopol and F. Moses, "Reliability-based structural optimization," in *Advances in Design Optimization*, H. Adeli, Ed., pp. 492–570, Chapman and Hall, London, UK, 1994.
- [10] G. Cheng, G. Li, and Y. Cai, "Reliability-based structural optimization under hazard loads," *Structural and Multidisciplinary Optimization*, vol. 16, no. 2-3, pp. 128–135, 1998.
- [11] T. H. Lee and J. J. Jung, "A sampling technique enhancing accuracy and efficiency of metamodel-based RBDO: constraint boundary sampling," *Computers and Structures*, vol. 86, no. 13-14, pp. 1463–1476, 2008.
- [12] X. K. Zou, Q. Wang, G. Li, and C. M. Chan, "Integrated reliability-based seismic drift design optimization of base-isolated concrete buildings," *Journal of Structural Engineering*, vol. 136, no. 10, pp. 1282–1295, 2010.
- [13] G. D. Cheng, L. Xu, and L. Jiang, "A sequential approximate programming strategy for reliability-based structural optimization," *Computers and Structures*, vol. 84, no. 21, pp. 1353–1367, 2006.
- [14] P. Yi and G. Cheng, "Further study on efficiency of sequential approximate programming for probabilistic structural design optimization," *Structural and Multidisciplinary Optimization*, vol. 35, no. 6, pp. 509–522, 2008.
- [15] A. Kaveh, B. Farahmand Azar, A. Hadidi, F. Rezazadeh Sorochi, and S. Talatahari, "Performance-based seismic design of steel frames using ant colony optimization," *Journal of Constructional Steel Research*, vol. 66, no. 4, pp. 566–574, 2010.
- [16] S. Talatahari, "Optimum performance-based seismic design of frames using meta-heuristic optimization algorithms," in *Metaheuristic Applications in Structures and Infrastructures*, Elsevier, 2013.
- [17] S. Talatahari, A. Hosseini, S. R. Mirghaderi, and F. Rezazadeh, "Optimum performance-based seismic design using a hybrid optimization algorithm," *Mathematical Problems in Engineering*, vol. 2014, Article ID 693128, 8 pages, 2014.
- [18] A. Kaveh and S. Talatahari, "A novel heuristic optimization method: charged system search," *Acta Mechanica*, vol. 213, no. 3-4, pp. 267–289, 2010.
- [19] A. Kaveh and V. R. Mahdavi, "Colliding bodies optimization: a novel meta-heuristic method," *Computers & Structures*, vol. 139, no. 15, pp. 18–27, 2014.
- [20] L. Xu, "Geometrical stiffness and sensitivity matrices for optimization of semi-rigid steel frameworks," *Structural Optimization*, vol. 5, no. 1-2, pp. 95–99, 1992.
- [21] R. Hasan, L. Xu, and D. E. Grierson, "Push-over analysis for performance-based seismic design," *Computers and Structures*, vol. 80, no. 31, pp. 2483–2493, 2002.
- [22] Federal Emergency Management Agency FEMA-350, *Recommended Seismic Design Criteria for New Steel Moment-Frame Buildings*, SAC Joint Venture, Sacramento, Calif, USA, 2000.
- [23] *Manual of Steel Construction, Load and Resistance Factor Design*, American Institute of Steel Construction, Chicago, Ill, USA, 2001.
- [24] A. Kaveh and S. Talatahari, "A discrete particle swarm ant colony optimization for design of steel frames," *Asian Journal of Civil Engineering*, vol. 9, no. 6, pp. 563–575, 2008.

Research Article

A Parametric Study of Nonlinear Seismic Response Analysis of Transmission Line Structures

Li Tian,¹ Yanming Wang,¹ Zhenhua Yi,¹ and Hui Qian²

¹ School of Civil and Hydraulic Engineering, Shandong University, Jinan 250061, China

² School of Civil Engineering, Zhengzhou University, Zhengzhou 450001, China

Correspondence should be addressed to Li Tian; tianli@sdu.edu.cn

Received 13 May 2014; Accepted 1 July 2014; Published 15 July 2014

Academic Editor: Fei Kang

Copyright © 2014 Li Tian et al. This is an open access article distributed under the Creative Commons Attribution License, which permits unrestricted use, distribution, and reproduction in any medium, provided the original work is properly cited.

A parametric study of nonlinear seismic response analysis of transmission line structures subjected to earthquake loading is studied in this paper. The transmission lines are modeled by cable element which accounts for the nonlinearity of the cable based on a real project. Nonuniform ground motions are generated using a stochastic approach based on random vibration analysis. The effects of multicomponent ground motions, correlations among multicomponent ground motions, wave travel, coherency loss, and local site on the responses of the cables are investigated using nonlinear time history analysis method, respectively. The results show the multicomponent seismic excitations should be considered, but the correlations among multicomponent ground motions could be neglected. The wave passage effect has a significant influence on the responses of the cables. The change of the degree of coherency loss has little influence on the response of the cables, but the responses of the cables are affected significantly by the effect of coherency loss. The responses of the cables change little with the degree of the difference of site condition changing. The effect of multicomponent ground motions, wave passage, coherency loss, and local site should be considered for the seismic design of the transmission line structures.

1. Introduction

Transmission line structures are very important to electric engineering. Most of the transmission lines cross the highly seismic region. The past earthquakes indicate that transmission lines are often damaged under earthquake loading. About 100 transmission lines of Los Angeles city were destroyed in the 1992 Landers earthquake [1]. 38 transmission lines were broken during the 1995 Kobe earthquake [2]. Many transmission lines were pulled off in the 2008 Wenchuan earthquake [3]. A lot of transmission lines were ruptured during the 2013 Lushan earthquake. To guarantee the safety of transmission lines during earthquake, the parametric study of nonlinear responses of the transmission line structures under earthquake loading should be accurately obtained.

Most of research has focused on the actions of static load, impulsive load, and equivalent static wind load. There are no calculation methods about how to consider the transmission line structures under earthquake loading in current seismic

codes [4, 5]. Some research has been performed to analyze the seismic responses of transmission tower and transmission line under earthquake loading. Li et al. [6, 7] have completed a number of studies on seismic effects on transmission towers and have verified that the effect of transmission lines in seismic design should not be neglected.

With the development of techniques, the spans of transmission lines have increased dramatically. It is unrealistic to assume that earthquake ground motions for long span transmission tower-line system are the same and single component. Ghobarah et al. [8] investigated the effects of multisupport excitations on the response of overhead power transmission tower and line. The results indicated that the assumption of uniform ground motions at all supports of a transmission line does not provide the most critical case for the response calculations. Tian et al. [9] studied the behavior of power transmission tower-line system subjected to spatially varying ground motions. The effects of the incident angle of the seismic wave, coherency loss, and wave

travel on the transmission tower are investigated. Li et al. [10, 11] investigated the response of a transmission tower-line system at a canyon site to spatially varying ground motions. The results showed that the effect of ground motion spatial variations should be incorporated in seismic analysis of the transmission tower-line system. In addition, Tian et al. [12] analyzed the effect of multicomponent multisupport excitations on the response of the transmission tower-line system. Multiple effect parameters were considered, but the responses of the transmission tower were obtained only. Wang et al. [13] researched the progressive collapse analysis of a transmission tower-line system under earthquake. The results indicated that the proposed procedure can provide collapse mode and vulnerable points for use in seismic performance and retrofit evaluation of structure. Furthermore, Tian et al. [14] studied seismic responses of straight line type and broken line type transmission tower-line systems subjected to nonuniform seismic excitations. The results showed that the effect of nonuniform ground motions should be considered in seismic design for the straight line type and broken line type transmission lines practical engineering. The previous study concluded that the responses of transmission tower under nonuniform and multicomponent ground motions were different from that of under uniform and single ground motion. A lot of studies about the response of transmission towers are obtained, but there is little research about the parametric study of nonlinear response of transmission line structures under earthquake loading.

The parametric studies of seismic response analysis of transmission line structures considering geometric nonlinearity subjected to earthquake loading are carried out in this paper. The transmission lines are modeled by cable element account for the nonlinearity of the cable based on a real project. The effects of multicomponent ground motions, correlations among multicomponent ground motions, wave travel, coherency loss, and local site on the responses of the cables are investigated using nonlinear time history analysis method, respectively. The analysis results could provide reference for the seismic design of the transmission line structures.

2. Transmission Line Structures Model

A typical three-dimensional finite element model of transmission line structures is established based on a real electric project in the north of China. SAP2000 finite element program is used to simulate the transmission line structures. As shown in Figure 1, the transmission line structures include three towers and four span conductors lines and ground lines. Figure 1 shows the conductor and ground lines. The longitudinal, transverse, and vertical directions of the transmission line structures are shown in Figure 1. Conductor line and ground line properties are shown in Table 1. The transmission line is modeled by 40 two-node isoparametric cable elements with three translational degrees of freedom at each node. The upper one layer line is ground cable, and the lower three layer lines are four-bundled conductor cables. The distance between adjacent transmission towers

TABLE 1: Conductor line and ground line properties.

Type	Conductor line	Ground line
Transmission line	LGJ-400/35	LGJ-95/55
Outside diameter (m)	26.82E - 3	16.00E - 3
Modulus (GPa)	65	105
Transversal cross-section (m ²)	425.24E - 6	152.81E - 6
Mass per unit length (Kg/m)	1.3490	0.6967
Expansion coefficient (1/°C)	2.05E - 005	1.55E - 005

is 400 m. The connections between transmission towers and transmission lines are hinged using insulators. The side spans of the transmission lines are hinged at the same height of middle transmission tower.

Under self-weight, the cables' configuration is a catenary. Based on the coordinate system illustrated in Figure 2, (1) was used to define the initial geometry of the cable profile [15]

$$z = \frac{H}{q} \left| \cosh(\alpha) - \cosh \left| \frac{2\beta x}{l} - \alpha \right| \right|, \quad (1)$$

where $\alpha = \sinh^{-1} |\beta(c/l) / \sin(\beta)| + \beta$, $\beta = ql/2H$, H represents the initial horizontal tension which can be obtained from a preliminary static analysis, and q denotes the uniformly distributed gravity loads along the conductor and ground lines.

3. Simulation of Nonuniform Ground Motions

An empirical coherency loss function derived from SMART-1 array is used in the paper [16]. The coherency loss function between two points i and j is

$$|\gamma_{ij}(\omega, d_{ij})| = \exp(-\beta d_{ij}) \cdot \exp \left\{ -a(\omega) \sqrt{d_{ij}} \left(\frac{\omega}{2\pi} \right)^2 \right\} \quad (2)$$

in which d_{ij} is the projected distance in the wave propagation direction between points i and j in the wave propagation direction, β is a constant, and $a(\omega)$ is a function with the form

$$a(\omega) = \begin{cases} \frac{2\pi a}{\omega} + \frac{b\omega}{2\pi} + c, & 0.314 \text{ rad/s} \leq \omega \leq 62.83 \text{ rad/s}, \\ 0.1a + 10b + c, & \omega \geq 62.83 \text{ rad/s}, \end{cases} \quad (3)$$

where the constants a , b , and c can be obtained by least-squares fitting the coherency function of recorded motions. The constants in coherency function are $a = 3.583 \times 10^{-3}$, $b = -1.811 \times 10^{-5}$, $c = 1.177 \times 10^{-4}$, and $\beta = 1.019 \times 10^{-4}$, which were obtained by processing recorded motions during Event 45 at the SMART-1 array [16], and it represents highly correlated ground motions. To compare the change of the coherency loss, different degrees of coherency loss are selected based on Bi et al.'s studies [17].

A stochastic approach based on random vibration analysis is used, and the simulated ground motion time history is iterated to be compatible with the response spectrum defined

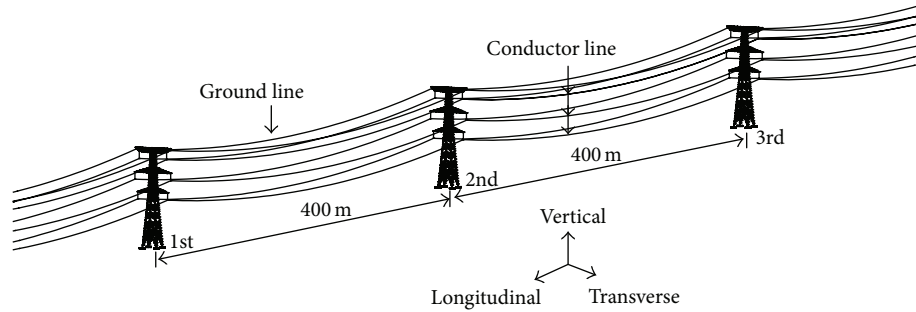


FIGURE 1: Finite element model of transmission line structures.

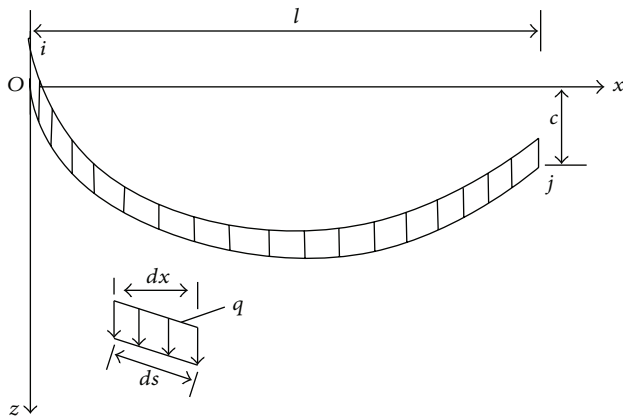


FIGURE 2: Coordinates of a single cable under self-weight.

in Code for Design of Seismic of Electrical Installations. Reference [18] gives the parameters of Clough-Penzien model according to the Code for Design of Seismic of Electrical Installations. The transmission cable structures are assumed to locate in the mid-firm soil. The peak ground motion of the longitudinal component is 0.4 g. The intensities of the transverse component and vertical component, as stated in the code, are 0.85 and 0.65 times of the longitudinal component, respectively. The three components of the ground motion are assumed to coincide with the principal axes. The three components of ground motions along a set of principal axes are uncorrelated based on Penzien and Watabe's studies [19]. Figure 3 shows acceleration time histories of three transmission tower points in longitudinal direction on mid-firm soil with apparent velocity 1000 m/s.

4. Numerical Simulation and Discussion

The parametric studies of nonlinear seismic responses of the transmission line structures under earthquake loading are analyzed using nonlinear time history analysis method. The geometric nonlinearity is taken into account due to large deformation of the transmission lines. The HHT (Hilber-Hughes-Taylor) method is applied in the numerical integration. The layers of cables shown in Figure 1 from upper to down are numbered 1, 2, 3, and 4, respectively.

TABLE 2: Selection of seismic wave.

Number	Earthquake	Event date	Magnitude	Station
①	Imperial Valley	May 18, 1940	6.7	El Centro
②	Kobe	January 16, 1995	6.9	Oka
③	Kern County	July 21, 1952	7.4	Taft

4.1. *Effect of Multicomponent Ground Motions.* To study the effect of multicomponent ground motions, three typical natural seismic waves are selected, which are El Centro wave, Oka wave, and Taft wave. The selection of seismic waves is shown in Table 2. Three components of the natural seismic waves are considered in the paper. The direction of the maximum acceleration component of the horizontal seismic wave is denoted by the horizontal 1, while the other direction component of the horizontal seismic wave is denoted by the horizontal 2, and the vertical component of seismic wave is denoted by vertical. The maximum acceleration value of the ground motion is adjusted to 0.4 g, and the other two directions are scaled according to the proportion.

Four cases are considered, longitudinal excitation only (Case 1), transverse excitation only (Case 2), vertical excitation only (Case 3), and multicomponent excitations (Case 4). Case 1 is longitudinal excitation only, and the horizontal 1 component of the seismic wave is inputted along longitudinal direction of the transmission line structures model. Case 2 is transverse excitation only, and the horizontal 2 component of the seismic wave is inputted along transverse direction of the transmission line structures model. Case 3 is vertical excitation only, and the vertical component of the seismic wave is inputted along vertical direction of the transmission line structures model. Case 4 is multicomponent excitations, and the horizontal 1, horizontal 2, and vertical component of seismic wave are inputted together along longitudinal, transverse, and vertical direction of the transmission line structures model, respectively.

The maximum value curves of the vertical displacements of the cable under different analysis cases are shown in Figure 4. It can be seen from Figure 4 that the vertical displacement of the cable under longitudinal or transverse excitation only is larger than that of under vertical seismic excitation only, so the longitudinal or transverse excitation has a great influence on the response of the vertical displacement of the cable. The vertical displacements of the cable under

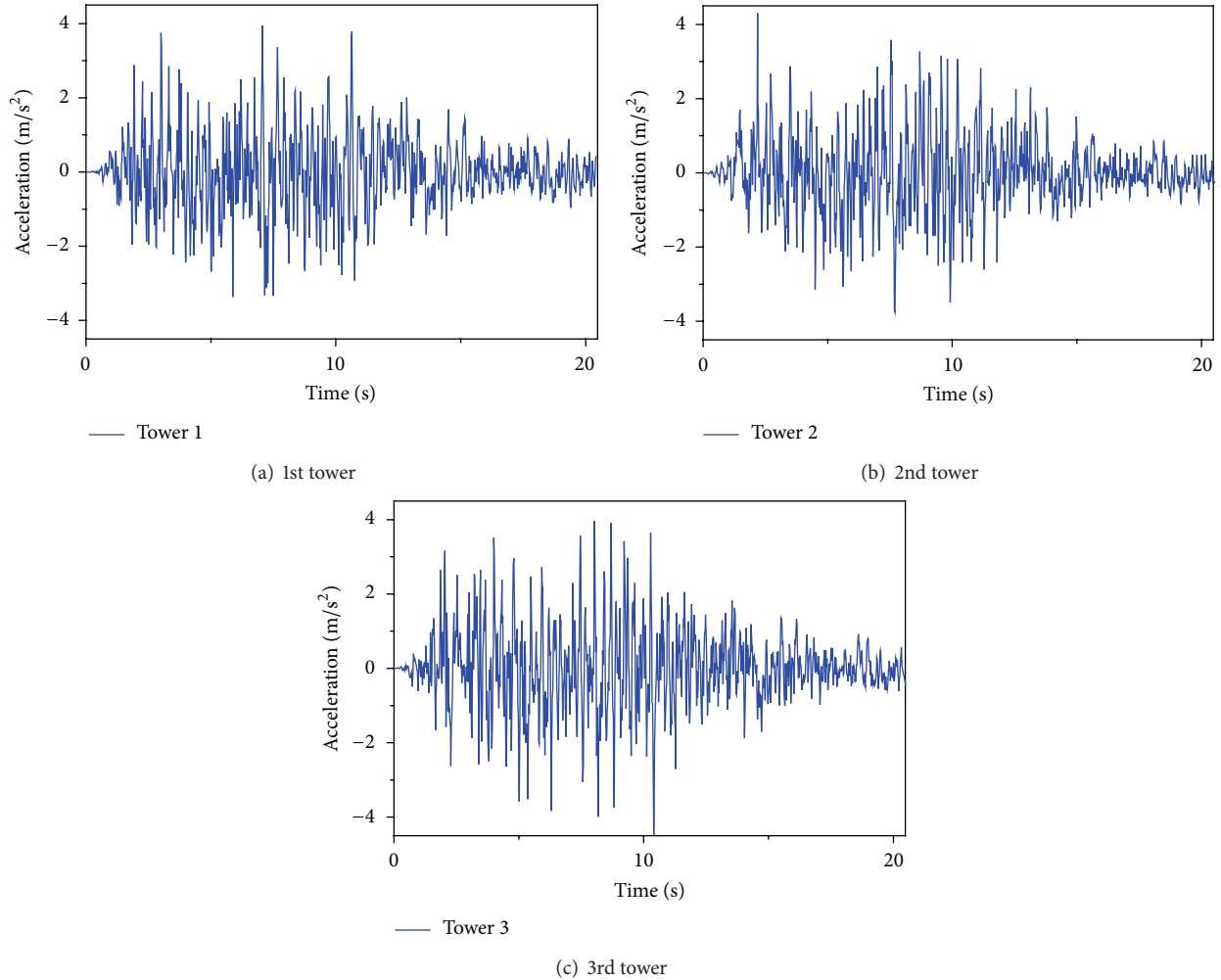


FIGURE 3: Acceleration time histories of three tower points in longitudinal direction.

multicomponent excitations are significantly larger than that of under vertical, longitudinal, or transverse excitation only. The longitudinal and transverse seismic excitations have a large coupling with the response of the vertical displacement of the cable. Therefore, multicomponent seismic excitations should be considered for the transmission line structures.

4.2. Effect of Correlations among Multicomponent Ground Motions. To research the effect of the correlations among multicomponent ground motions, four cases are considered, uniform (Case 1), $\alpha = 0^\circ$ (Case 2), $\alpha = 18^\circ$ (Case 3), and $\alpha = 45^\circ$ (Case 4). The correlations among multicomponent ground motions are selected based on previous studies [12].

The maximum values of the tension forces of the cables under different degrees of the coherence are shown in Table 3. It can be seen from Table 3 that the tension forces of the cables have an increasing tendency with the increasing of the degree of the coherence. Ignoring the correlations among the multicomponent ground motions, the results may be small, but the changes are very little. The above analysis indicates

TABLE 3: Tension forces of the cables under different degrees of the coherence (kN).

Layer	Case 1	Case 2	Case 3	Case 4
①	13.98	22.97	23.21	23.91
②	95.51	142.80	143.12	143.79
③	95.52	143.13	143.77	144.22
④	95.20	143.01	143.63	143.91

that the effect of correlations among multicomponent ground motions could be neglected.

4.3. Effect of Ground Motion Spatial Variations. To investigate the effect of ground motion spatial variations, four cases are considered, uniform (Case 1), wave passage effect only (Case 2), coherency loss effect only (Case 3), and local site effect only (Case 4). Case 1 is the uniform excitation, because the apparent velocity, coherency loss, and soil condition of

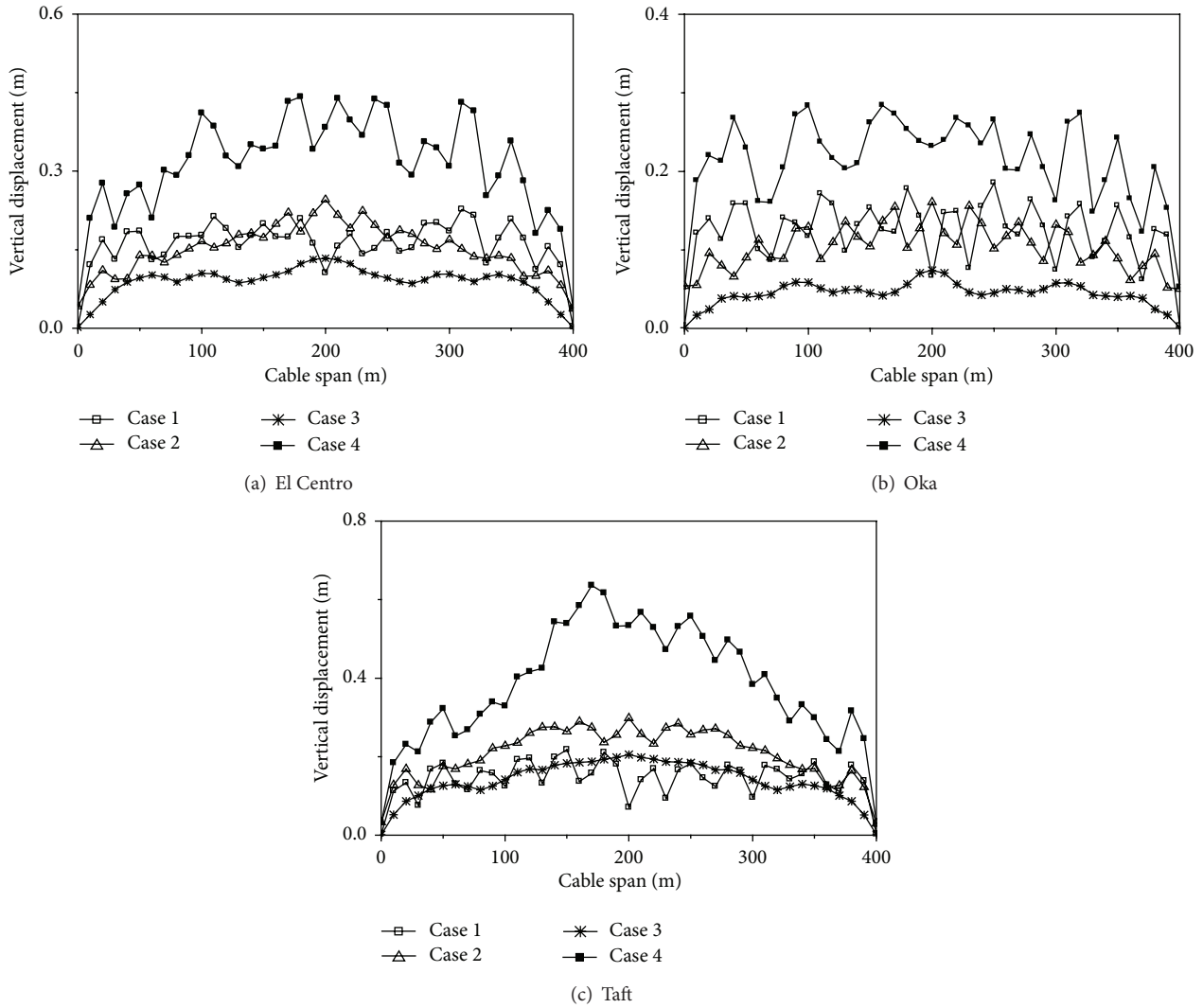


FIGURE 4: Vertical displacements of the cable under different analysis cases.

ground motion are assumed to be infinite, highly correlated, and mid-firm site, respectively.

The maximum value curves of the vertical displacements of the cable under different analysis cases are shown in Figure 5. It can be seen from Figure 5 that the vertical displacements of the cable considering wave travel effect only, coherency loss effect only, or local site effect only are larger than that of under uniform excitation. The vertical displacements of the cable considering wave travel effect only are larger than that of considering coherency loss effect only or local site effect only. Existing research [20] has shown that the wave travel effect is very important to the responses of structure when the structure is flexible, and the responses are mainly decided by dynamic response of the structure. The coherency loss effect is very important to the responses of structure when the structure is rigid, and the responses are mainly decided by quasistatic response of the structure. Therefore, wave travel effect of ground motion

is more obvious to the influence of the structure than the other effect for the flexible structure of the transmission lines.

4.4. Wave Travel Effect. To study the effect of apparent velocity, ten different velocities of wave propagation are considered in the analysis, uniform (Case 1), 200 m/s (Case 2), 400 m/s (Case 3), 600 m/s (Case 4), 800 m/s (Case 5), 1000 m/s (Case 6), 1200 m/s (Case 7), 1600 m/s (Case 8), 2000 m/s (Case 9), and 3000 m/s (Case 10), to cover the range of practical propagation velocities in engineering. In all these cases, the coherency loss and soil condition of ground motion are assumed to be highly correlated and the mid-firm site, respectively.

The maximum value curves of the vertical displacements of the cable under different traveling wave velocities are shown in Figure 6. It can be seen from Figure 6 that

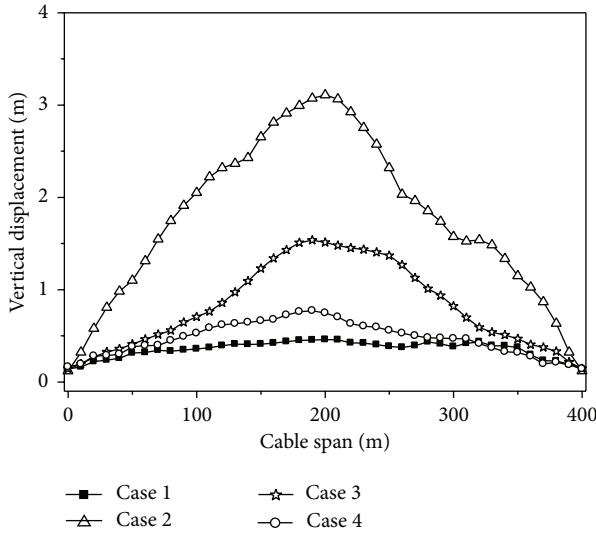


FIGURE 5: Vertical displacements of the cable under different analysis cases.

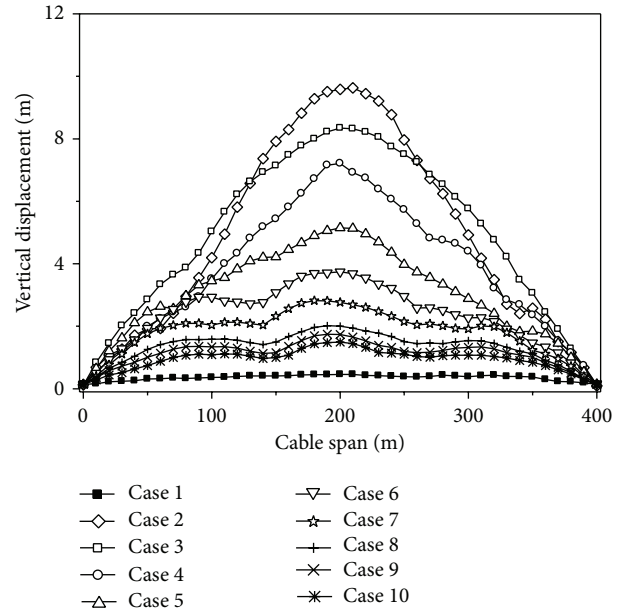


FIGURE 6: Vertical displacements of the cable under different traveling wave velocities.

the vertical displacements of the cable increase with the decreasing wave velocity. The maximum vertical displacements of the cable appear when the velocity is 200 m/s. The vertical displacements of the cable decrease with the increasing wave velocity, but it is larger than that of under uniform excitation. Therefore, the vertical displacement of the cable is very sensitive to the traveling wave velocity of the seismic wave.

The maximum value curves of tension forces of the cables under different traveling wave velocities are shown in Figure 7. The tension forces of the cables change very little when the traveling wave velocity is less than 200 m/s, but it is larger than that of under uniform excitation. With the traveling wave velocity increasing, the tension forces of the cables decrease gradually. Neglecting the wave passage effect of ground motion, the maximum tension forces of the cables could be underestimated by more than 50%.

Based on the variations of the displacements and tension forces of the cables considering the change of traveling wave velocity, the wave travel effect has a significant influence on the response of the cables. The vertical displacements of the cable are amplified greatly considering the wave travel effect. The vibration of the cable is very large, which would lead to discharge and short circuit. The tension forces of the cables considering the wave travel effect are larger than that of under uniform excitation. Because the tension forces of the cables are too large, the transmission lines would be pulled off and the situations usually occur in the past earthquakes. Therefore, it is necessary to estimate the traveling wave velocity accurately.

4.5. Coherency Loss Effect. To investigate the effect of coherency loss, uniform (Case 1), uncorrelated (Case 2), weakly (Case 3), intermediately (Case 4), highly (Case 5), and completely correlated (Case 6) ground motions are considered, respectively. It should be noted that the correlation as low

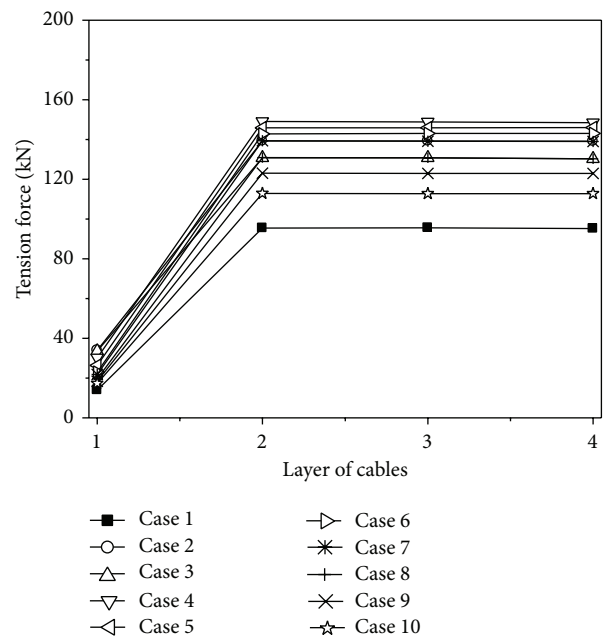


FIGURE 7: Tension forces of the cables under different traveling wave velocities.

as uncorrelated does not usually occur at short distances, unless there are considerable changes in the local geology from one support to the other. In all these cases, the apparent velocity and soil condition of ground motion are assumed to be 1000 m/s and the mid-firm site, respectively.

The maximum value curves of the vertical displacements of the cable under different degrees of coherency loss are shown in Figure 8. It can be seen from Figure 8 that the

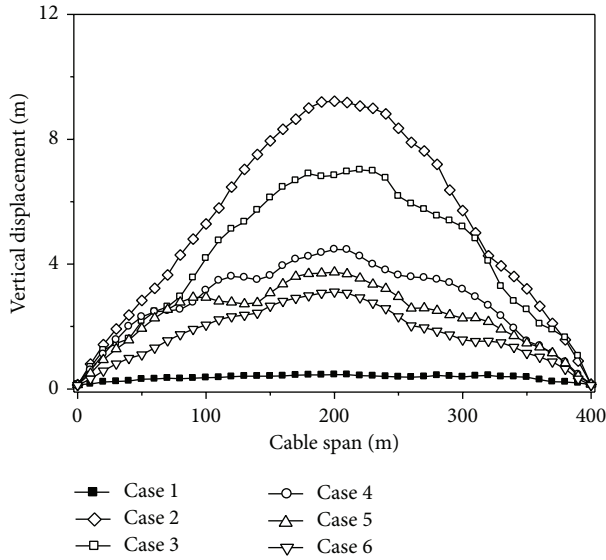


FIGURE 8: Vertical displacements of the cable under different degrees of coherency loss.

maximum vertical displacements of the cable appear when the coherency loss is uncorrelated. The vertical displacements of the cable have an increasing tendency with the decrease of the degree of coherency loss. The changes of the vertical displacements are very little when the coherency losses are intermediately, highly, and completely correlated.

The maximum value curves of tension forces of the cables under different degrees of coherency loss are shown in Figure 9. It can be seen from Figure 9 that the change of coherency loss has little influence on the tension forces of the cables, so the change of coherency loss can be ignored. The tension forces of the cables considering coherency loss effect are larger than that of under uniform excitation, so the effect of coherency loss should be considered. Neglecting the coherency loss effect of ground motion, the maximum tension forces of the cables could be underestimated by more than 50%.

The variations of the displacement and force responses of the cables considering the change of coherency loss can be obtained from the above analysis. The vertical displacements of the cable have an increasing tendency with the decrease of the degree of coherency loss. The change of coherency loss can be ignored, but the effect of coherency loss must be considered. Therefore, it is very important to consider the coherency loss effect of ground motion for the seismic design of the transmission line structures.

4.6. Local Site Effect. To research the effect of local site influence on the cable responses, eight cases are considered, Case 1~Case 8. Analysis cases considering the effect of local site are shown in Table 4. Mid-firm, mid-soft, and soft sites are denoted by F, MF, MS, and S, respectively. In all these cases, the apparent velocity and coherency of ground motion are assumed to be 1000 m/s and highly correlated, respectively.

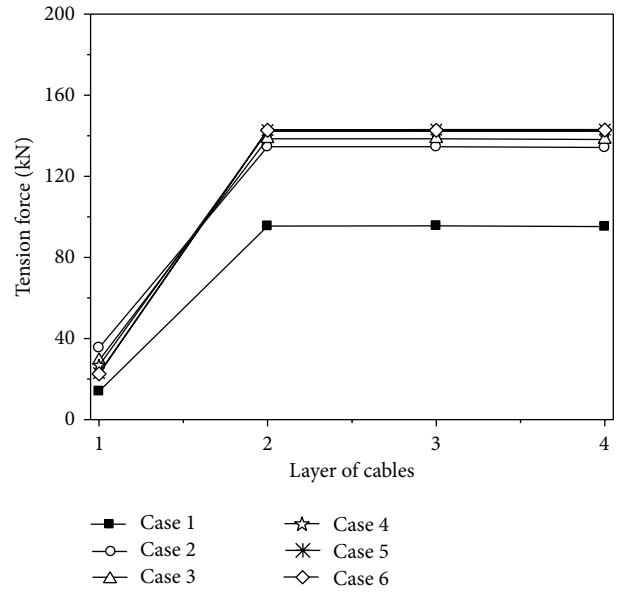


FIGURE 9: Tension forces of the cables under different degrees of coherency loss.

The maximum value curves of the vertical displacements of the cable under different site conditions are shown in Figure 10. It can be seen from Figure 10 that the vertical displacements of the cable have an increasing tendency with the site condition growing soft. The vertical displacements of the cable increase with the degree of the difference of site condition increasing.

The maximum value curves of tension forces of the cables under different site conditions are shown in Figure 11. It can be seen from Figure 11 that the tension forces of the cables have an increasing tendency with the site condition growing soft, and the maximum tension forces of the cables appear when the three transmission towers are located on soft sites. The tension forces of the cables change very little when the site is located in different types, and it could be ignored.

Based on the above analysis, the variations of the displacement and tension force responses of the cables considering different site conditions can be summarized. The vertical displacements and tension forces of the cable have an increasing tendency with the site condition growing soft. The responses of the cables change little with the degree of the difference of site condition changing, especially for the tension forces of the cables. Therefore, the local site effect should be considered for the seismic design of the transmission line structures.

5. Conclusion

The parametric studies of nonlinear dynamic responses of the transmission line structures subjected to earthquake loading are investigated in the paper. The effects of multicomponent ground motions, correlations among multicomponent ground motions, ground motion spatial variation, wave passage, coherency loss, and local site on the transmission

TABLE 4: Analysis cases considering the effect of local site.

Case	Apparent velocity	Coherency	Soil condition		
			1st tower	2nd tower	3rd tower
Case 1	Infinite	Perfectly	MF	MF	MF
Case 2	1000 m/s	Highly	F	F	F
Case 3	1000 m/s	Highly	MF	MF	MF
Case 4	1000 m/s	Highly	MS	MS	MS
Case 5	1000 m/s	Highly	S	S	S
Case 6	1000 m/s	Highly	F	MF	F
Case 7	1000 m/s	Highly	MS	MF	MS
Case 8	1000 m/s	Highly	S	MF	S

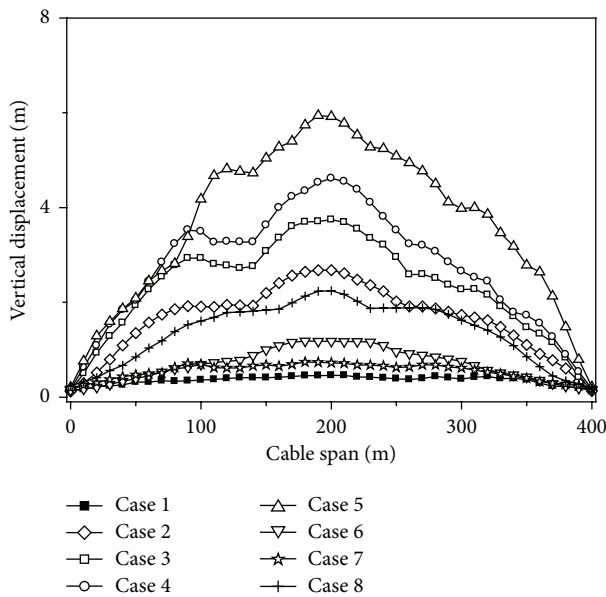


FIGURE 10: Vertical displacements of the cable under different site conditions.

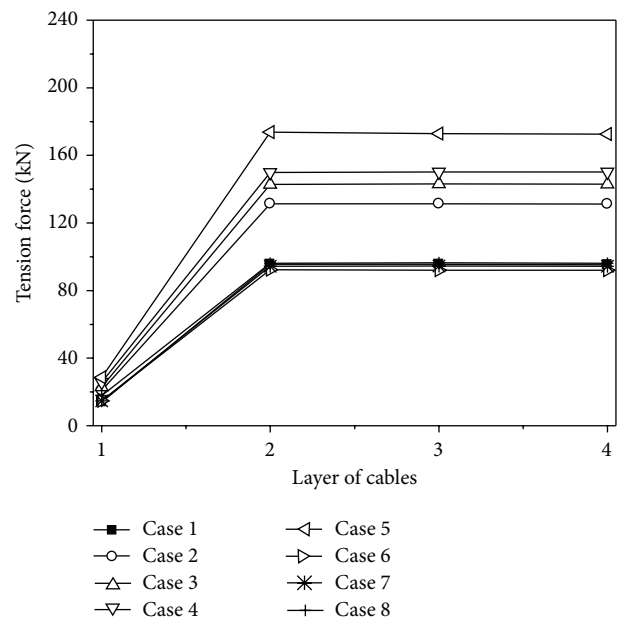


FIGURE 11: Tension forces of the cables under different site conditions.

line structures are considered, respectively. Based on the numerical results, the following conclusions are drawn.

- (1) The vertical displacements of the cable under multicomponent excitations are significantly larger than that of under vertical, longitudinal, or transverse excitation only. Multicomponent seismic excitations should be considered.
- (2) Ignoring the correlations among the multicomponent ground motions, the response of the cable may be small, but the changes are very little. The correlations among multicomponent ground motions can be neglected.
- (3) The responses of the cables considering the effect of ground motion spatial variations are larger than that of under uniform excitation. Wave travel effect of ground motion is more obvious to the influence of the structure than the other effect for the flexible structure of the transmission line structures.

- (4) The wave passage effect has a significant influence on the responses of the cables. Neglecting the wave passage effect in analysis, the cables responses would be underestimated. Because the tension forces of the cables are too large, the transmission lines would be pulled off. It is necessary to estimate the traveling wave velocity accurately.
- (5) The change of the degree of coherency loss has little influence on the response of the cables. The responses of the cables are affected significantly by the effect of coherency loss. It is very important to consider the coherency loss effect of ground motion for the seismic design of the transmission line structures.
- (6) The vertical displacements and tension forces of the cables have an increasing tendency with the site condition growing soft. The responses of the cables change little with the degree of the difference of site condition changing, especially for the tension forces.

Conflict of Interests

The authors declare that there is no conflict of interests regarding the publication of this paper.

Acknowledgment

This work is supported by the National Natural Science Foundation of China under Grant no. 51208285. The supports for this research are greatly appreciated.

References

- [1] J. F. Hall, W. T. Holmes, and P. Somers, *Northridge Earthquake of January 17, 1994*, Earthquake Engineering Research Institute, California, Calif, USA, 1994.
- [2] M. Shinozuka, "The Hanshin-Awaji earthquake of January 17, 1995, performance of lifelines," Report NCEER-95-0015, NCEER, 1995.
- [3] P. Zhang, G. Song, H. Li, and Y. Lin, "Seismic control of power transmission tower using pounding TMD," *Journal of Engineering Mechanics*, vol. 139, no. 10, pp. 1395–1406, 2013.
- [4] GB 50260-96, *Code for Seismic Design of Electrical Facilities*, National Standard of the People's Republic of China, China Plan Press, Beijing, China, 1996 (Chinese).
- [5] C. J. Wong and M. D. Miller, *Guidelines for Electrical Transmission Line Structural Loading*, American Society of Civil Engineers, New York, NY, USA, 2009.
- [6] H. Li, S. Xiao, and S. Wang, "Study on limits of height-to-width ratio for base isolated buildings under earthquake," *ASME PVP*, vol. 445, no. 2, pp. 143–147, 2002.
- [7] H. Li, W. Shi, G. Wang, and L. Jia, "Simplified models and experimental verification for coupled transmission tower-line system to seismic excitations," *Journal of Sound and Vibration*, vol. 286, no. 3, pp. 569–585, 2005.
- [8] A. Ghobarah, T. S. Aziz, and M. El-Attar, "Response of transmission lines to multiple support excitation," *Engineering Structures*, vol. 18, no. 12, pp. 936–946, 1996.
- [9] L. Tian, H. Li, and G. Liu, "Seismic response of power transmission tower-line system subjected to spatially varying ground motions," *Mathematical Problems in Engineering*, vol. 2010, Article ID 587317, 20 pages, 2010.
- [10] H. Li, F. Bai, L. Tian, and H. Hao, "Response of a transmission tower-line system at a canyon site to spatially varying ground motions," *Journal of Zhejiang University*, vol. 12, no. 2, pp. 103–120, 2011.
- [11] F. Bai, H. Hao, K. Bi, and H. Li, "Seismic response analysis of transmission tower-line system on a heterogeneous site to multi-component spatial ground motions," *Advances in Structural Engineering*, vol. 14, no. 3, pp. 457–474, 2011.
- [12] L. Tian, H. Li, and G. Liu, "Seismic response of power transmission tower-line system under multi-component multi-support excitations," *Journal of Earthquake and Tsunami*, vol. 6, no. 4, pp. 1–21, 2012.
- [13] W. M. Wang, H. N. Li, and L. Tian, "Progressive collapse analysis of transmission tower-line system under earthquake," *Advanced Steel Construction*, vol. 9, no. 2, pp. 161–174, 2013.
- [14] L. Tian, R. Ma, H. Li, and P. Zhang, "Seismic response of straight line type and broken line type transmission lines subjected to non-uniform seismic excitations," *Advanced Steel Construction*, vol. 10, no. 1, pp. 85–98, 2014.
- [15] S. Shen, C. Xu, and C. Zhao, *Design of Suspension Structure*, China Architecture and Building Press, Beijing, China, 1997, (Chinese).
- [16] H. Hao, C. S. Oliveira, and J. Penzien, "Multiple-station ground motion processing and simulation based on smart-1 array data," *Nuclear Engineering and Design*, vol. 111, no. 3, pp. 293–310, 1989.
- [17] K. Bi, H. Hao, and N. Chouw, "Required separation distance between decks and at abutments of a bridge crossing a canyon site to avoid seismic pounding," *Earthquake Engineering and Structural Dynamics*, vol. 39, no. 3, pp. 303–323, 2010.
- [18] L. Tian and H. Li, "Parameter study on seismic random model based on code for design of seismic electrical installations," *Journal of Disaster Prevention and Mitigation Engineering*, vol. 30, no. 1, pp. 17–22, 2010 (Chinese).
- [19] J. Penzien and M. Watabe, "Characteristics of 3-dimensional earthquake ground motions," *Earthquake Engineering and Structural Dynamics*, vol. 3, no. 4, pp. 365–373, 1975.
- [20] H. Hao, "Arch responses to correlated multiple excitations," *Earthquake Engineering and Structural Dynamics*, vol. 22, no. 5, pp. 389–404, 1993.

Research Article

The Effect Analysis of Strain Rate on Power Transmission Tower-Line System under Seismic Excitation

Li Tian,¹ Wenming Wang,² and Hui Qian³

¹ School of Civil and Hydraulic Engineering, Shandong University, Jinan 250061, China

² Shandong Electric Power Engineering Consulting Institute Co., Ltd., Jinan 250013, China

³ School of Civil Engineering, Zhengzhou University, Zhengzhou 450001, China

Correspondence should be addressed to Li Tian; tianli@sdu.edu.cn

Received 13 May 2014; Accepted 14 June 2014; Published 29 June 2014

Academic Editor: Fei Kang

Copyright © 2014 Li Tian et al. This is an open access article distributed under the Creative Commons Attribution License, which permits unrestricted use, distribution, and reproduction in any medium, provided the original work is properly cited.

The effect analysis of strain rate on power transmission tower-line system under seismic excitation is studied in this paper. A three-dimensional finite element model of a transmission tower-line system is created based on a real project. Using theoretical analysis and numerical simulation, incremental dynamic analysis of the power transmission tower-line system is conducted to investigate the effect of strain rate on the nonlinear responses of the transmission tower and line. The results show that the effect of strain rate on the transmission tower generally decreases the maximum top displacements, but it would increase the maximum base shear forces, and thus it is necessary to consider the effect of strain rate on the seismic analysis of the transmission tower. The effect of strain rate could be ignored for the seismic analysis of the conductors and ground lines, but the responses of the ground lines considering strain rate effect are larger than those of the conductors. The results could provide a reference for the seismic design of the transmission tower-line system.

1. Introduction

Power transmission tower-line system is an important component of a power system. Its reliable operation is of great significance in achieving the energy strategy of nationwide interconnection, power transmission from west to east, and mutual supply between north and south. So far, most of research attentions have been paid on the actions of static load, dynamic characteristic, and nonlinear time history analysis with only geometric nonlinear was taken into account [1–8]. However, several recent cases of damage to transmission towers during earthquakes have proved that the structure under strong earthquake excitation could enter nonlinear status. During the 1976 Tangshan earthquake, some transmission towers collapsed. In the 1999 CHI-CHI earthquake, a lot of transmission lines were broken and some towers collapsed [9]. In 2008, Sichuan electric network was damaged by the Wenchuan earthquake.

Therefore, studies about elastic-plastic analysis of transmission towers have been reported recently. Li et al. [10]

calculated the dynamic characters of two different kinds of towers, and the two transmission towers were calculated with two different pieces of seismic records based on the simplified method of seismic calculation, and the nonlinear behaviors and plastic limit of transmission towers in different vibration directions subjected to earthquake action were summarized. Xiong et al. [11] investigated the elastic-plastic analysis of a long-span concrete filled steel-tube transmission tower under earthquake actions by the static and the dynamic method. The results showed a lot of elements enter the plastic status soon after earthquake action and there were some steel-tube elements that failed but no concrete filled steel-tube element failed at last times. Albermani et al. [12] presented a nonlinear analysis technique for transmission tower structures, and the proposed technique could be used to accurately predict structural failure, with the predictions confirmed by the results of an expensive full-scale test. It is necessary to consider the effect of strain rate on transmission tower-line system using elastic-plastic analysis method. However, there

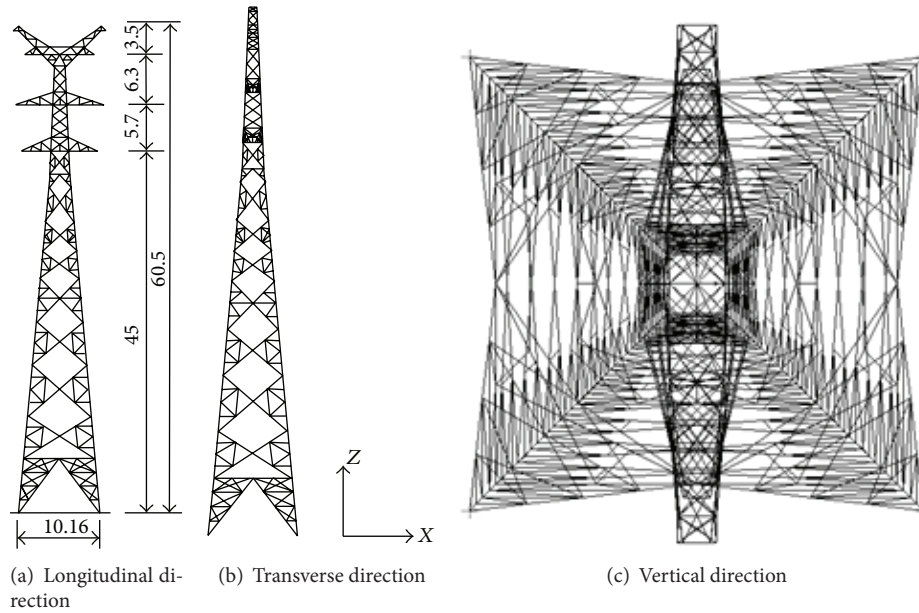


FIGURE 1: Longitudinal, transverse, and vertical views of a transmission tower (m).

TABLE 1: Mechanical properties of Q345 and Q235.

Material	Yield stress (Pa)	Young's modulus (Pa)	Poisson's ratio	Density (Kg/m ³)
Q345	$3.45E + 08$	$2.00E + 11$	0.3	7800
Q235	$2.35E + 08$	$2.00E + 11$	0.3	7800

is no research about the analysis of strain rate effect on transmission tower-line system at present.

The experimental results have showed that the steel is a rate sensitive material, which has different mechanical properties under different strain rates. A few experimental studies have been carried out in recent years. Chang and Lee [13] investigated the strain rate and strain rate history effects on the inelastic stress-strain behavior of annealed A-36 structural steel at room temperature under monotonic and cyclic loading conditions. Test results show relatively more significant strain rate sensitivity of the material for monotonic loading and less significant strain rate sensitivity for cyclic loading. Restrepo-Posada et al. [14] studied variables affecting cyclic behavior of reinforcing steel, and the effects of strain on the cyclic behavior of reinforcing steel can be very relevant when considering postearthquake retrofitting of reinforced concrete structures. Yang et al. [15] studied the dynamic tensile property of three steels, and the results showed that the yield strength and extension rate of the steel improved with strain rate increasing but the rate sensitivity was different. Song [16] carried out the dynamic cyclic loading test of steel, and the results showed that the yield strength of the steel improved with strain rate increasing, and the elastic modulus was not changed. At present general conclusion is that the yield strength and tensile strength of the steel have a certain improvement with strain rate increasing, and the increased range of yield strength is larger than the tensile strength, but

the elastic modulus is not changed. The lower the strength of the steel is, the more obvious the effect of strain rate is. Strain rate has an influence on the response of the structure under earthquake excitation. It is unreasonable to calculate the seismic response of the structure using static analysis, and the effect of strain rate should be considered. It is very important to study the influence of strain rate on the nonlinear seismic response of the structure.

This paper aims to investigate the influence of the strain rate effect on the power transmission tower-line system under different ground motion intensities. A subroutine is developed in ABAQUS. The progressive collapse simulation method is proposed. Incremental nonlinear time history analysis method is adapted to calculate the response with and without considering the strain rate effect. The results could provide a reference for the seismic design of the transmission tower-line system.

2. Structural Model

The selected tower for the analysis is illustrated in Figure 1, which has a height of 60.5 m and a square base area of 10.16 m × 10.16 m at ground level. The angle steel with equal section is used for all tower members. Main members of the tower are made of Q345, and secondary members are made of Q235. The mechanical properties of Q345 and Q235 are shown in Table 1.

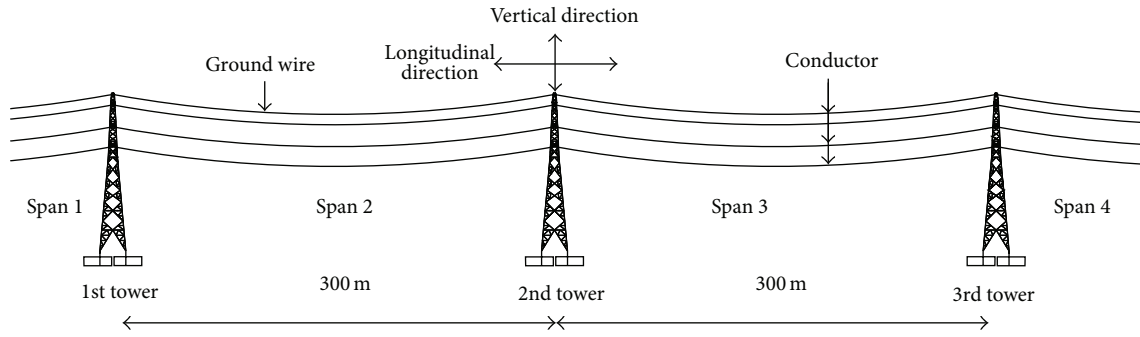


FIGURE 2: Three-dimensional finite element model of transmission tower-line system.

TABLE 2: Properties and performance indices of conductor, ground wire, and insulator.

Type	Area (m ²)	Young's modulus (Pa)	Poisson's ratio	Density (Kg/m ³)	Yield force (N)
Conductor	4.25E - 04	6.50E + 10	0.3	3172	98710
Ground wire	1.53E - 04	1.05E + 11	0.3	4631	74200
Insulator	0.02	7.65E + 10	0.2	7500	1000000

A transmission tower-line system consists of many towers and lines, and the coupling effects of tower and line are prominent. However, it is unrealistic to establish a model that includes all towers and lines. The numerical model contains three towers and four-span lines in the paper, which was verified to be reasonable [17, 18]. As shown in Figure 2, the transmission tower-line coupled system includes three towers (1st tower, 2nd tower, and 3rd tower) and four-span line (Span 1, Span 2, Span 3, and Span 4). The upper 8 cables are ground lines and the lower 24 cables are single bundled conductor. The spans of adjacent towers are all 300 m. The conductors and towers are connected with insulators and the materials for conductor and ground wire are steel-cored aluminum strand. The base points of the transmission tower are fixed on the ground, and the connections between transmission towers and lines are hinged. The side spans of the lines are hinged at the same height of the middle tower. The properties and performance indices of conductor, ground wire, and insulator are listed in Table 2.

The three-dimensional beam elements type, B31, with three translational and three rotational degrees of freedom per node, is employed to model the tower members, and the three-dimensional truss elements type, T3D2, with three translational degrees of freedom per node, is applied to model the lines and insulators in the ABAQUS software. Each tower contains 741 beam elements, each insulator contains one element, and the mesh selected for each conductor and ground wire consists of 100 truss elements.

3. Material Strain Rate and Analysis Method

3.1. Material Strain Rate. The strain rate of steel under seismic excitation is hard to exceed 1/s. The dynamic constitutive

relationship model incorporated in the finite element analysis is as follows [19]:

$$f_{yd} = \left(1 + c_f \lg \frac{\dot{\epsilon}}{\dot{\epsilon}_0} \right) f_{ys} \tag{1}$$

$$c_f = 0.1709 - 3.289 \times 10^{-4} f_{ys},$$

where $\dot{\epsilon}$ is the current strain rate; $\dot{\epsilon}_0$ is the quasistatic strain rate, $\dot{\epsilon}_0 = 2.5 \times 10^{-4}/s$; f_{ys} is the yield strength at quasistatic strain rate; f_{yd} is the dynamic yield strength at the current strain rate.

3.2. Theoretical Analysis. For the transmission tower-line system, the nonlinear dynamic analysis should be used because of its importance and complexity. The motion equation of structure under the seismic excitation is as follows:

$$M(t) \ddot{x}(t) + C(t) \dot{x}(t) + K(t) x(t) = -M(t) (\ddot{x}_u(t) + \ddot{x}_v(t) + \ddot{x}_w(t)), \tag{2}$$

where $\ddot{x}(t)$, $\dot{x}(t)$, and $x(t)$ are the relative acceleration, velocity, and displacement vectors; $\ddot{x}_u(t)$, $\ddot{x}_v(t)$, and $\ddot{x}_w(t)$ are the ground motion accelerations in two horizontal and one vertical directions, respectively; $M(t)$, $K(t)$, and $C(t)$ are the mass, stiffness, and damping matrices, respectively. Generally, $M(t)$ is an invariant, while $K(t)$ and $C(t)$ change during the earthquake.

If the ground motion intensity is weak, the material cannot enter nonlinear status. The mass, stiffness, and damping matrices are irrelevant to strain rate. The strain rate has no influence on the elastic response analysis of the structure. If the ground motion intensity is strong, the material can enter

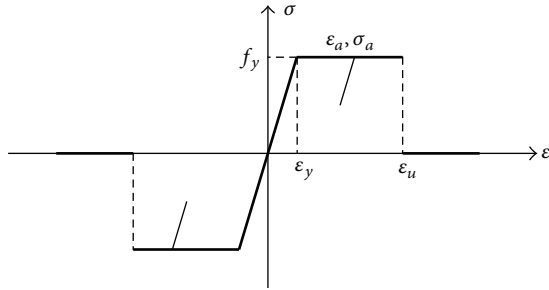


FIGURE 3: Stress-strain curve of steel.

nonlinear status. The stiffness matrix is relevant to strain rate, but the mass matrix is irrelevant to strain rate. The damping matrix is irrelevant to strain rate if the mass-damping is used. However, if stiffness-damping or Raleigh damping is chosen, the damping matrix is relevant to strain rate. Therefore, the strain rate has some influence on the plastic response analysis of the structure.

According to a series of ground motion intensity indices of monotone increasing of a specific seismic wave, the structure is analyzed using nonlinear time history analysis, and the nonlinear seismic response of the structure under different ground motion intensities can be obtained. The method is called incremental dynamic analysis (IDA) [20]. Multiple seismic waves are selected. The response of the structure is calculated by nonlinear time history analysis method with and without strain rate effect taken into account. The peak accelerations of the three-dimensional seismic waves are increased with equal proportions until progressive collapse of the structure occurs.

3.3. Progressive Collapse Simulation. Elastic-perfectly plastic material model is used, which is shown in Figure 3. The constitutive relationship is coded using the user subroutine VUMAT [21], which can be implemented in the advanced finite element program ABAQUS. According to the proposed method, once the strain exceeds ultimate strain, the stiffness of the element is zero while the mass remains the same.

For uniaxial loading, the stress-strain relationship of steel is as follows:

$$\sigma = \begin{cases} E_s \varepsilon & \varepsilon \leq \varepsilon_y, \\ f_y & \varepsilon_y \leq \varepsilon \leq \varepsilon_u, \\ 0 & \varepsilon > \varepsilon_u, \end{cases} \quad (3)$$

where ε and σ are the strain and stress, respectively; E_s is the elastic modulus; ε_y and f_y are the yield strain and yield stress, respectively; ε_u is the ultimate strain.

For cyclic loading, the stress-strain relationship is as follows:

$$\sigma = \sigma_a + E_s (\varepsilon - \varepsilon_a), \quad (4)$$

where σ_a and ε_a are the stress and strain of the starting point in the unloading curve, respectively.

4. The Selection of Seismic Waves

Three seismic waves are selected: (1) Kobe wave (1995); (2) Northbridge wave (1994); (3) El Centro wave (1940). And the seismic waves include two horizontal components and one vertical component. The NS, WE, and vertical components of seismic wave coincide with the Y, X, and Z directions of the transmission tower-line system shown in Figure 2, respectively. The material of transmission tower under seismic excitation is hard to enter plastic status and is very hard to collapse. When the plastic analysis is carried out, the ground motion intensity requires very strong amplitude. The structure under very strong earthquake action is analyzed using elastic-plastic analysis method. The increasing of ground motion intensity is fast at the beginning of the incremental dynamic analysis. When the structure is close to collapse, the increasing of seismic intensity is slow, and the minimum increment of ground motion intensity is 1 m/s^2 .

5. Numerical Simulation and Discussion

The responses of the strain rate effect on the power transmission tower line system shown in Figure 2 under different ground motion intensities are investigated. The nonlinear time history analysis method is used in the paper. The geometric nonlinearity is taken into account due to large deformation of the transmission lines and the material nonlinearity of the system is considered. The strain rate effect on the maximum top displacement and base shear force of the transmission tower are studied. The strain rate effect on the maximum tension force and vertical displacement of the conductor and ground line are also investigated.

5.1. The Effect of Strain Rate on the Transmission Tower.

The maximum top displacements of 2nd transmission tower under different seismic excitations are given in Table 3, and the table shows the responses of the transmission tower with and without considering the strain rate. It also can be seen from Table 3 that the transmission tower is easy to collapse under El Centro and Kobe earthquake actions, but it is hard to collapse under Northbridge earthquake action. The deformation capacity of the transmission tower under Kobe earthquake action is larger than those of the other two earthquake actions.

Figure 4 shows the relative changes of the maximum top displacements of 2nd transmission tower considering the effect of strain rate with the increasing ground motion intensity. It can be seen from Figure 4 that the effect of strain rate on the transmission tower may decrease or increase the maximum top displacements when the ground motion intensity is weak. When the transmission tower is close to collapse, the transmission tower considering the effect of strain rate significantly decreases the maximum top displacements. The effect of strain rate has little influence on the maximum top displacements of the transmission tower under Northbridge earthquake action. However, the effect of strain rate has a great influence on the maximum top displacements of the transmission tower under El Centro and

TABLE 3: Maximum top displacements of 2nd transmission tower.

Seismic wave	Peak acceleration (m/s ²)	Displacement (m)			
		X direction		Y direction	
		Without considering strain rate	Considering strain rate	Without considering strain rate	Considering strain rate
El Centro	6.0	0.243	0.243	0.330	0.329
	8.0	0.256	0.258	0.453	0.454
	10.0	0.339	0.318	0.514	0.513
	12.0	0.460	0.396	0.618	0.617
	14.0	0.841	0.757	0.691	0.687
	15.0	Collapse	1.124	Collapse	0.706
	16.0	Collapse	Collapse	Collapse	Collapse
Kobe	6.0	0.498	0.501	0.505	0.505
	8.0	0.685	0.682	0.701	0.694
	10.0	1.012	0.973	0.949	0.936
	12.0	1.085	1.020	1.121	1.084
	13.0	1.177	1.109	1.241	1.157
	14.0	Collapse	1.196	Collapse	1.268
	15.0	Collapse	Collapse	Collapse	Collapse
Northbridge	10.0	0.306	0.305	0.329	0.329
	15.0	0.518	0.516	0.453	0.455
	20.0	0.573	0.568	0.499	0.492
	23.0	0.681	0.674	0.644	0.640
	25.0	0.748	0.725	0.664	0.659
	27.0	0.828	0.813	0.743	0.740
	29.0	Collapse	0.880	Collapse	0.752
30.0	Collapse	Collapse	Collapse	Collapse	

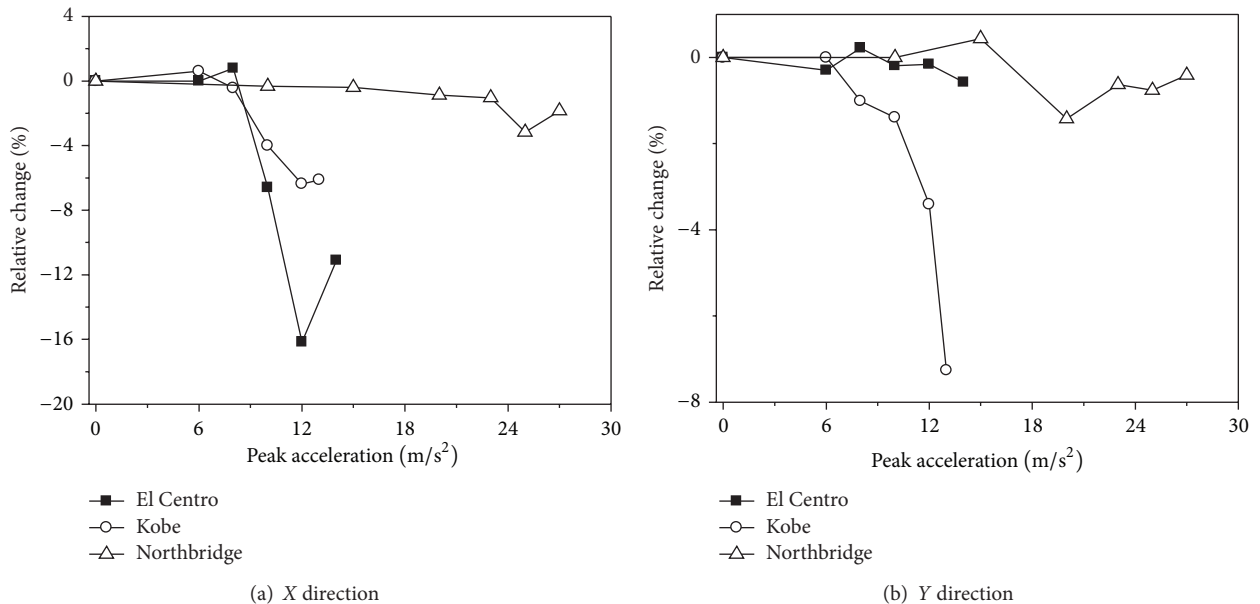


FIGURE 4: Relative changes of the maximum top displacements of 2nd transmission tower.

TABLE 4: Maximum base shear forces of 2nd transmission tower.

Seismic wave	Peak acceleration (m/s ²)	Shear force (kN)			
		X direction		Y direction	
		Without considering strain rate	Considering strain rate	Without considering strain rate	Considering strain rate
El Centro	6.0	138.465	136.894	163.459	157.404
	8.0	140.797	140.648	214.633	214.248
	10.0	151.760	154.172	262.068	268.623
	12.0	166.223	178.293	303.575	316.353
	14.0	203.141	212.887	319.025	323.093
	15.0	Collapse	222.141	Collapse	307.916
	16.0	Collapse	Collapse	Collapse	Collapse
Kobe	6.0	198.513	198.516	228.912	228.911
	8.0	228.882	228.878	260.429	260.427
	10.0	279.233	281.514	283.561	285.820
	12.0	248.166	252.340	263.036	267.653
	13.0	279.085	291.489	256.623	259.124
	14.0	Collapse	301.570	Collapse	267.427
	15.0	Collapse	Collapse	Collapse	Collapse
Northbridge	10.0	247.764	248.244	216.227	216.941
	15.0	289.418	289.030	309.638	309.181
	20.0	393.213	396.100	453.791	453.690
	23.0	456.353	458.828	469.431	474.372
	25.0	467.501	474.122	464.471	473.617
	27.0	465.700	481.191	500.019	520.178
	29.0	Collapse	485.623	Collapse	523.600
30.0	Collapse	Collapse	Collapse	Collapse	

Kobe earthquake actions, and the maximum reduction of the maximum top displacement is 16.2%. The effect of strain rate on the maximum top displacement of the transmission tower has an increasing tendency with the ground motion intensity increasing.

The maximum base shear forces of 2nd transmission tower under different seismic wave excitations are shown in Table 4. It can be seen from Table 4 that the base shear forces of the transmission tower under Northbridge earthquake action are very large. Figure 5 shows the relative changes of the maximum base shear forces of the transmission tower considering the effect of strain rate with the ground motion intensity increasing. The effect of strain rate on the transmission tower would decrease or increase the maximum base shear forces of the transmission tower. The nonlinear degree of the material is very low and the effect of strain rate is very small when the ground motion intensity is weak. The effect of strain rate would increase the maximum base shear forces of the transmission tower when the seismic ground motion is strong, and the maximum increase is 6.8%. The maximum base shear forces of the transmission tower considering strain rate effect are varied by less than 5%, but the effect of strain rate on the maximum base shear forces of the transmission tower is less than that of the maximum top displacements. The effect of strain rate on maximum

base shear forces of the transmission tower has an increasing tendency with the ground motion increasing.

5.2. The Effect of Strain Rate on the Conductor and Ground Line. The maximum tension forces and vertical displacements of the conductor of span 2 are given in Table 5. Relative changes to the conductor's maximum response considering the effect of strain rate with the ground motion increasing are shown in Figure 6. It can be seen from the analysis results that the effect of strain rate has little influence on the response of the conductor, and the maximum responses of the conductor considering the effect of strain rate are varied by less than 1%; so the effect of strain rate on the conductor can be ignored. The material of the conductor cannot enter plastic status, and the effect of strain rate has no direct influence on the response of the conductor, but it could have an indirect influence on the conductor through the transmission tower.

Table 6 shows the maximum tension forces and vertical displacements of the ground line of span 2. It can be seen from Table 6 that the change of the response of the ground line is very little with the ground motion increasing. Relative changes of the ground line's maximum responses considering the effect of strain rate with the ground motion increasing are shown in Figure 7. The effect of strain rate has little influence

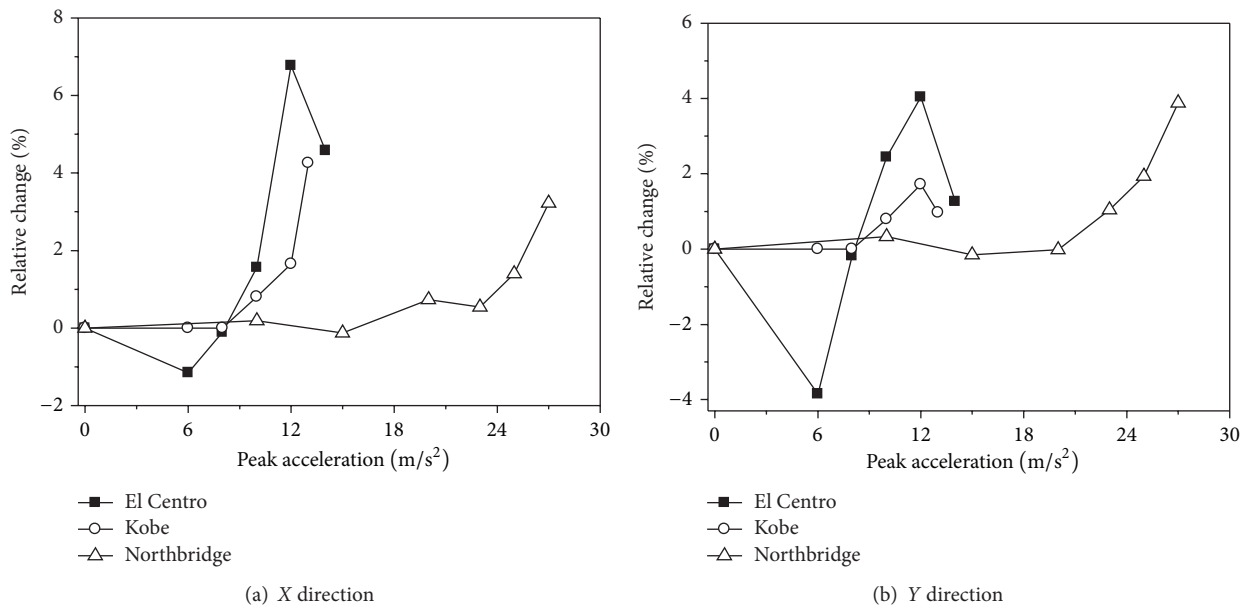


FIGURE 5: Relative changes of the maximum base shear forces of 2nd transmission tower.

TABLE 5: Maximum responses of the conductor.

Seismic wave	Peak acceleration (m/s ²)	Tension force (kN)		Vertical displacement (m)	
		Without considering strain rate	Considering strain rate	Without considering strain rate	Considering strain rate
El Centro	6.0	21.262	21.263	8.859	8.872
	8.0	21.244	21.245	8.625	8.635
	10.0	21.224	21.134	8.423	8.419
	12.0	22.089	22.205	8.420	8.408
	14.0	21.185	21.310	8.184	8.184
	15.0	Collapse	21.651	Collapse	8.197
	16.0	Collapse	Collapse	Collapse	Collapse
Kobe	6.0	21.321	21.321	8.629	8.629
	8.0	21.322	21.322	8.640	8.639
	10.0	21.322	21.323	8.674	8.674
	12.0	21.324	21.323	8.707	8.706
	13.0	21.361	21.359	8.756	8.758
	14.0	Collapse	21.366	Collapse	8.790
	15.0	Collapse	Collapse	Collapse	Collapse
Northbridge	10.0	21.323	21.323	8.377	8.377
	15.0	21.324	21.324	8.081	8.081
	20.0	22.239	22.219	7.386	7.389
	23.0	21.326	21.346	7.219	7.217
	25.0	21.545	21.517	7.220	7.220
	27.0	21.617	21.424	7.221	7.215
	29.0	Collapse	22.203	Collapse	7.223
30.0	Collapse	Collapse	Collapse	Collapse	

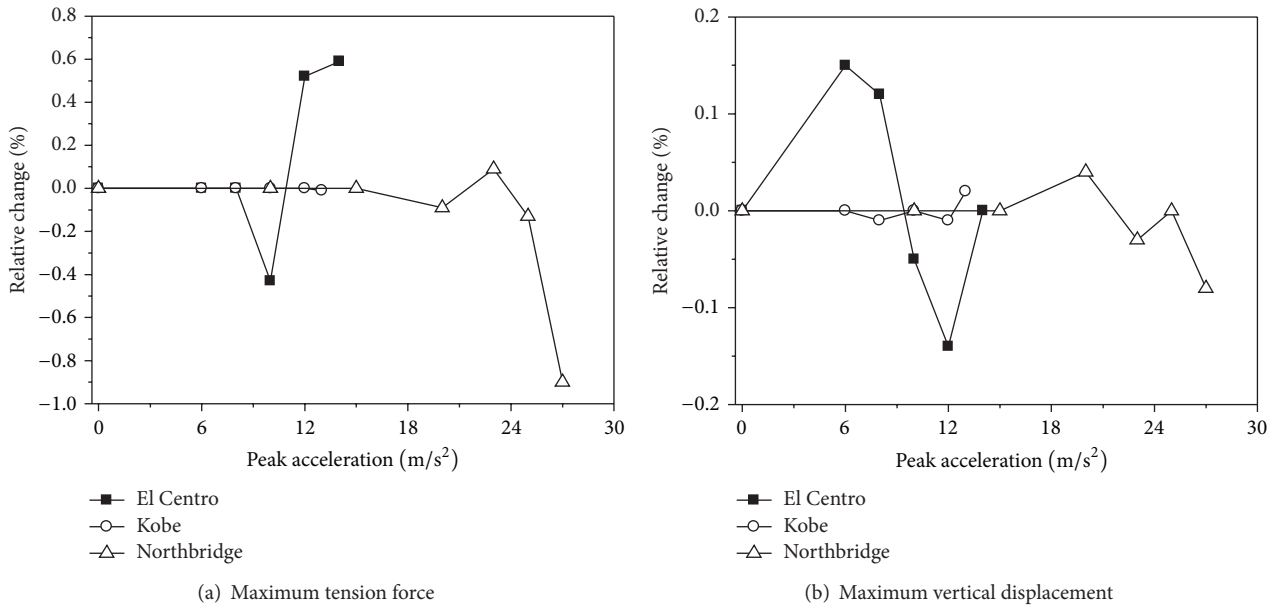


FIGURE 6: Relative changes of the conductor's maximum responses.

TABLE 6: Maximum responses of the ground line.

Seismic wave	Peak acceleration (m/s ²)	Tension force (kN)		Vertical displacement (m)	
		Without considering strain rate	Considering strain rate	Without considering strain rate	Considering strain rate
El Centro	6.0	17.239	17.292	3.509	3.513
	8.0	17.847	17.851	3.501	3.494
	10.0	18.651	18.589	4.428	4.377
	12.0	19.282	19.496	4.546	4.608
	14.0	19.183	19.512	4.276	4.315
	15.0	Collapse	19.965	Collapse	4.716
	16.0	Collapse	Collapse	Collapse	Collapse
Kobe	6.0	17.292	17.292	3.484	3.484
	8.0	17.292	17.291	3.485	3.484
	10.0	17.291	17.289	3.614	3.612
	12.0	17.292	17.290	3.586	3.579
	13.0	17.305	17.412	3.968	4.012
	14.0	Collapse	17.460	Collapse	4.163
	15.0	Collapse	Collapse	Collapse	Collapse
Northbridge	10.0	17.296	17.296	5.358	5.358
	15.0	22.424	22.423	5.487	5.487
	20.0	17.539	17.611	5.739	5.742
	23.0	20.882	20.870	5.253	5.258
	25.0	20.115	21.310	5.623	5.635
	27.0	20.790	20.053	5.152	5.161
	29.0	Collapse	21.136	Collapse	7.519
30.0	Collapse	Collapse	Collapse	Collapse	

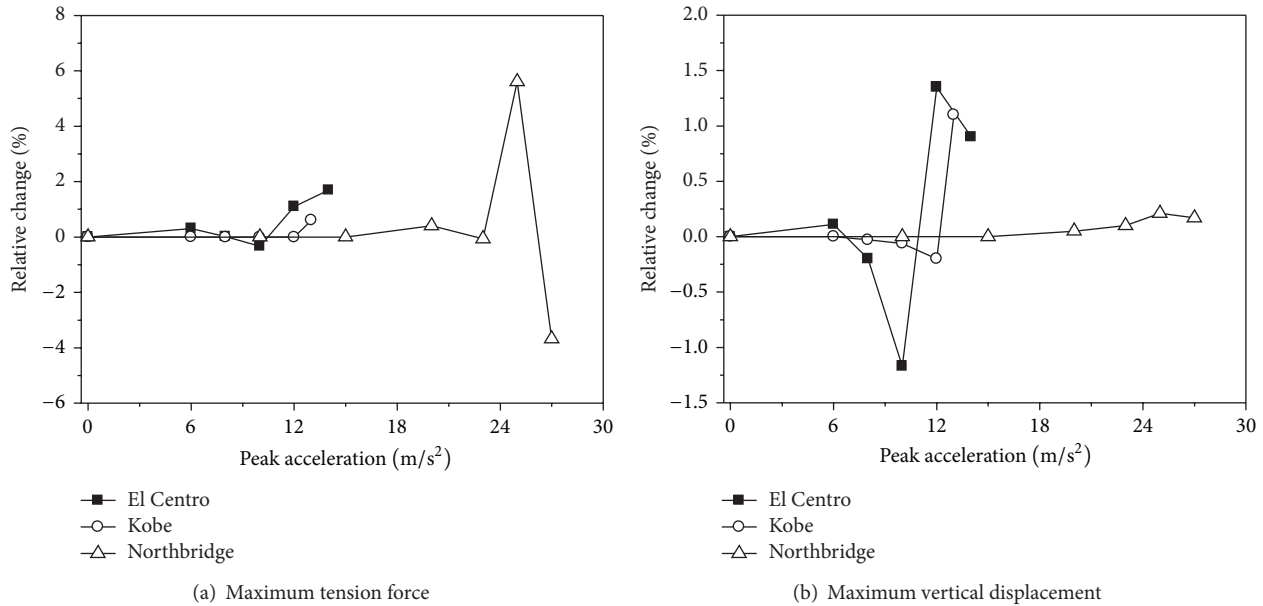


FIGURE 7: Relative changes of the ground wire's maximum responses.

on the ground line response, and the maximum responses of the ground line considering the effect of strain rate are varied by less than 6%. Comparing the response of the conductor and the ground line considering strain rate effect, the effect of strain rate on the ground line is more significant than that of the conductor. The reason is that the insulator length between the ground line and the transmission tower is shorter than that of between the conductor and the transmission tower.

6. Conclusion

The power transmission tower-line system is analyzed using incremental nonlinear time history analysis method, and the responses of strain rate on the transmission tower-line system are studied. Based on the numerical results, the following conclusions are drawn.

- (1) If the ground motion is weak, the effect of strain rate on the transmission tower would decrease the maximum top displacements in most of cases, but it would increase the maximum top displacements in few cases. The effect of strain rate on the transmission tower significantly decreases the maximum top displacements when the ground motion intensity of the transmission tower is close to collapse and the maximum reduction of the maximum top displacement is 16.2%.
- (2) If the ground motion is weak, the effect of strain rate on the transmission tower increases the maximum base shear forces in most of cases, but it would decrease the maximum base shear forces in few cases. The effect of strain rate on the transmission tower would increase the maximum base shear forces when the ground motion intensity of the transmission

tower is close to collapse, and the maximum increase of the maximum base shear force is 6.8%.

- (3) The effects of strain rate on the response of the transmission tower-line system have an increasing tendency with the ground motion intensity increasing.
- (4) The effect of strain rate has little influence on the response of the conductor, and the maximum responses of the conductor considering strain rate are varied by less than 1%; so the effect of strain rate on the conductor can be ignored. Comparing the responses of the conductor and ground line considering the effect of strain rate, the effect of strain rate on the ground line is more significant than that of the conductor, but the maximum responses of the ground line considering strain rate effect are less than 6%.

This study demonstrates that the strain rate effect is very important to transmission tower-line system, especially for transmission tower. As many other type towers such as cat head type towers, cup towers, and guyed towers are also widely used in the powers transmission systems, more studies are deemed necessary to further investigate the strain rate effect on responses of these systems.

Conflict of Interests

The authors declare that there is no conflict of interests regarding the publication of this paper.

Acknowledgments

This work is supported by the National Natural Science Foundation of China under Grant no. 51208285 and China Postdoctoral Science Foundation Funded Project under Grant no. 2012M521338. The support for this research is greatly appreciated.

References

- [1] H. Li, W. Shi, G. Wang, and L. Jia, "Simplified models and experimental verification for coupled transmission tower-line system to seismic excitations," *Journal of Sound and Vibration*, vol. 286, no. 3, pp. 569–585, 2005.
- [2] A. Ghobarah, T. S. Aziz, and M. El-Attar, "Response of transmission lines to multiple support excitation," *Engineering Structures*, vol. 18, no. 12, pp. 936–946, 1996.
- [3] H. Li and H. Bai, "High-voltage transmission tower-line system subjected to disaster loads," *Progress in Natural Science*, vol. 16, no. 9, pp. 899–911, 2006.
- [4] F. G. A. Albermani and S. Kitipornchai, "Numerical simulation of structural behaviour of transmission towers," *Thin-Walled Structures*, vol. 41, no. 2-3, pp. 167–177, 2003.
- [5] S. Ozono and J. Maeda, "In-plane dynamic interaction between a tower and conductors at lower frequencies," *Engineering Structures*, vol. 14, no. 4, pp. 210–216, 1992.
- [6] L. Tian, R. Ma, H. Li, and P. Zhang, "Seismic response of straight line type and broken line type transmission lines subjected to non-uniform seismic excitations," *Advanced Steel Construction*, vol. 10, no. 1, pp. 85–98, 2014.
- [7] H. Li, F. Bai, L. Tian, and H. Hao, "Response of a transmission tower-line system at a canyon site to spatially varying ground motions," *Journal of Zhejiang University*, vol. 12, no. 2, pp. 103–120, 2011.
- [8] F. Bai, H. Hao, K. Bi, and H. Li, "Seismic response analysis of transmission tower-line system on a heterogeneous site to multi-component spatial ground motions," *Advances in Structural Engineering*, vol. 14, no. 3, pp. 457–474, 2011.
- [9] P. Zhang, G. Song, H. Li, and Y. Lin, "Seismic control of power transmission tower using pounding TMD," *Journal of Engineering Mechanics*, vol. 139, no. 10, pp. 1395–1406, 2013.
- [10] H. Li, D. Hu, and L. Huang, "Plastic limit analysis of the transmission tower system subjected to earthquake action," *Proceedings of the Chinese Society of Electrical Engineering*, vol. 26, no. 24, pp. 192–199, 2006 (Chinese).
- [11] T. Xiong, S. Liang, L. Zou, and H. Wu, "Elastic-plastic analysis of a long-span concrete filled steel-tube transmission tower under earthquake action," *Engineering Mechanics*, vol. 29, no. 11, pp. 158–164, 2012 (Chinese).
- [12] F. Albermani, S. Kitipornchai, and R. W. K. Chan, "Failure analysis of transmission towers," *Engineering Failure Analysis*, vol. 16, no. 6, pp. 1922–1928, 2009.
- [13] K. C. Chang and G. C. Lee, "Strain rate effect on structural steel under cyclic loading," *Journal of Engineering Mechanics*, vol. 113, no. 9, pp. 1292–1301, 1987.
- [14] J. I. Restrepo-Posada, L. L. Dodd, R. Park, and N. Cooke, "Variables affecting cyclic behavior of reinforcing steel," *Journal of Structural Engineering*, vol. 120, no. 11, pp. 3178–3196, 1994.
- [15] D. Yang, J. Yu, Z. Li, and Z. Duan, "An experimental study on the tensile properties and damage mechanism of three alloy steel at high strain rate," *ACTA Armamentarii*, vol. 3, pp. 65–73, 1992 (Chinese).
- [16] J. Song, *Investigation of mechanical parameters for rate-sensitive material and its applications [Ph.D. thesis]*, Tsinghua University, Beijing, China, 1990, (Chinese).
- [17] L. Tian, H. Li, and G. Liu, "Seismic response of power transmission tower-line system subjected to spatially varying ground motions," *Mathematical Problems in Engineering*, vol. 2010, Article ID 587317, 20 pages, 2010.
- [18] L. Tian, H. Li, and G. Liu, "Seismic response of power transmission tower-line system under multi-component multi-support excitations," *Journal of Earthquake and Tsunami*, vol. 6, no. 4, Article ID 1250025, 21 pages, 2012.
- [19] M. Li and H. Li, "Effects of strain rate on reinforced concrete structure under seismic loading," *Advances in Structural Engineering*, vol. 15, no. 3, pp. 461–475, 2012.
- [20] ABAQUS, *ABAQUS Analysis User's Manual*, ABAQUS, 2010.
- [21] D. Vamvatsikos and C. Allin Cornell, "Incremental dynamic analysis," *Earthquake Engineering and Structural Dynamics*, vol. 31, no. 3, pp. 491–514, 2002.